AN AXIAL-FLUX SWITCHED RELUCTANCE MOTOR FOR LIGHT ELECTRIC VEHICLES

McMASTER UNIVERSITY

An Axial-Flux Switched Reluctance Motor for Light Electric Vehicles

by

JACK GILLIES, B.Tech

A thesis submitted in partial fulfillment for the
degree of Master of Applied Science

in the
Faculty of Engineering
Department of Mechanical Engineering

September 2020

McMaster University MASTER OF APPLIED SCIENCE (2020) Hamilton, Ontario (Mechanical Engineering)

TITLE: An Axial-Flux Switched Reluctance Motor for Light Electric Vehicles

AUTHOR: John (Jack) Gillies, B.Tech (McMaster University)

CO-SUPERVISORS: Dr. Ali Emadi and Dr. Berker Bilgin

PAGES: xxii, 135

Lay Abstract

This thesis documents the design of a new type of electric motor that is intended to be used in a small electric vehicle. The electric motor is different from the majority of motors used in this application for two reasons: firstly, the motor is a switched reluctance motor, which means that it does not contain any permanent magnets, offering cost savings and additional robustness. Secondly, the machine takes the form of a disk, where the magnetic interface between rotating and stationary components is on the face perpendicular to the axis of rotation. Normally, electric motors have the magnetic interface on the cylindrical surface which is parallel to the axis of rotation. The disk form factor presents multiple design challenges, which when coupled with the switched reluctance motor type, are addressed. A series of mathematical models are built to predict the performance of the motor in the vehicular application. Finally, a prototype of the motor is constructed.

Abstract

In an increasingly urgent climate crisis, the use of electric powertrains in smaller, purpose-built vehicles can expedite the global adoption of electrification. This thesis discusses the detailed design of an axial-flux switched reluctance motor for application in a light electric vehicle, such as an E-motorcycle. A vehicle application is studied based on typical driving conditions in an urban environment. The requirements of the propulsion motor are extracted, and a baseline machine topology is analyzed for its performance and manufacturability, towards the goal of a functional prototype. The prototype design includes a self-supporting foil winding, designed to maximize the use of axial space and allow for good conductive heat transfer to the machine casing. The rotor structure is found to be a limiting factor, where maximum speed is limited by the mechanical stresses.

The performance of the motor is analyzed in detail, beginning with a numerical iron loss model that is implemented to provide faster simulation time of the machine efficiency than FEA. The efficiency is found to peak at 90%, comparable with other traction motors of similar size on the market. The switching angles are studied, and the trade-offs between torque quality and efficiency are quantified over the drive cycle. It was determined that the vehicle could save 19.6 Wh/km by accepting poor torque quality and operating with the most efficient control parameters. Thermal analysis is performed to determine the realistic performance limitations. The machine was found to have power ratings of 7.12 kW instantaneous and 4.76 kW continuous. The final temperature of the winding during the drive cycle was predicted not to exceed the temperature ratings of the insulation system. Finally, the prototype is assembled, and a test plan is outlined for qualification of the motor.

Acknowledgements

I would like to first and foremost extend my utmost gratitude towards Dr. Ali Emadi and Dr. Berker Bilgin. I thank you for your thoughtfulness and expertise, and for always making sure I walked out of your offices with calmed nerves and a compelling direction for next steps in this project.

Secondly, thank you to Tim Lambert, who provided valuable technical guidance throughout the course of this project. I consider myself lucky to have been taken in by a mentor of such astoundingly diverse technical know-how and relentless drive for innovation.

The groundwork for this research was laid by Jianing Lin, who I was fortunate enough to work alongside through the remainder of her Ph.D studies. Her research in the pole configuration and rotor pole shaping provided a solid foundation for this project, and made the case for the continued product development effort.

Many of my colleagues took on various supportive roles throughout my graduate studies. I offer special thanks to Elizabeth Trickett, who took me under her wing and showed me what it means to be both a question-asker and a question-answerer. Thank you to those who rolled up their sleeves to lend a hand with the coil winding, including Elizabeth Trickett, John Reimers, Jianing Lin and Silvio Rotili Filho. To countless others who took interest in my rants about airgaps, or were otherwise there to share a laugh, I thank you for your camaraderie and wish you the best.

Several others were instrumental in getting the motor prototype built. Thank you to Chris Mak and Rob Lau for our valuable discussions on the motor fabrication. To Megan Wood and Andrew George of the EcoCar team, thank you for letting me steal your tools and occupy your workspace. Thanks to Dr. Beth McNally for your help with the sample preparation for the encapsulation material.

Thank you to Stanley Baer and Bill Jager from Accelerated Systems Inc for having me at the shop to machine the stator poles. It was admittedly challenging to stay focused on the task at hand when there was such a frenzy of fascinating products being developed and tested at ASI.

Also integral to the construction of the motor was Kyle Threndyle from Merq Inc, who went out on a limb to take on the carbon fiber machining. The rotor yoke and retaining ring turned many heads in the lab, and the quality was critical to the success of the prototype.

Needless to say, I must extend thanks to my family and friends for their continued support and taking an active interest in the challenges that I faced. Finally, to Delphine, to whom I owe my sanity and perseverance as we navigated an uncertain world together, I am grateful for your companionship.

Contents

List of Figures

List of Tables

Abbreviations

AC	Alternating Current
AFBDC	Axial Flux Brushed Direct Current
AFIM	Axial Flux Induction Motor
AFM	Axial Flux Motor
AFPMSM	Axial Flux Permanent Magnet Synchronous Motor
AFSRM	Axial Flux Switched Reluctance Motor
AG	Airgap
AWG	American Wire Gauge
BDC	Brushed Direct Current
BEMF	Back Electromotive Force
BMS	Battery Management System
CFRP	Carbon Fiber Reinforced Polymer
CSRM	C-core Switched Reluctance Motor
DC	Direct Current
EV	Electric Vehicle
FEA	Finite Element Analysis
FFT	Fast Fourier Transform
FSAFM	Flux Switching Axial Flux Motor
GOES	Grain Oriented Electrical Steel
ICE	Internal Combustion Engine
IM	Induction Motor
IPM	Interior Permanent Magnet

LEV	Light Electric Vehicle
LPTM	Lumped Parameter Thermal Model
MMF	Magnetomotive Force
MRMS	Multi-Rotor Multi-Stator
ORIS	Outer Rotor Inner Stator
OSIR	Outer Rotor Inner Stator
PEC	Power Electronic Converter
PMSM	Permanent Magnet Synchronous Motor
RFM	Radial Flux Motor
RMF	Rotating Magnetic Field
RMSE	Root Mean Square Error
RPM	Rotations Per Minute
SMC	Soft Magnetic Composite
SPM	Surface Permanent Magnet
SRM	Switched Reluctance Motor
SS	Single-Sided
TRS	Transverse Rupture Strength
VSI	Voltage Source Inverter
YASA	Yokeless and Segmented Armature

Symbols

$\mathbf{A_{w}}$	Winding area
$\mathbf{A_{f}}$	Vehicle frontal area
$\mathbf{A}$	Dowell equation argument
$\mathbf{A_{impact}}$	Area of impact zone
$\mathbf{A_{pole}}$	Pole face area
$\vec{\boldsymbol{B}}$, $\boldsymbol{B}$	Magnetic Flux Density
$\mathbf{C_{torqueError}}$	Cost assigned to deviation from torque setpoint
$\mathbf{C_{1}}$, $\mathbf{C_{2}}$	Coefficients for Nusslet number
$\mathbf{C_{D}}$	Coefficient of drag
$\mathbf{C_{R0}}$, $\mathbf{C_{R1}}$	Static, dynamic coefficient of rolling resistance
$\mathbf{d}$	conductor diameter
$\mathbf{D}$	Diameter
$\mathbf{D_{o}}$, $\mathbf{D_{i}}$	Inner and outer rotor diameters
$\mathbf{E_{wall}}$	Energy to rupture containment wall
$\mathbf{f}$	Frequency
$\mathbf{F_{A}}$	Acceleration force
$\mathbf{F_{C}}$	Climbing force
$\mathbf{F_{D}}$	Drag force
$\mathbf{F_{R}}$	Rolling resistance force
$\vec{\boldsymbol{F}}$, $\mathbf{F}$	Force
$\mathbf{g}$	Gravitational constant
$\mathbf{G}$	Vibration transmissibility

$\mathbf{h}$	Conductor height
$\mathbf{H}$	Magnetic field strength
$\vec{\boldsymbol{I}}$, $\mathbf{I}$	Current
$\mathbf{I_{RMS}}$	RMS current
$\mathbf{I_{targ}}$	Target SRM phase current
$\mathbf{J}$	Inertia
$\mathbf{K_{ec}}$	Eddy current coefficient
$\mathbf{K_{excess}}$	Excess loss coefficient
$\mathbf{K_{hyst}}$	Hysteresis loss coefficient
$\mathbf{K_{Z}}$	Axial stiffness
$\mathbf{l_{g}}$	Airgap length
$\mathbf{L}$	Inductance
$\mathbf{L_{A}}$	Armature length
$\mathbf{M}$	Mass
$\mathbf{N}$	Number of Turns
$\mathbf{N_{Gear}}$	Gear ratio
$\mathbf{N_{l}}$	Number of winding layers
$\mathbf{N_{Phase}}$	Number of phases
$\mathbf{N_{R}}$	Number of rotor poles
$\mathbf{N_{RPM}}$	Rotational speed in RPM
$\mathbf{N_{T}}$	Number of torque setpoints
$\mathbf{N_{\omega}}$	Number of speed setpoints
$\mathbf{Nu}$	Nusslet number
$\mathbf{p}$	Conductor pitch
$\mathbf{P_{copper}}$	Copper loss
$\mathbf{P_{ec}}$	Eddy current loss
$\mathbf{P_{excess}}$	Excess loss
$\mathbf{P_{hyst}}$	Hysteresis loss
$\mathbf{P_{iron}}$	Iron loss
$\mathbf{P_{impact}}$	Perimeter of impact zone

$\mathbf{P_{loss}}$	Power loss
$\mathbf{P_{mech}}$	Mechanical loss
$\mathbf{P_{out}}$, $\mathbf{P_{in}}$	Output, input power
$\mathbf{R_{Phase}}$	Phase resistance
$\mathbf{Re}$	Reynolds Number
$\mathbf{R_A}$	Armature resistance
$\mathbf{r_{wheel}}$	Wheel radius
$\mathbf{r_f}$	Frequency ratio
$\mathbf{r_o}$, $\mathbf{r_i}$	Inner and outer rotor radii
$\mathbf{T}$, $\boldsymbol{\tau}$	Torque
$\mathbf{T_r}$	Torque ripple
$\mathbf{t_{wall}}$	Containment wall thickness
$\mathbf{v}$	Velocity
$\mathbf{V}$	Voltage
$\mathbf{V_{DC}}$	DC link voltage
$\mathbf{W_C}$	Coenergy
$\mathbf{W_{Elec}}$	Electrical Energy
$\mathbf{W_{Field}}$	Field Energy
$\mathbf{W_{Mech}}$	Mechanical Energy
$\boldsymbol{\alpha}$	Rotor angle to stator field
$\boldsymbol{\alpha}_{\mathrm{c}}$	Vehicle climb angle
$\boldsymbol{\delta}_{\mathrm{R}}$	Rotating mass factor
$\boldsymbol{\delta}_{\mathrm{g}}$	Airgap deflection
$\boldsymbol{\delta}$	Skin depth
$\boldsymbol{\epsilon}$	Strain
$\boldsymbol{\eta}$	Efficiency
$\boldsymbol{\eta}_{\mathrm{gear}}$	Gearbox efficiency
$\boldsymbol{\eta}_{\mathrm{w}}$	Conductor geometry factor
$\boldsymbol{\mu}$	Magnetic permeability
$\boldsymbol{\mu}_0$	Permeability of free space

$\boldsymbol{\mu}_{\mathrm{f}}$	Friction coefficient
$\boldsymbol{\mu}_{\mathrm{air}}$	Dynamic viscosity of air
$\boldsymbol{\lambda}$	Flux linkage
$\boldsymbol{\theta}$	Electrical angle
$\boldsymbol{\theta}_{\mathrm{on}}$, $\boldsymbol{\theta}_{\mathrm{off}}$	Turn on, turn off angles
$\boldsymbol{\omega}$	Angular velocity
$\boldsymbol{\rho}_{\mathrm{air}}$	Air density
$\boldsymbol{\rho}$	Electrical resistivity
$\boldsymbol{\phi}$	Magnetic flux
$\mathscr{R}$	Magnetic reluctance
$\boldsymbol{\sigma}_{\mathrm{t}}$	Electromagnetic stress
$\boldsymbol{\sigma}_{\mathrm{max}}$	Maximum stress
$\boldsymbol{\zeta}$	Damping factor

Declaration of Academic Achievement

The text and figures contained in this thesis were created by Jack Gillies, except where referenced otherwise. The fabrication of components was an effort led by Jack Gillies, however outsourced machining was used where noted. Consultation was gathered from various engineers and technicians, but ultimately all design decisions were made by Jack Gillies

The prior work on this motor topology was carried out by Jianing Lin and Tim Lambert, as documented in [1].

The ideas that steered the direction of this work were a collaborative effort between author Jack Gillies, supervisors Dr. Berker Bilgin and Dr. Ali Emadi, and project sponsor Tim Lambert. All analysis and development was carried out by Jack Gillies.

Attempts are made to cite information that is not considered original, or common knowledge in the field. Ideas presented that are interpreted as similar to uncited works are not intended to be claimed as the author's own.

Dedicated to the memory of Iman Aghabali and Mehdi Eshagian

Chapter 1

Introduction

1.1 Background and Motivation

The elimination of carbon emissions for transportation is a partial but necessary component of the effort to ensure the sustainability of the human civilization. Electrification of passenger vehicles is a significant technological hurdle which can be easily preceded by electrification of smaller vehicles. Light Electric Vehicles (LEVs) such as E-scooters, E-motorcycles and E-rickshaws have the opportunity to gain significant popularity before electric vehicles due to the low cost. The small size and bounded use cases allow the production of an affordable vehicle, whereas passenger EVs must be designed to suit the edge cases of consumer use, such as inter-city road trips in winter conditions. LEVs may be sized for more specific conditions, such as delivery of goods within city limits. Therefore, while EV technology is still becoming mainstream, a large market exists for LEVs to reduce the number of fossil-fuel powered trips [2]. Nowadays, the majority of traction machines used in EVs use permanent magnets, which rely on materials such as Neodymium, of which the price is subject to a high volatility [3]. The Switched Reluctance Motor (SRM) is a type of electrical machine that does not use any permanent magnets, and is suited to traction applications due to the robust construction and large constant power range [4]. Traditionally, traction machines for EVs have a concentric rotor and stator, where the magnetic flux acts perpendicular to the axis of rotation, known as Radial-Flux Machines (RFMs). Alternatively, Axial Flux Machines (AFMs) have disk-shaped rotor and stator and are arranged in coplanar fashion, where the magnetic flux acts in the direction of the rotational axis. AFMs have gained popularity in recent years in motorsport applications, where short axial length allows for more compact design in a vehicle powertrain. Axial Flux Switched Reluctance Motors (AFSRMs) can have the benefits of short axial length and high torque density typical of AFMs, without the use of permanent magnet materials. This research project will investigate a topology of AFSRM that has not previously been prototyped and attempt to tackle some of the challenges involved at the intersection between axial-flux and switched reluctance motor types.

1.2 Contributions

This thesis discusses the realization of a novel AFSRM design. A self-supporting foil winding is implemented to achieve high fill factor even with hand-wound coils. The foil winding achieves superior heat removal due to the high contact area between turns and to the machine casing. To date, there is limited research into foil windings in electric motors, with the exception of work by Rios [5] [6] who prototyped a radial-flux machine. This thesis proposes the self-supporting foil windings as beneficial features for axial flux motors due to the improved utilization of the machine axial length. Additionally, a novel rotor structure is prototyped, which uses a carbon-fiber based composite to provide both axial retention and assist with the radial retention of rotor poles.

1.3 Thesis Outline

- **Chapter 2** introduces the LEV powertrain and discusses the challenges associated with the design of the electric machine. A vehicle model is introduced which calculates road loads under typical LEV driving conditions in order to determine motor design targets.

- **Chapter 3** introduces the switched reluctance motor and its phenomenological modeling. The key differences between radial flux motors (RFMs) and axial flux motors (AFM) are introduced, and a review of axial flux SRMs is presented.
- **Chapter 4** discusses the design of an AFSRM that fits the requirements for the LEV powertrain in Chapter 2. The mechanical, electromagnetic and manufacturing challenges of the AFSRM are investigated.
- **Chapter 5** uses the static characteristics of the AFSRM design for more detailed performance analysis including efficiency, torque quality and duty cycle.
- **Chapter 6** documents the prototyping of the AFSRM and discusses the manufacturing challenges encountered
- **Chapter 7** discusses future work necessary for further product development of the AFSRM.

Chapter 2

Electric Powertrains for Light Electric Vehicles

While the shift to electrified powertrains for on-road passenger vehicles has been slow, LEVs are good candidates for electrification due to the small size, predictable driving conditions and low cost. The electrification of passenger vehicle presents many product design challenges, namely battery cost and mass. A major barrier for adoption of passenger EVs is the battery cost, which must meet the top percentile of trips, even if long range driving is infrequently required. This results in unused vehicle mass for many use cases, for instance delivery of small quantities of goods, or carrying few passengers. Therefore, a LEV could be cost effective when the use is targeted towards short-range, low mass transportation of goods or personnel. Examples of light electric vehicles are E-mopeds, E-motorcycles, heavy quadricycles and golf cars. Although definitions of LEV have not been standardized across the industry, the following key differences to EVs can be highlighted:

Parameter	LEV	EV
DC bus voltage	24-96V	>300V
Nominal Output Power	1-10 kW	>80 kW
Mass	<400 kg	>1000 kg
Typical speeds	0-60 km/h	0-120 km/h

TABLE 2.1: Comparison of LEV and EV specifications

2.1 Components of LEV Powertrains

A typical LEV powertrain consists of the battery, the power electronic converter (PEC), the traction motor and the gear reduction. The battery stores electrical energy using multiple electrochemical cells in series and parallel, and is typically controlled with a battery management system (BMS). The power electronic converter is a device that regulates the exchange of current between the battery and the traction motor. AC machines are driven by voltage source inverter (VSI) with integrated DC-link capacitor. For DC machines, a single-switch PEC can be used for single-quadrant operation or full H-bridge for four quadrant. The traction motor acts as the conversion plant between electrical and mechanical power. The motor acts as a generator during braking and converts the mechanical power back to electrical, thus the term "electrical machine" instead of "motor" is often used. Due to the high-speed nature of the typical compact electrical machine, a gear reduction is necessary to reduce the speed and increase the torque from the shaft to the wheels, however in-wheel motor are becoming increasingly common for two-wheel vehicles. Otherwise, chain or belt drives are typical for two or three wheeled vehicles. For four wheel vehicles, a differential may act as both the reduction gear and the power split device between the two drive wheels.

2.2 Review of Light Electric Vehicle Propulsion Technologies

The most basic form of electric machine is the Brushed DC (BDC) motor, which uses rotor-mounted windings and commutator rings to produce torque. Although widely popular due the simplicity of the construction and control, the DC machine does not make effective use of every armature winding for the entire mechanical period, leading to low power density. Additionally, the DC machine suffers from high maintenance due to the presence of brushes, and poor overloading performance due to the isolated heat on the rotor. Despite this, BDC machines can often be found in early golf-carts. Brushless DC motors, which are a type of permanent magnet synchronous motors (PMSM), are the de-facto standard for all light duty traction applications. The high power density and high efficiency make the PMSM a good candidate for mobile applications. The PMSM may be configured as an external rotor machine, allowing for in-wheel drive for eBikes and eScooters, offering space for the battery elsewhere onboard. The longstanding alternative to PMSM, the induction motor (IM), has demonstrated potential as a traction motor in the Tesla Model S/X and the early Ford Ranger EV, however has not commonly appeared in the lower-power traction applications.

2.2.1 Brushed DC Motors

A brushed machine is named for the sliding interface that is necessary to conduct current onto the rotor. Coils of conductor are wound around the rotor lamination stack, and are provided current in sequence, such that a coil is excited when its axis is perpendicular to the direction of the stator field B, as seen in Figure 2.1a.

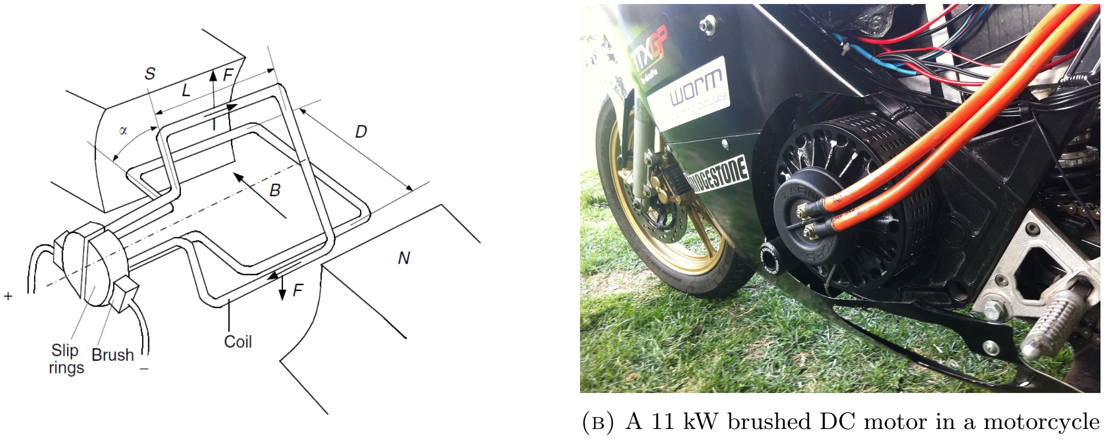

(A) Basic arrangement of a Brushed DC Motor [7]

(B) A 11 kW brushed DC motor in a motorcycle [8]

Figure 2.1: Brushed DC motor

The torque produced by the rotor can be modeled by the Lorentz force, the force on a moving charge in a magnetic field:

$$\vec{F} = \vec{I}L_{\mathrm{A}} \times \vec{B} \tag{2.1}$$

For a winding of length L_{A}, radius of rotation r and N turns, at an angle α to the stator field, the torque produced is given as

$$T = NBIL_{\mathrm{A}}D\cos\alpha = NBIA\cos\alpha \tag{2.2}$$

thus, torque production is proportional to the area A formed by the winding, equating the design value of both diameter and axial length [7]. Under a fixed voltage, current is limited by back-electromotive force (BEMF) due the relative motion of the armature coils and the stator field:

$$BEMF = \frac{d\lambda}{dt} = \frac{d}{dt}NBAsin(\omega t) = NBA\omega cos(\omega t) \tag{2.3}$$

The armature is conducting only when $\alpha \approx 0$, simplifying the torque and Back-EMF expressions to:

$$T = NBAI \ , \ BEMF = NBA\omega \tag{2.4}$$

$$I = \frac{V_{\mathrm{DC}} - BEMF}{R_{\mathrm{A}}} \tag{2.5}$$

thus, torque production diminishes as shaft speed increases. The maximum torque of the machine is limited by the temperature of the armature windings, which is sensitive to the heat removal inside the casing. The thermal limitations, along with brush maintenance, are what limit the popularity of BDC machines in modern LEV powertrains.

2.2.2 Permanent Magnet Synchronous Machines

The PMSM operates on the same torque production principles as the BDC machine, however places the windings on the stator and permanent magnets on the rotor. Commutation is achieved through power electronics, allowing for a higher degree of control over the machine. Periodic excitation of the stator coils produces a rotating magnetic field (RMF), which is synchronized to the rotor magnetic field to produce torque. Although three-phase is typical, polyphase machines have been proposed in literature in effort to increase fault tolerance or reduce torque ripple for traction applications [9]. Heat may be removed through direct conduction to the stator casing, and accelerated through use of liquid coolant channels. The high power density and high efficiency are what allow the PMSM to be so widely used in LEV traction applications, however prior to modern power electronics and embedded controls, the electrical commutation was not feasible. The PMSM family may be classified into surface permanent magnet (SPM) and interior permanent magnet (IPM) types indicating the mounting method of the magnets to the rotor. This classification changes the operating characteristics of the machine. Figure 2.2 illustrates the key difference in rotor geometry.

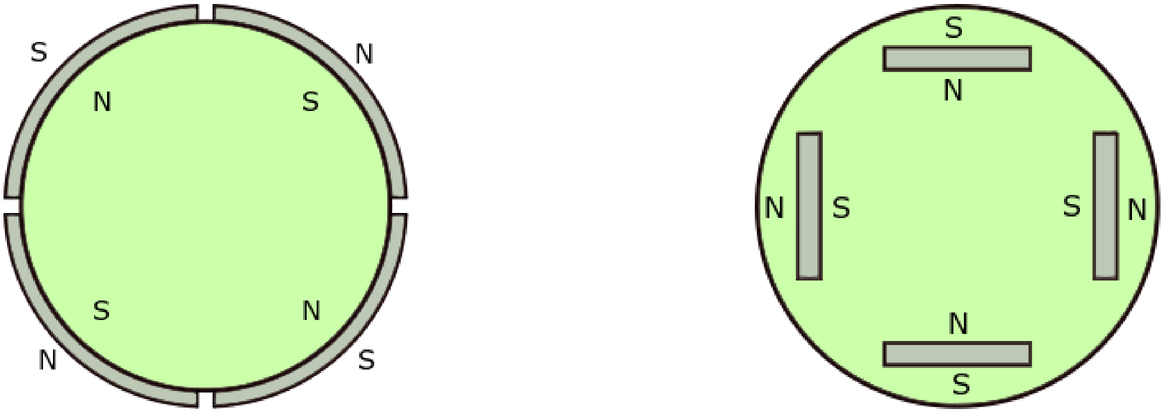

(A) SPM (B) IPM

Figure 2.2: Surface PM and Internal PM Machines

Note that in 2.2b, the rotor has areas where the steel is removed, creating higher reluctance paths through the rotor. This saliency creates reluctance torque which is a key performance advantage of the IPM. However, the manufacturing of the IPM is more problematic, due to the magnet insertion process. Additionally, pockets weaken the rotor, limiting high-speed operation.

2.2.3 Induction Machines

The IM is favoured due to the cost effectiveness and robust design over PMSM, however the power factor is lower due to the rotor magnetization, which leads to lower power density. The stator is identical to the PMSM in construction, however the rotor consists of conducting bars embedded in a steel lamination stack. The stator RMF production is the same as the PMSM, however the rotor speed must be slower from the RMF speed to produce motoring torque. For applications such as e-bikes where the electric powertrain may be shut off and freewheel, the induction motor offers the benefit of no cogging torque or iron loss when idling. Although the induction motor has been applied in many EV applications, the mainstream LEV market has not seen many instances. One exception is the Renault Twizy, a classified heavy quadricycle that employs a 12 kW induction motor.

2.2.4 Switched Reluctance Machines

The SRM is a promising candidate for LEV propulsion in terms of cost minimization. Although the efficiency is lower than a permanent magnet machine due to the need to excite the rotor field, the constant power range is longer and higher speeds are achievable without the injection of field weakening current. The lack of rare earth material or rotor conductor improves the duty cycle of the SRM allowing for longer periods of higher than nominal output power. External rotor SRMs have been designed for in-wheel E-bike applications in [10] and [11] among others. Effort is underway to reduce the torque ripple and acoustic noise of the SRM. The electromagnetic modelling of the SRM will be discussed further in Chapter 3.

2.3 Requirements for a LEV Traction Motor

2.3.1 Cost Minimization

With cost as the main barrier to adoption for electrified powertrains, their design should be centered around cost at production scale. All raw materials, manufacturing processes and assembly must be optimized in order to achieve a competitive price point. Active materials in traction motors include copper, steel and permanent magnet material. [12] provides active material masses for three 30 kW machines designed in FEA. Using historical raw material cost data, the machines active material cost is plotted in Figure 2.3.

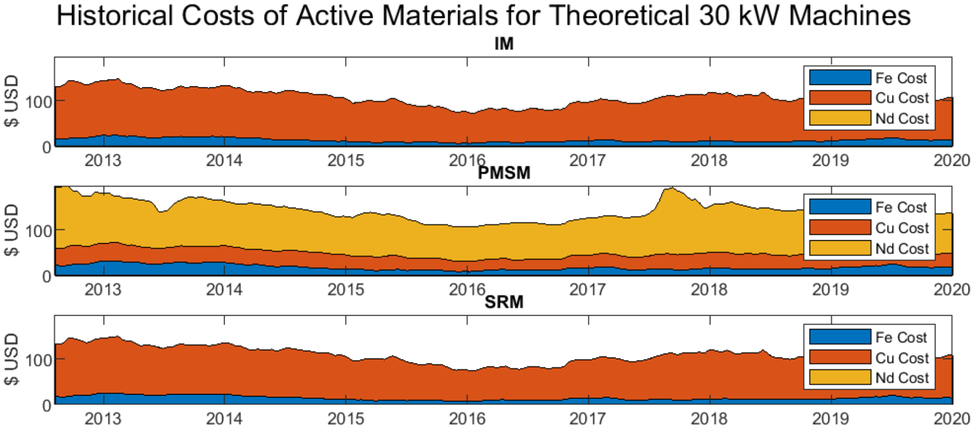

FIGURE 2.3: Material cost breakdown for three 30 kW machines [12] [13] [14] [15]

2.3.2 Torque Quality

Rider comfort is another key design requirement which stems from the competitive advantage over internal combustion engine (ICE) powertrains. Acoustic noise and vibration are contributors to passenger discomfort and should be minimized. Torque ripple is undesirable in electrified powertrains, as this contributes to longitudinal vibration. Longitudinal vibrations may contribute to premature wear of components in the driveline, and introduce the potential for resonant interaction with the vehicle structure at certain operating frequencies [16].

2.3.3 Power Density and Specific Power

The power density of an electric machine is defined as the mechanical power produced by the shaft per unit mass of the machine, whereas specific power is related to the volume. Both power density and specific power are limited by the machine's ability to dissipate heat generated by the losses [17]. This presents two separate design challenges, the first to maximize the efficiency of the machine as to minimize heat generation and the second to effectively remove heat from the source of losses. While copper losses make up the majority of loss, it is also the easiest to remove in AC machines, given the direct heat path to the machine casing. For power-dense machines, liquid cooling is imperative to sustain high currents in the windings. The armature windings of DC machines and the rotor bars of induction machines do not easily benefit from liquid cooling as it is often not practical to pump coolant onto the rotor.

2.3.4 Efficiency and Losses

For onboard applications, scarce battery energy must be used as effectively as possible. Modern power electronics exhibit a higher peak efficiency and wider high-efficiency range compared modern traction motors, leaving the motor as the main bottleneck for effective energy use [18][19]. The efficiency of an electric machine is defined as:

$$\eta = \frac{P_{\text{out}}}{P_{\text{in}}} = \frac{\tau\omega}{VI} \tag{2.6}$$

where $\tau\omega$ is the product of the torque and angular frequency and VI is the product of the DC voltage and current feeding the system. It is often useful to instead express the efficiency as the ratio of output power to the sum of output power and the losses:

$$\eta = \frac{\tau\omega}{\tau\omega + P_{\text{loss}}} = \frac{\tau\omega}{\tau\omega + P_{\text{copper}} + P_{\text{Iron}} + P_{\text{mech}}} \tag{2.7}$$

where P_{copper} is the resistive loss in the copper conductors, P_{iron} is the loss associated with Eddy currents and hysteresis losses in the magnetic materials, and P_{mech} is the loss due to friction of the bearings and the aerodynamic drag on the rotor known as windage.

2.4 Vehicle Model for Motor Sizing

The torque and speed operating point of a traction machine depends on the drive cycle conditions. The shaft speed of the machine depends on the wheel speed and the gear ratio between the motor and wheel. The torque depends on the road loads on the wheel, and the efficiency of the driveline to the motor. Road loads can be summarized with the following definitions:

- Acceleration force depends on the time rate of change of velocity $\frac{dv}{dt}$, the vehicle mass M and the rotating component factor δ_{R}, which represents the apparent mass of the vehicle due to rotating driveline components whose angular velocity is proportional to the vehicle speed:
$$F_{\text{A}} = \delta_{\text{R}} M \frac{dv}{dt} \tag{2.8}$$
- Climbing Force is required to overcome grade and is equal to the vehicle mass M, the gravitational acceleration g and the sine of the climb angle α_{c}
$$F_{\text{C}} = M g sin \alpha_{\text{c}} \tag{2.9}$$
- Drag Force is the force to overcome aerodynamic forces in the longitudinal direction of vehicle travel. It depends on the density ρ_{air} of the air (typically $1.22 kg/m^3$), the vehicle frontal area A_{f}, coefficient of drag C_{D} and the square of the velocity:
$$F_{\text{D}} = \frac{1}{2} \rho_{\text{air}} C_{\text{D}} A_{\text{f}} v^2 \tag{2.10}$$

- Rolling resistance force represents the forces necessary to overcome the damping effects of the tire as it rotates. While many models exist to capture the viscoelastic effects of tire compression, a simplified linear model will suffice for powertrain sizing purposes. C_{R0} and C_{R1} may be defined to represent the static and velocity-dependent rolling resistance coefficients:

$$F_{\mathrm{R}} = Mg(C_{\mathrm{R0}} + C_{\mathrm{R1}}v) \tag{2.11}$$

In summary, longitudinal wheel force can be estimated over a velocity and grade schedule $v(k)$ and $\alpha_{\mathrm{c}}(k)$:

$$F_{\mathrm{Wheel}}(k) = \delta_{\mathrm{R}} M \frac{v(k) - v(k-1)}{dt} + Mgsin\alpha_{\mathrm{c}}(k) + \frac{1}{2}\rho_{\mathrm{air}} C_{\mathrm{D}} A_{\mathrm{f}}(v(k))^2 + Mg(C_{\mathrm{R0}} + C_{\mathrm{R1}} v(k)) \tag{2.12}$$

The vehicle model is implemented in the MATLAB/Simulink environment. The drive cycle is tracked with a PID controller, whose output is a torque request. The vehicle acceleration is calculated from a summation of road forces and the torque applied by the wheel. The torque request is an input to the torque controller, which passes the requested torque to the motor block, and splits braking requests into regenerative braking and friction braking. The high-level block diagram is shown in Figure ??.

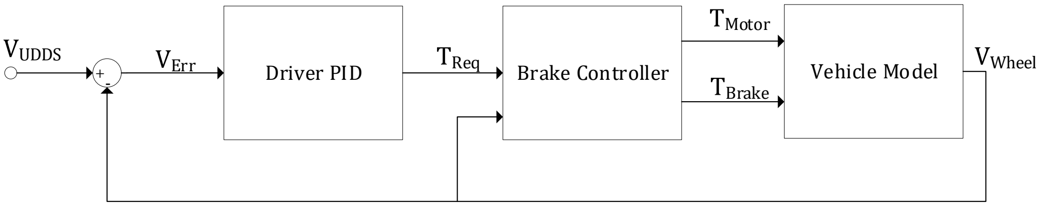

FIGURE 2.4: Vehicle model block diagram

The blended braking strategy should reflect the limitations of regenerative braking at low speeds. To accomodate for low BEMF and therefore poor braking performance at low speeds, the vehicle controller block applies a lookup table which reduces motor braking torque at low speeds. The difference between the requested braking torque and the reduced torque the motor can apply is applied in the form of friction brakes. This logic is reflected in the block diagram in Figure 2.5

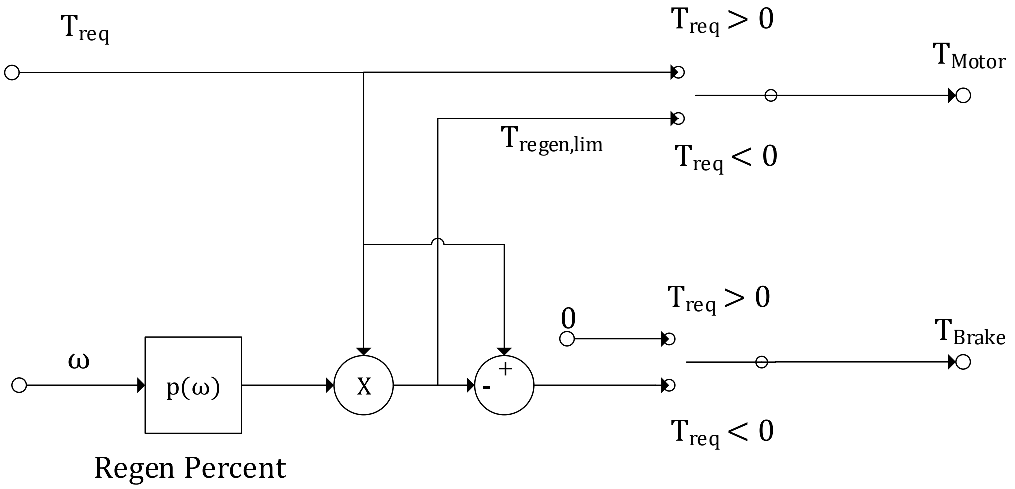

FIGURE 2.5: Blended braking block diagram

The gearbox is represented by a reduction in speed and an amplification in torque with an applied efficiency:

$$T_{\text{Wheel}} = T_{\text{motor}} N_{\text{GB}} \eta_{\text{GB}} \;\; , \;\; \eta_{\text{GB}} = \begin{cases} \eta_{\text{GB}} & \text{if } T_{\text{Wheel}} > 0 \\ \frac{1}{\eta_{\text{GB}}} & \text{if } T_{\text{Wheel}} < 0 \end{cases} \tag{2.13}$$

A small e-motorcycle or e-rickshaw is an application of interest. Such a vehicle would be expected to have parameters contained in Table 2.2

The velocity schedule, or drive cycle, should be selected to reflect the typical and worst-case operating conditions of the vehicle. For an urban LEV such as an e-moped or e-tuktuk, typical conditions of stop-and-go, short grade ascents and occasional high-speed cruising should be expected. The urban dynamometer driving schedule (UDDS) is used for

Parameter	Symbol	Value
Drag Coefficient	C_{D}	0.5
Frontal Area	A_{f}	1 m^2
Mass	M	200 kg
Rotating component factor	δ_{R}	1.05
Gearbox ratio	N_{Gear}	7.5:1
Gearbox efficiency	η_{Gear}	0.95
Wheel radius	r_{wheel}	0.25 m
Static rolling resistance coefficient	C_{R0}	0.015
Dynamic rolling resistance coefficient	C_{R1}	0.00001

TABLE 2.2: Typical LEV parameters used for traction motor sizing

emissions testing to represent city driving for passenger vehicles. It features 12 km of driving, with speeds up to 88 km/h. For an LEV, the speed should not exceed 60 km/h, therefore the UDDS must be scaled down to approximately 68%. Another driving cycle, the New York City cycle (NYCC), represents a lower speed, intermittent drive designed to reflect higher volume traffic, up to 40 km/h. Therefore, a combination of UDDS and NYCC can be used to simulate typical and maximum conditions for a LEV. The combined drive cycle is plotted in Figure 2.6. The probability density of each operating point can be visualized in Figure 2.8.

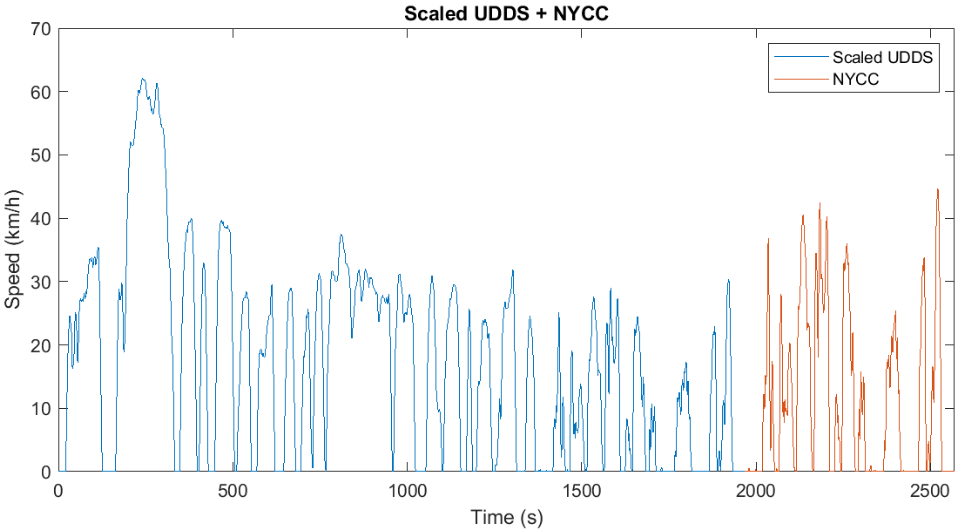

FIGURE 2.6: Combined scaled UDDS and NYCC

This drive cycle was simulated in the vehicle model for $\alpha_c = 0°$, $\alpha_c = 2°$ and $\alpha_c = -2°$. The shaft torque and speed can be seen in Figure 2.7.

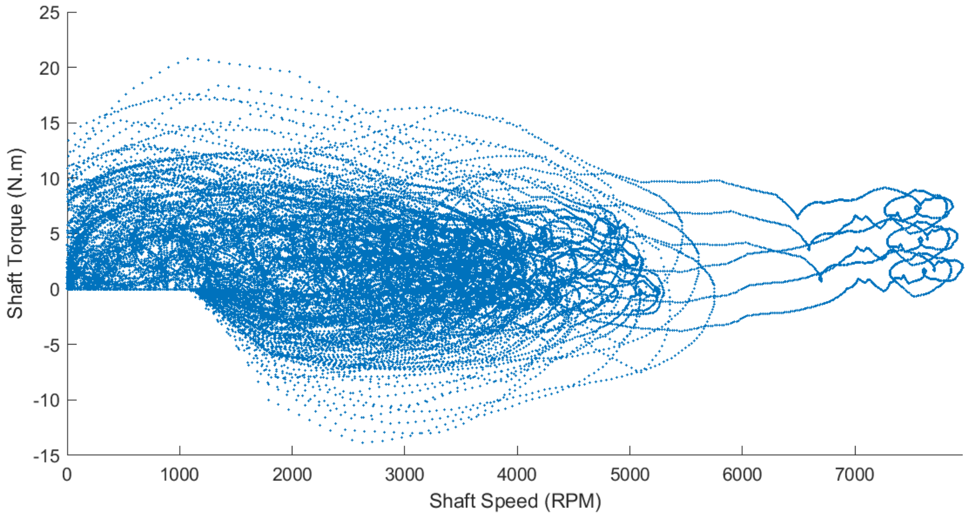

FIGURE 2.7: Shaft torque and speed for 3 combined drive cycles

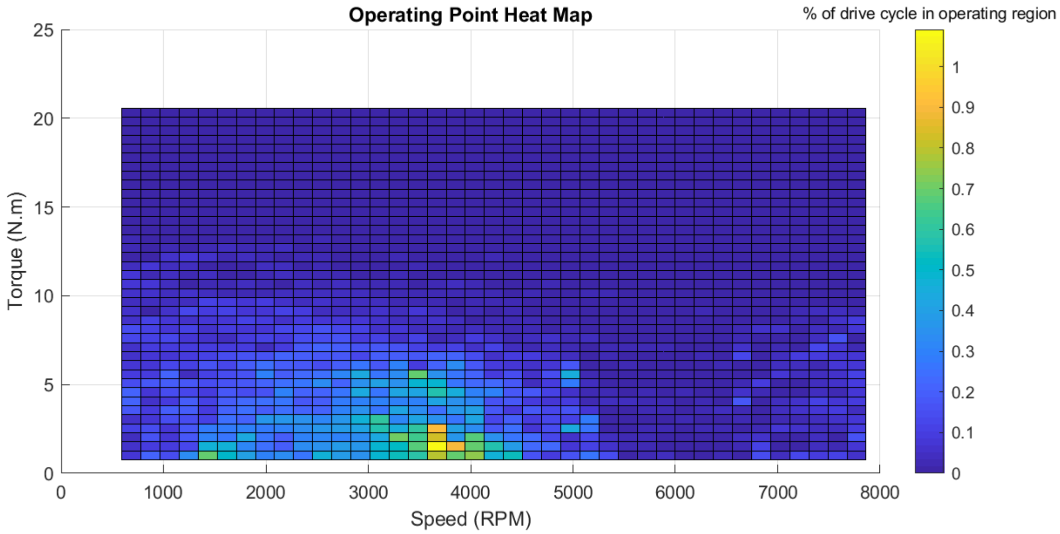

FIGURE 2.8: Operating point heat map

In the interest of energy savings, the motor design should be optimized to exhibit the best efficiency at the most common operating points, weighting the operating point probability by the power required. Scaling the weight by the timestep puts the metric in units of energy. The energy use map for the drive cycles can be seen in Figure 2.9.

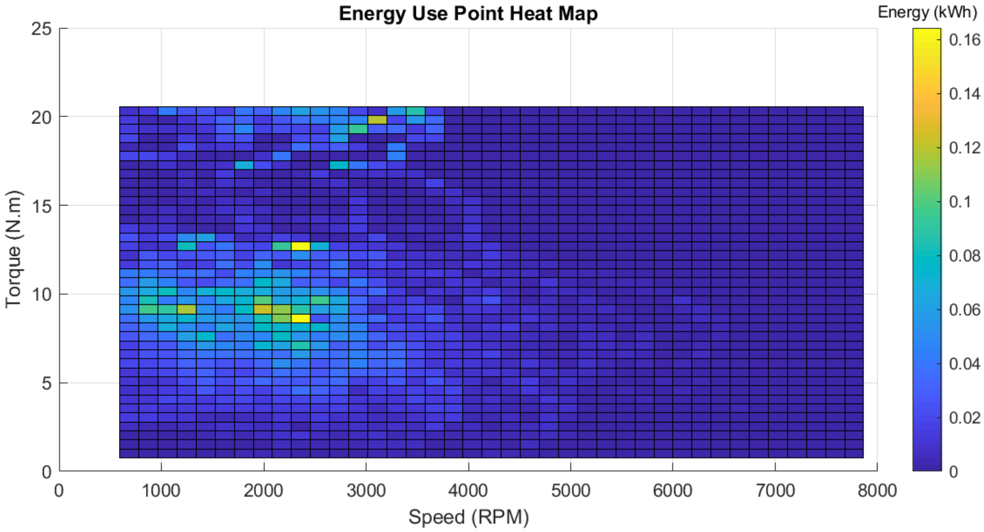

FIGURE 2.9: Operating point heat map

Based on the energy use map, some targets may be defined for the motor. The targets can be summarized in Table 2.3 and Figure 2.10

Parameter	Target
Continuous Torque	9 $N.m$
Continuous Power	3.7kW
30 s Torque	14 $N.m$
30 s Power	6.3kW
Max speed	8000 RPM
Base speed	4000 RPM
Efficient operating point	8 $N.m$, 2250 RPM

TABLE 2.3: LEV motor performance targets

Figure 2.10: Motor Torque-Speed Target Curves

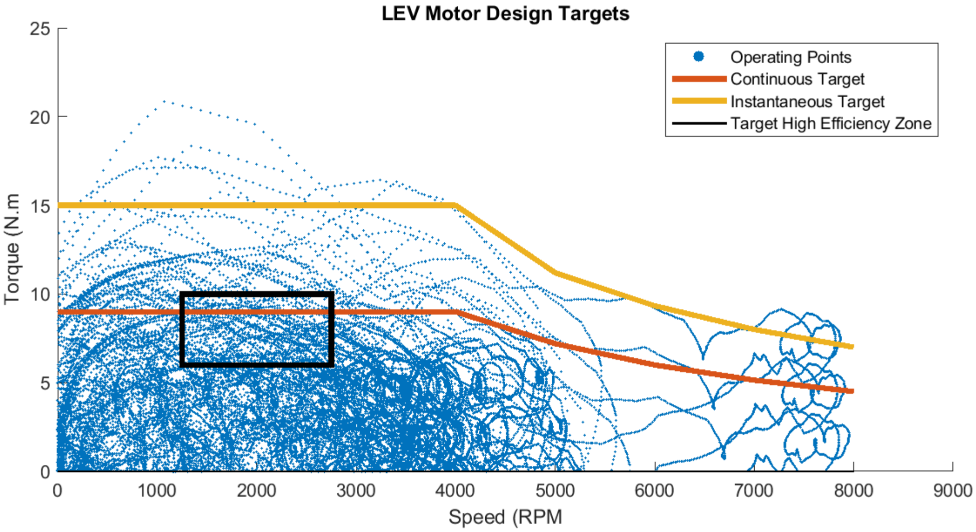

Chapter 3

Introduction to Axial Flux Switched Reluctance Motors

The switched reluctance machine (SRM) is gaining traction as a viable candidate for vehicle propulsion due to it's wide speed range, robust construction and lack of rare-earth materials. The SRM operates on the principle of varying magnetic reluctance, or the tendency for magnetic flux to take the path of least resistance. Torque is produced by the attraction of rotor-mounted steel teeth (poles) to the stator mounted poles with sections of wound conductor. Current is switched between stator windings to produce continuous torque. SRMs are defined by the number of stator and rotor poles, generally written as X/Y, where X is the number of stator poles and Y is the number of rotor poles. For example, an 8/6 machine has 8 stator poles and 6 rotor poles. The rotor of a SRM is entirely steel construction, eliminating conduction losses associated with induction machines, and allowing for a more robust and simple to manufacture rotor. The simplified rotor also allows for higher-speed operation, without the risk of structural failure due to weaker sections of rotor associated with permanent magnets. The stator shares similarities to other brushless machines, however poles are typically wound as concentrated, fractional slot windings.

3.1 Electromagnetic Principles of Switched Reluctance Motors

The first-quadrant operation of the SRM behaves like a magnetic circuit of decreasing overall reluctance as the rotor pole nears the stator pole. The position in which the rotor pole makes the lowest reluctance path is known as the aligned position, at which no torque is produced. The unaligned position is the midpoint between two adjacent stator poles, which is the lowest inductance, or highest reluctance position. In Figure 3.1 a, the rotor is aligned with phase A and an excitation of phase C would proceed the rotor to rotate clockwise.

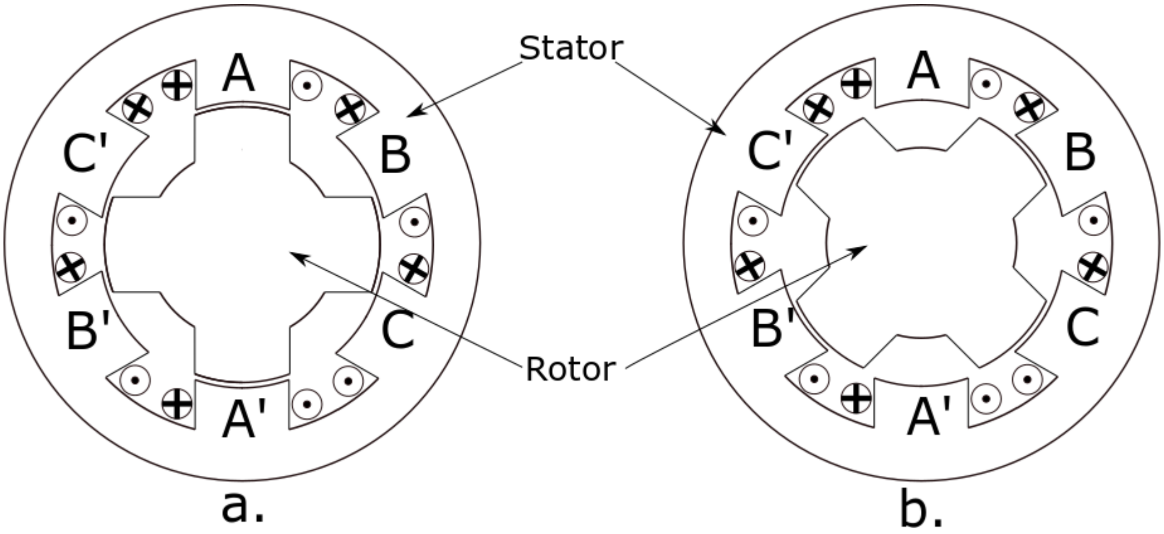

FIGURE 3.1: a. Aligned with phase A. b. Unaligned with Phase A

3.1.1 Electromechanical Energy Conversion

The energy conversion process in SRMs is rooted in the conversion of electromagnetic co-energy into mechanical energy [4]. This can be understood by the exchange between electrical, mechanical and stored magnetic energy:

$$W_{\text{Elec}} = W_{\text{Field}} + W_{\text{Mechanical}} \tag{3.1}$$

Under constant current excitation, a magnetic system is said to store magnetic energy W_f

$$W_\mathrm{Field} = \int i d\lambda \tag{3.2}$$

where λ is the coil flux linkage, represented in units of Weber-turns. The flux linkage represents the flux that would cause the equivalent voltage behaviour if only one loop of conductor surrounding the flux was considered. The magnetic field energy can be represented graphically in the $\lambda - i$ space, shown in Figure 3.2. A curve on this plane can represent a magnetic system where the current or flux linkage change with time. The complement to magnetic field energy is known as coenergy, which is the area below the $\lambda - i$ curve.

$$W_\mathrm{C} = \int \lambda d i \tag{3.3}$$

Both coenergy and field energy are magnetic quantities due to the presence of magnetic flux. The total magnetic energy may be expressed as their sum, represented by the rectangular area on the $\lambda - i$ space.

$$W_\mathrm{Field} + W_\mathrm{C} = \lambda i \tag{3.4}$$

The torque produced in a rotational magnetic system can be expressed as the angular rate of change of coenergy:

$$T = \frac{dW_\mathrm{C}}{d\theta} \tag{3.5}$$

Due to magnetic saturation, the coenergy integral begins to exceed the field energy integral as $\frac{d\lambda}{di}$, or inductance, decreases. Therefore, the SRM benefits from operating in the saturated region of the core material. The voltage in an SRM can be expressed as the resistive voltage drop in the winding and the flux linkage rate of change:

$$V = iR + \frac{d\lambda}{dt} \tag{3.6}$$

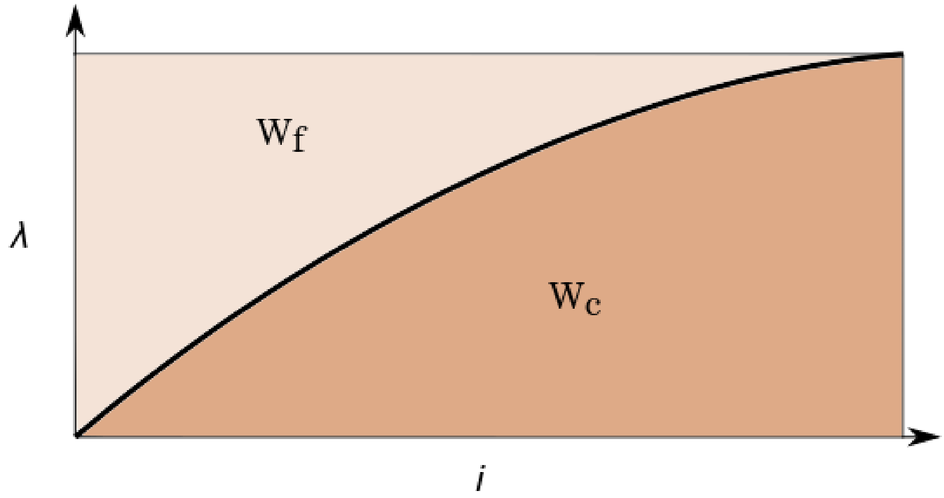

FIGURE 3.2: Energy in a magnetic system

where λ may be expressed as Li. However, with both changing inductance and changing current in the SRM phase, the voltage is separated into two terms using chain rule:

$$\frac{d\lambda}{dt} = L(\theta)\frac{di}{dt} + i\frac{dL(\theta)}{dt} \tag{3.7}$$

Thus the power in an SRM can be expressed as:

$$iV = i^2R + \frac{d}{dt}\frac{1}{2}i^2L(\theta) + \frac{1}{2}i^2\frac{dL(\theta)}{d\theta}\omega \tag{3.8}$$

where the first term represents resistive power lost, the second represents stored energy, and the third represents mechanical power.

$$\tau\omega = \frac{1}{2}i^2\frac{dL(\theta)}{d\theta}\omega \ \ , \ \ \tau = \frac{1}{2}i^2\frac{dL(\theta)}{d\theta} \tag{3.9}$$

Thus the torque is proportional to the angular rate of change of inductance and is current polarity agnostic.

3.1.2 SRM Control

The SRM may be controlled by any topology of electrical drive that controls phase currents independently. The asymmetric bridge converter, shown in Figure 3.3 uses two switches and two diodes per phase, allowing for fewer components than the full bridge converter.

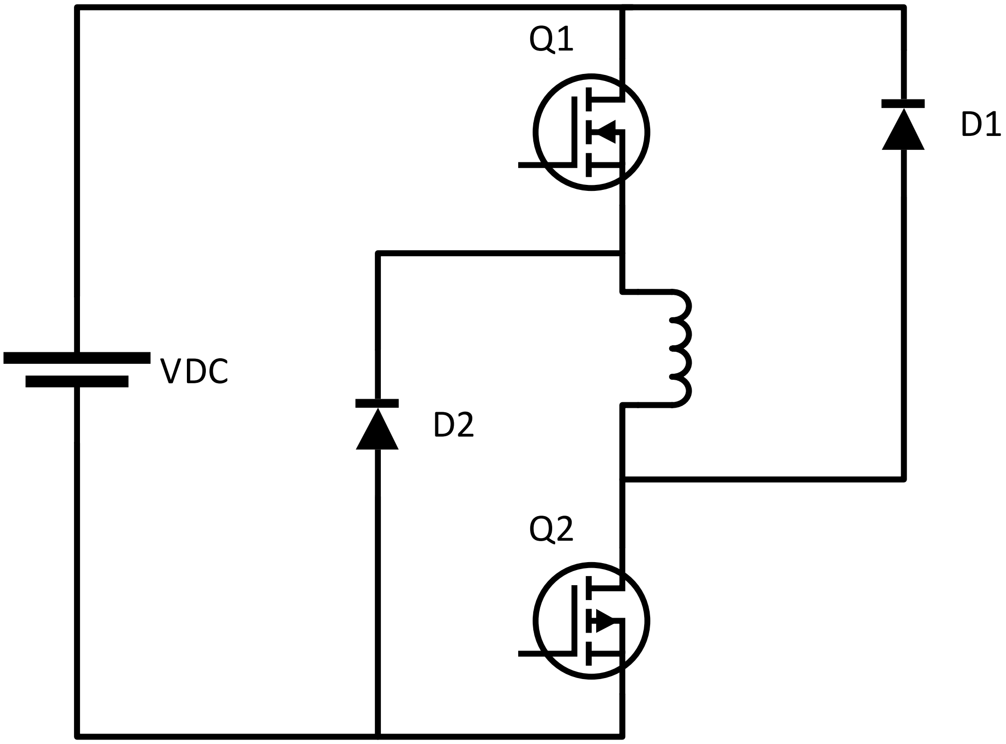

Figure 3.3: Asymmetric bridge converter for one phase

A phase can be switched on by activating both switch Q1 and Q2. Either switch may be opened to cause the phase to freewheel through the other switch (soft-switching), or both switches may be opened to forward bias both diodes and reverse the polarity of the phase (hard-switching). The converter modulates between on state and off state according to a hysteresis band around a target current, with feedback from individual current sensors. The

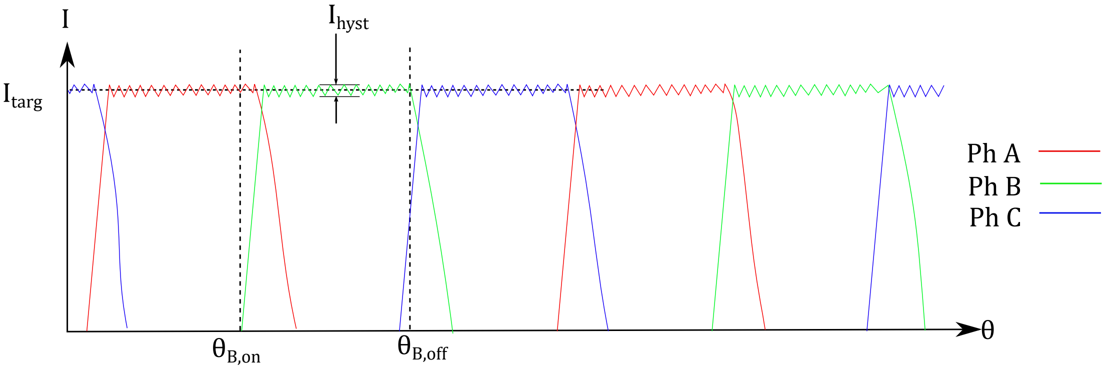

(A) Low speed

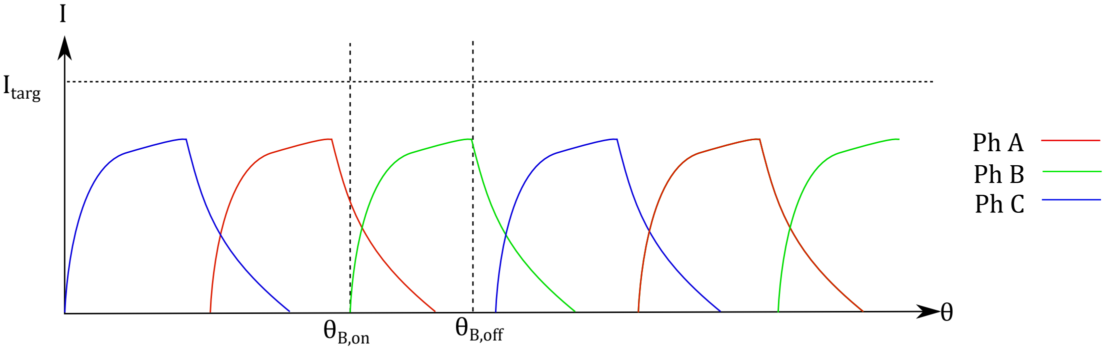

(B) High speed

Figure 3.4: SRM phase currents at low and high speed

switching angles may be determined by an offline optimization that uses experimental or FEA data to meet a maximum performance target, such as torque ripple or efficiency. At low speed, where $\frac{d\lambda}{dt}$ is minimal, the current is not naturally limited by induced voltage, and rises quickly. Since induced voltage is a function of both flux and speed, the base speed is dependent on the target current. At the base speed, a portion of the conduction cycle will not achieve the target current due to induced voltage. At speeds above the base speed, the target current might not be reached at all. An example of SRM phase currents is plotted in Figure 3.4. At low speed, the controller switches the current on and off to maintain a constant current of $\mathrm{I}_{\mathrm{targ}}$. Deviations from $\mathrm{I}_{\mathrm{targ}}$ are due to the hysteresis band defined by the controller. At high speed, the converter operated in single-pulse mode, as the target current is never reached. This is what gives the shape to a typical torque-speed curve. This behaviour is also what drives the need for dynamic switching angles, such as to advance the turn on of the phase at higher speed in order to magnetize the phase.

3.1.3 Losses

The SRM experiences a number of losses in the process of energy conversion. Copper and iron loss are the principle sources of electromagnetic energy loss. Copper loss is the result of current, and dominates in the high-torque region of the torque-speed curve. Iron loss is the result of changing flux density, and dominates in the high-speed region of the motor operation.

3.1.3.1 Copper Loss

The DC copper loss, is due to the resistivity of the winding and is proportional to the square of the current:

$$P_{\text{Copper}} = {I_{\text{RMS}}}^2 R_{\text{Phase}} N_{\text{Phase}} \tag{3.10}$$

where I_{RMS} is the root mean square current, R_{phase} is the phase resistance and N_{phase} is the number of phases. At high frequency, eddy currents in the conductor cause the effective conductor area to be reduced to the edge, increasing apparent resistance. The skin depth is considered the depth from the conductor surface where current density has decreased to 37% of the surface value, and can be calculated as:

$$\delta = \sqrt{\frac{2\rho}{\omega\mu}} \tag{3.11}$$

where μ, ρ are the permeability and resistivity of the conductor and ω is the angular frequency of the current. To ignore the skin effect, the conductor radius must be smaller than the skin depth [20]. Reducing the ratio of the conductor area to its perimeter can reduce the cross sectional utilization of the conductor, achievable by using more parallel strands of conductor in the winding. The other phenomenon that contributes to AC copper losses is the proximity effect, or the tendency for adjacent conductors to induce losses in each other. The computation of proximity effects requires geometry-dependent derivations, achievable with FEA or analytical models for predefined winding patterns. For orthogonal arranged circular conductors, the ratio $F_{\mathrm{R}} = \frac{R_{\mathrm{AC}}}{R_{\mathrm{DC}}}$ can be found by applying Dowell's equation which combines the skin effect and proximity losses in conductors:

$$F_{\mathrm{R}} = A\left(\frac{sinh(2A) + sin(2A)}{cosh(2A) - cos(2A)} + \frac{2{N_{\mathrm{l}}}^2 - 1}{3}\frac{sinh(A) - sin(A)}{cosh(A) + cos(A)}\right) \tag{3.12}$$

where $A = \sqrt{\eta_{\mathrm{w}}}\frac{h}{\delta}$ and the porosity factor η_{w} is a conductor geometry dependent term, which is generally a ratio of the conductor size to its winding pitch, and $\frac{h}{\delta}$ is the ratio of the conductor height to the skin depth at a given frequency [21]. The Dowell equation is applicable to sinusoidal currents, however Fourier decomposition may be employed to calculate losses at higher harmonics, particularly critical for inverter-fed machines [22].

3.1.3.2 Iron Loss

Iron loss is an unavoidable consequence of passing magnetic fields through ferromagnetic materials. While many iron loss models have been proposed, all suggest elements of eddy currents and hysteresis effects that are responsible for the losses. A third component, the excess loss, is said to be responsible for measured losses that cannot be mathematically attributed to eddy currents of magnetic hysteresis. For this reason, excess loss is often mischaracterized as being anomalous. Eddy current losses result from Faraday's law which states a changing magnetic flux will produce an electric field, which in conductive materials results in a circulating eddy current. In RFSRMs, the rotor and stator are laminated to reduce the path lengths of the eddy currents, increasing overall resistivity in the axial direction. The eddy current loss is shown to increase with lamination thickness δ_{lam}, due to the larger macroscopic region that encloses time changing flux, as well as the frequency f and magnitude of flux density B_{max} in the material [23] :

$$P_{\mathrm{ec}} = K_{\mathrm{ec}}(B_{\mathrm{max}}f\delta)^2 \tag{3.13}$$

where K_{ec} depends on the material properties, such as resistivity. The hysteresis losses are due to the alternating nature of flux density in the magnetic material, which requires energy to magnetize and demagnetize regions of the material. The hysteretic energy depends on the flux density B raised to the Steinmetz coefficient α. Thus, the general form for hysteresis loss under sinusoidal excitation can be expressed as:

$$P_{\text{hyst}} = K_{\text{hyst}} f B^{\alpha_{\text{hyst}}} \tag{3.14}$$

The exponent α_{hyst} was first proposed by Steinmetz as 1.6 [24], however is often determined to be closer to 2 [25]. The excess losses are considered to be attributed to eddy currents that are the result of the discontinuous increases in flux density due to Barkhausen jumps [26]. Experimental data has shown that the excess loss is a 1.5th order function of frequency and flux density:

$$P_{\text{excess}} = K_{\text{excess}} f^{1.5} B^{1.5} \tag{3.15}$$

Iron loss models may be provided by manufacturers in the form of a series of coefficients pertaining to the aforementioned loss quantities, or a series of curves that result from power loss measurements at various frequencies and flux densities. However, many of these models are idealized, and manufacturing processes such as stamping and laser cutting may degrade the material properties, particularly on the edges where flux concentrates, resulting in relatively uncertain loss estimations in electric machines [27]. FEA may be used to compute element-wise iron loss given a profile of flux density over time. Nonsinusoidal flux profiles may be decomposed into harmonic components and summed in the frequency domain.

3.1.3.3 Mechanical Losses

Mechanical losses are power losses that can be attributed to friction, such as bearing friction loss or aerodynamic (windage) loss. Mechanical losses are suggested to account for approximately 10% of total motor power loss [23]. Global bearing manufacturer SKF proposes a model for bearing losses that accounts for rolling friction, sliding friction, friction of seals and viscous friction inside the bearing [28]. The magnitude of bearing friction depends on the materials, geometry and lubrication of the bearing, as well as radial and axial loading. Experimental friction data is available from bearing manufacturers and can be used in the design process.

Windage loss is highly dependent on the surfaces of rotor and stator. In air-cooled motors, a deliberate reduction in windage loss would reduce the cooling capability of the motor. The SRM is particularly exposed to high windage losses due to the salient rotor and stator poles. It has been proven that filling the spaces between rotor poles can reduce windage losses at high speed [29]. One model suggests the windage loss in a radial flux motor can be estimated by [30]:

$$P = k_{\mathrm{r}} \pi f \rho \omega^2 {r_{\mathrm{rotor}}}^4 l \tag{3.16}$$

where $\mathrm{K_r}$ is a roughness coefficient, f is a friction coefficient r, l are the rotor dimensions,ρ_{air} is the air density and ω is the angular velocity of the rotor. For a flat surface axial flux motor, the windage loss can be estimated as:

$$P = \frac{\pi \mu_{\mathrm{air}} \omega^2 ({r_{\mathrm{o}}}^4 - {r_{\mathrm{i}}}^4)}{2 l_{\mathrm{ag}}} \tag{3.17}$$

where μ is the dynamic viscosity of the air, and $\mathrm{l_{ag}}$ is the airgap length. While these two expressions fail to account for complexities such as surface features, it can be concluded that windage loss has the potential to affect high surface speed machines due to the quadratic and quartic dependencies on speed and radius, respectively.

3.2 SRM Modelling

FEA is useful for determining the geometry-dependent characteristics of the motor, however can be tedious for simulating the dynamic performance with the integration of control. A dynamic model can be constructed based off the voltage equation for the SRM and lookup tables for torque and flux linkage. The voltage equation of the SRM phase can be rearranged to solve for flux linkage:

$$\lambda = \int V - IR \tag{3.18}$$

Where λ is a function of position and current. If the flux linkage map is generated from FEA, it may be inverted numerically to solve for current given a flux linkage and position:

$$\lambda(i, \theta) \rightarrow i(\lambda, \theta) \tag{3.19}$$

The torque can be calculated with another lookup table. The SRM phase model in Simulink is shown in Figure 3.5. The discrete time model is setup to receive the voltage and position, and output a phase current and torque.

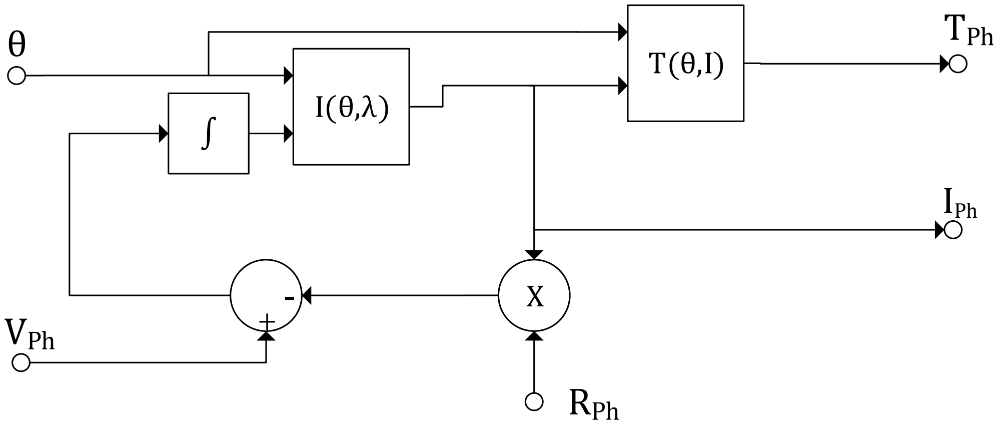

FIGURE 3.5: Energy conversion model for one phase of the SRM with lookup tables

Multiple phases are set up to receive independent voltages from a controller. The torque of each phase is summed to represent full rotor torque.

3.3 Axial Flux Motors

The vast majority of electric machines produced in history can be classified as radial-flux machines (RFM). The magnetic flux in RFMs is predominantly in the plane perpendicular to the axis of rotation of the shaft. The structure of a RFM is defined as concentric rotor and stator. An axial-flux machine (AFM) alternatively employs disc-shaped, coplanar rotor and stator. While the airgap of a RFM takes the shape of a cylinder, the airgap of an AFM takes the shape of a disc. The machine torque can be calculated with the airgap dimensions and σ_{t}, the tangential component of the Maxwell Stress Tensor, which can be calculated by the airgap flux density B if decomposed into radial and tangential components:

$$\sigma_{\mathrm{t}} = \frac{1}{\mu_0}(B_{\mathrm{r}}B_{\mathrm{t}}) \tag{3.20}$$

The torqe of a radial-airgap machine of airgap diameter D_{A} and axial length L is:

$$T_{\mathrm{RF}} = \frac{{D_{\mathrm{A}}}^2\pi L}{2}\sigma_{\mathrm{t}} \tag{3.21}$$

The torque of an axial-airgap machine of inner and out diameters D_I and D_O is given as:

$$T_{\mathrm{AF}} = \frac{{D_{\mathrm{o}}}^3 - {D_{\mathrm{i}}}^3}{8}\frac{4\pi}{3}\sigma_{\mathrm{t}} \tag{3.22}$$

This representation of torque shows that torque increases with the volume of the RFM, and the surface area of an AFM airgap. Thus, it is possible to design an AFM that will exceed the torque density of a RFM by increasing the diameter and minimizing the axial length. This axially compact design has established AFMs as promising candidates for in-wheel motors, integrated HEV powertrains and electric motorcycles. Additionally, airgaps may be stacked in the axial direction to increase machine power, giving opportunity to a modular design. The torque production is said to benefit from the longer effective radius of the lever arm, something outer-rotor RFMs exploit but suffer from heat removal problems associated with embedding the stator in a rotating case.

Like RFMs, AFMs can be defined by their electromagnetic principle of operation. Types include, but are not limited to permanent magnet synchronous (AFPMSM), induction (AFIM), flux-switching (FSAFM), brushed DC (AFBDC, or Lynch Motor) and switched reluctance (AFSRM). An AFM may also be categorized by the arrangement of rotor and stator plates, with many stack configurations.

3.3.1 Configurations of AFMs

Numerous configurations of rotor and stator plates are possible for AFMs. Four configurations are listed below, and illustrated in Figure 3.6:

- Single-sided (SS)
- Dual outer stator, inner rotor (OSIR)
- Dual outer rotor, inner stator (ORIS)
- Multi stator, multi rotor (MRMS)

The SS machine has the greatest simplicity and promising thermal management opportunity from the non-active side of the stator. However, the axial forces are unbalanced and require additional stiffness or damping to reduce noise. The OSIR machine also allows for thermal management from the non-active stator side, and balances the rotor forces, which may be more critical than the stator given the additional centrifugal loading on the rotor. Stator windings have more space in the OSIR machine than the ORIS, due to the requirement for pole retention. Thus, a higher fill-factor is possible on OSIR windings.

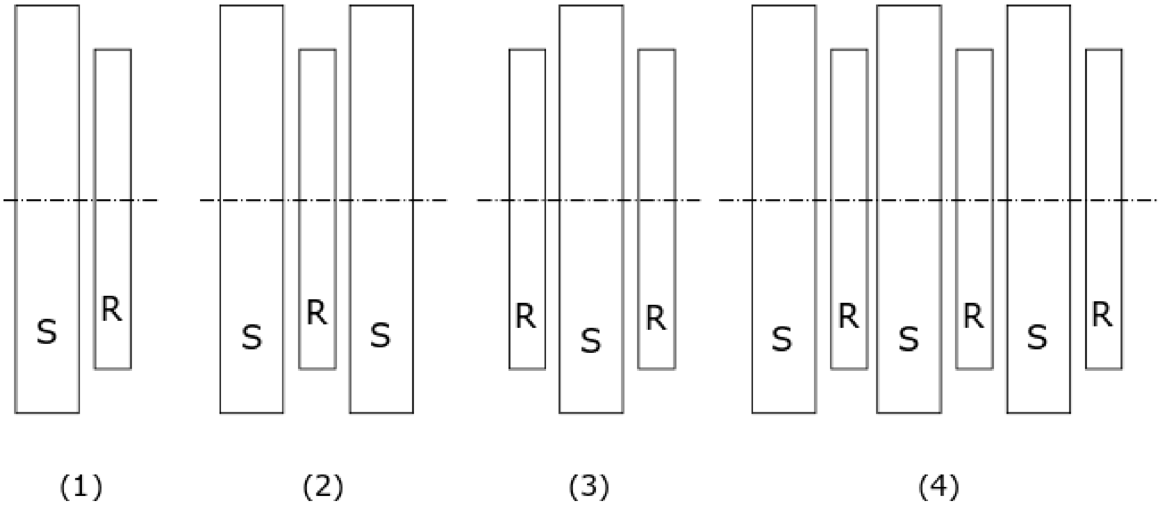

FIGURE 3.6: 1. Single-sided. 2. Outer stator, inner rotor. 3. Outer rotor, inner stator. 4. Multi rotor, multi stator.

3.3.2 Axial-Flux Motors in Industry

While many credit manufacturing difficulties as the main barrier to widespread AFM adoption, several companies have recently emerged with off-the-shelf AFM products. The construction features of commercially available motors are of particular interest for bringing a novel topology to prototype. It must be noted that all of the commercialized AFMs use permanent magnets, and the overwhelming majority are permanent magnet synchronous machines (PMSMs). While the presence of permanent magnets will increase the efficiency due to lack of copper losses associated with field excitation, the rare-earth materials required are costly and subject to high price fluctuations. Permanent magnets also suffer the risk of demagnetization at elevated temperatures, so complex thermal management including temperature estimation is required to fully utilize the PMSM.

3.3.2.1 Avid Technology AF140

Avid Technology (Cramington, UK), produces an OSIR permanent magnet machine, originally developed by EVO Electric Ltd. The motor employs dual wound stator backirons from M330-35A electrical steel [31]. The wound stator allows for cost-effective manufacturing using a stamping process on a continuous band, as illustrated in Figure 3.7. The rotor is comprised of permanent magnets embedded in a composite plate [33]. Cooling is provided by water jackets on the outer axial faces of the motor.

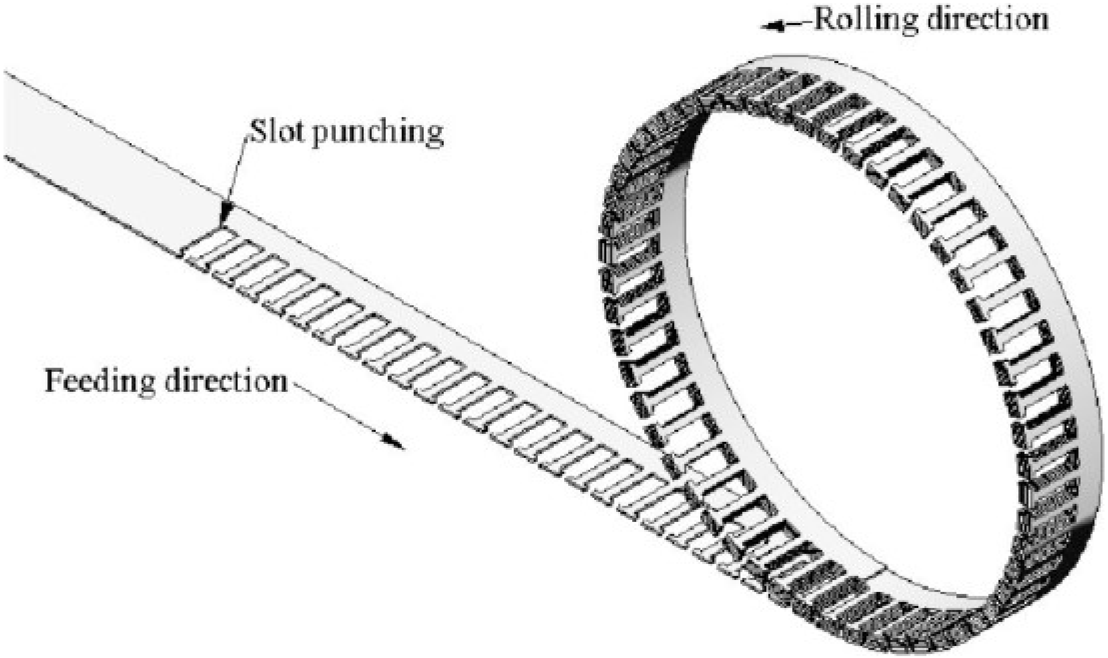

FIGURE 3.7: Winding electrical steel for single-sided or outer-stator AFM stator construction [32]

3.3.2.2 YASA Inc

YASA Inc (Oxford, UK) has developed a product line of high power density permanent magnet AFMs for motorsport. The motors offer a distinct feature of having no stator yoke (no magnetic path between stator poles), which is claimed to reduce iron losses in the stator. The stator core material is soft magnetic composite (SMC), produced by Hoganas AB (Hoganas, Sweden). Windings are circular profile conductor, wound concentrated on each stator pole. Cooling for the windings is provided by direct oil immersion, and additional heat is removed by airflow facilitated by ducts that feed each airgap. Coolant plumbing and phase cables are routed through the outer radius of the machine, while a through-shaft spline profile occupies the inner radius.

3.3.2.3 Emrax 268

Emrax d.o.o (Molkova, Slovenia) offers a series of ORIS motors for use in transportation applications. Unlike other AFPMMs, the rotors of the Emrax 228 are fixed to the case and all coolant plumbing, phase cables and sensor wires are routed through the inner race of the main bearing. Stator core is built using an array of individually sized lamina, stacked to form a wedge [34]. Conductor is circular and wound in concentrated form. Stator poles are held to a central hub by means of aluminum wedges fastened between the poles. The rotating case of the machine is perforated to allow airflow into the airgap.

Table 3.1 below compares three commercially available performance AFMs to a similar grade RFM.

Metric	Remy HVH250	Avid AF140	YASA 750R	Emrax 268
Flux Direction	Radial	Axial	Axial	Axial
Configuration	Inner rotor	Inner rotor	Outer rotor	Outer rotor
Peak Power (kW)	180	220	200	230
Peak Torque (Nm)	310	600	790	500
Mass (kg)	50	42.5	37	20.3
Continuous Torque Density (Nm/kg)	4.2	6.11	10.8	12.3
Continuous Power Density (kW/kg)	2.8	2.21	1.89	5.4
Reference	[35]	[36]	[37]	[38]

TABLE 3.1: Comparison of four high-performance traction motors

3.4 Axial Flux Switched Reluctance Motors

The AFSRM operates on the same electromagnetic principles as the RFSRM but differs greatly in construction. Salient teeth protrude from the rotor body in the axial direction as seen in Figure 3.8. In the radial machine, the flux path passes through two airgaps however due to the yokeless design shown, the axial machine has four airgaps per pole pair.

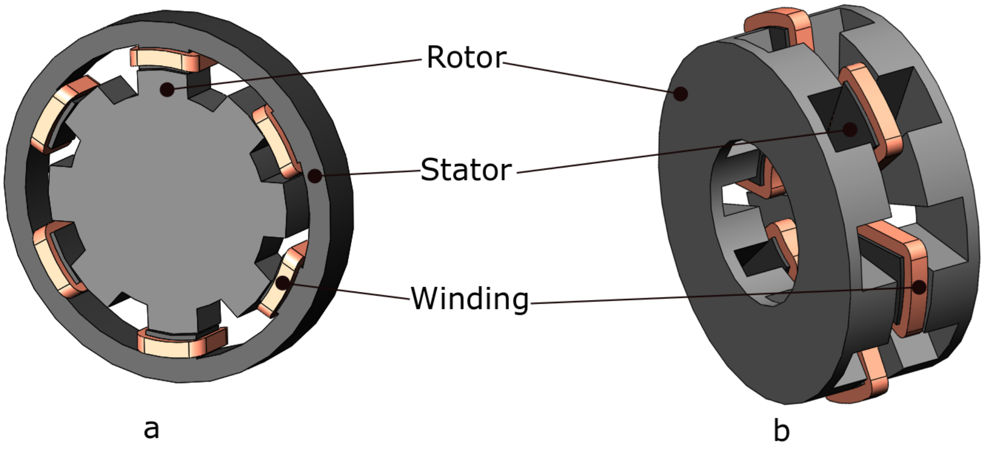

FIGURE 3.8: a: Radial flux SRM. b: Axial flux SRM

3.4.1 Configurations of Axial Flux SRMs

The aligned position in an AFSRM involves some rotor segment completing the flux path from the stator. The rotor design may be classified by the type of flux bridging performed by the rotor. A yoked rotor bridges the flux through the main disc body, as pictured in Figure 3.8b. Yokeless rotor designs may be implemented such that the rotor segment forms either a radial or tangential flux bridge. A basic diagram of tangential and radial bridging ORIS designs can be seen in Figure 3.9. For single-sided and OSIR machines, either the rotor or stator may be segmented, the other must provide the static flux connection between segments. For ORIS machines, both the stator and rotor may be segmented. The C-core SRM (CSRM) is a novel structure first proposed by Mao and Tsao in [39] as a RFSRM and by Labak and Kar as an AFSRM in [40], shown in Figure 3.10. The CSRM incorporates both segmented rotor and stator, however the stator employs a c-shaped iron core to complete the flux loop.

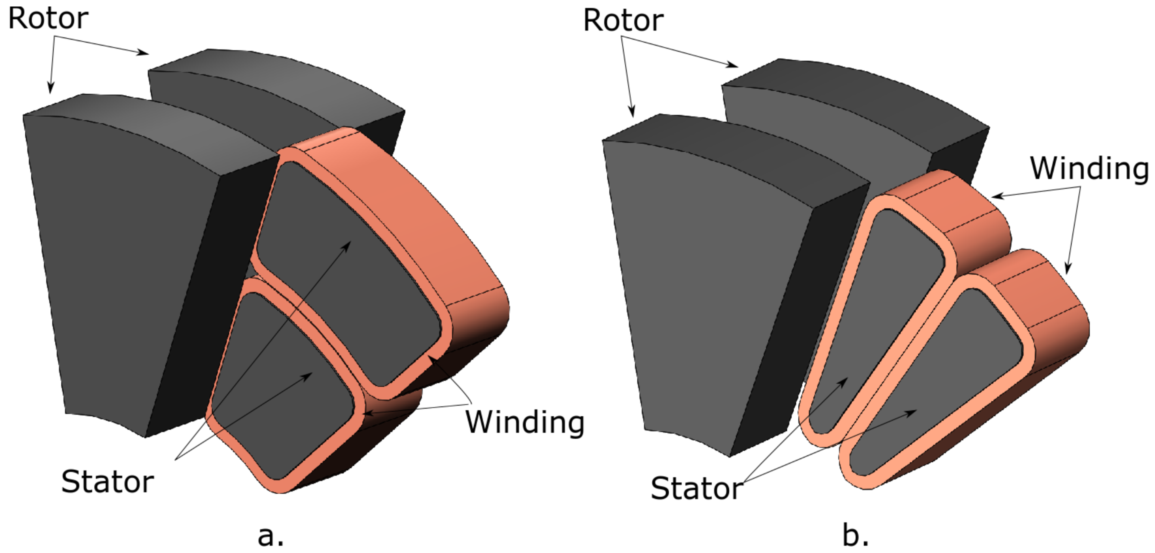

Figure 3.9: a: Radial bridging SRM. b: Tangential bridging SRM

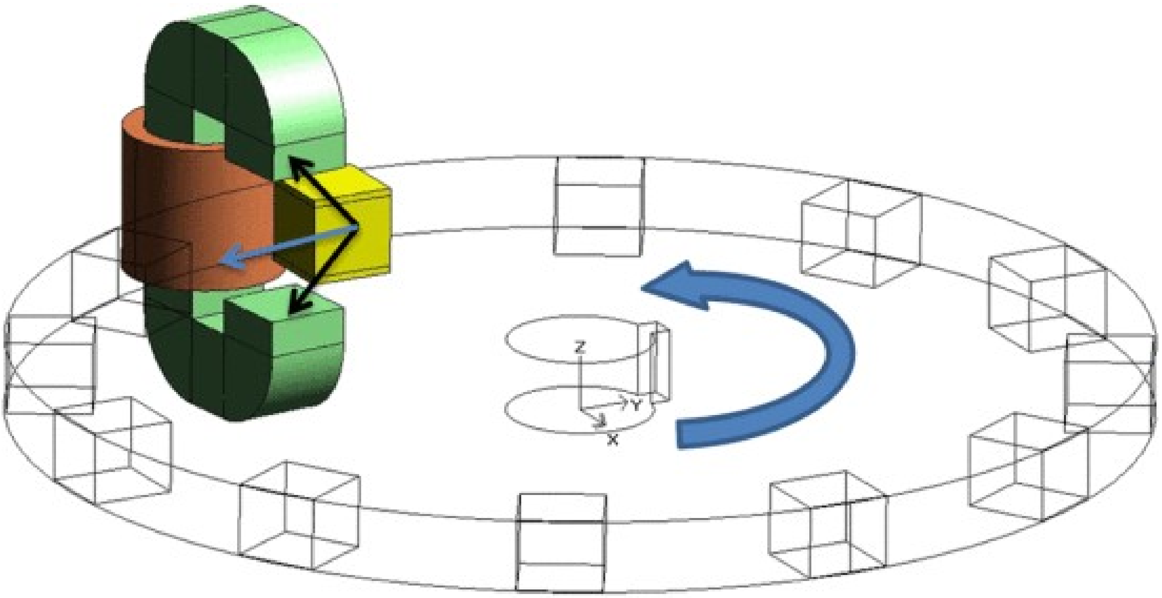

Figure 3.10: C-core AFSRM from [40]

3.4.2 Axial Flux SRMs in Literature

3.4.2.1 Modeling Techniques

A limitation to the design of AFSRMs is the modelling tools available for simulation. The nonlinear effects of pole geometry and material saturation often necessitate extensive FEA to represent the motor behaviour. For RFMs, the machine may be represented as an equivalent 2D cross section and extended to 3D using the stack length, however AFMs do not have an equivalent representative cross section. [41] and [42] explore the reduction of 3D AFSRM geometry into 2D linear motor representation for the reduction in computation time in FEA. [43] divides the 3D geometry into 5 linear motor cross sections for more accurate representation in 2D. Later, the authors present their work in modelling the use of grain-oriented electrical steel (GOES) for stator of this machine in [44]. Using a reduced 3D FEA model, the anisotropic material model was applied to the teeth of the AFSRM. The use of GOES in the stator is suggested to be attributed to an average torque increase of 20%.

Often, FEA is unsuitable for the initial design task for AFSRMs. Modeling techniques that do not require meshing are more suited for the exploratory phase of SRM design, where high-level topology decisions are made. The flux-tube method has been employed extensively for RFSRMs as a method of using pole geometry to populate elements for the magnetic equivalent circuit [45], and was applied in [46] using semi-circular flux line trajectories. In [47], Lambert developed an integral inductance function based on elliptical flux path segments, which more closely resemble magnetic flux line shapes.

3.4.2.2 Optimal Design

The abundance of geometric and electrical parameters that define an AFSRM design present major opportunity for design optimization.

The authors in [48] optimized torque density based on a trade-off between stator length and torque production. Performance dependencies on geometry were evaluated in 3D FEA. The increase in stator axial length is not beneficial for the torque production for AFSRMs in the same way as RFSRMs, however axial length allows for more winding area and higher MMF if current density is thermally limited. While a 1D sweep of axial length may be suitable for 3D FEA, multiple-parameter studies become computationally expensive and require a more efficient simulation tool. To accommodate for a large number of design parameters, statistical methods such as the Taguchi method can be applied, as was demonstrated in [49], where 3D FEA was performed on a limited number of design parameter combinations to obtain an improved machine performance from a baseline.

Several electromagnetic effects that are specific to the construction of AFSRMs are considered in literature. Considering the close proximity of stator poles in the AFSRM, stray flux is of special concern, in the interest of maximizing unaligned reluctance. [50] discusses stator pole shaping to increase the proportion of flux linked through the rotor segment. Torque ripple is another challenge which may be solved with optimization, often at a trade-off with power density. Multple rotors or stators may be skewed at an angle to create a more gradual pole alignment. In [51], the authors found a small skew angle of 2° reduced the torque ripple by 17%. However, a rotor skew will produce unbalanced rotor forces that must be taken up by the bearings.

3.4.2.3 Axial-Flux Specific Design Challenges

One of the most significant design challenges for AFSRM is the core construction. While RFMs use laminated steel sheets to minimize eddy currents, the direction of the flux in AFSRMs can not be contained to planar space. Wound cores may be used for machines with only tangential and axial flux directions, however AFSRMs with radial flux bridging introduce a 3D flux path. SMCs are promising candidates for AFSRMs due to the isotropic magnetic properties. However, SMCs exhibit inferior permeability to electrical steel laminations due to the lower volumetric filling of the material with iron [52]. [42] describes a design using SMCs, which facilitate the manufacturing of the machine despite the tangential flux bridging nature. The need for nonferromagnetic structural materials is greater in AFSRMs vs RFSRMs due to the common segmented nature of the rotor and stator. Stator construction challenges that are unique to AF machines are discussed in [53], in which the authors evaluate a laminated aluminum housing to reduce eddy currents in the structural member for a YASA AFPMSM, seen in Figure 3.11.

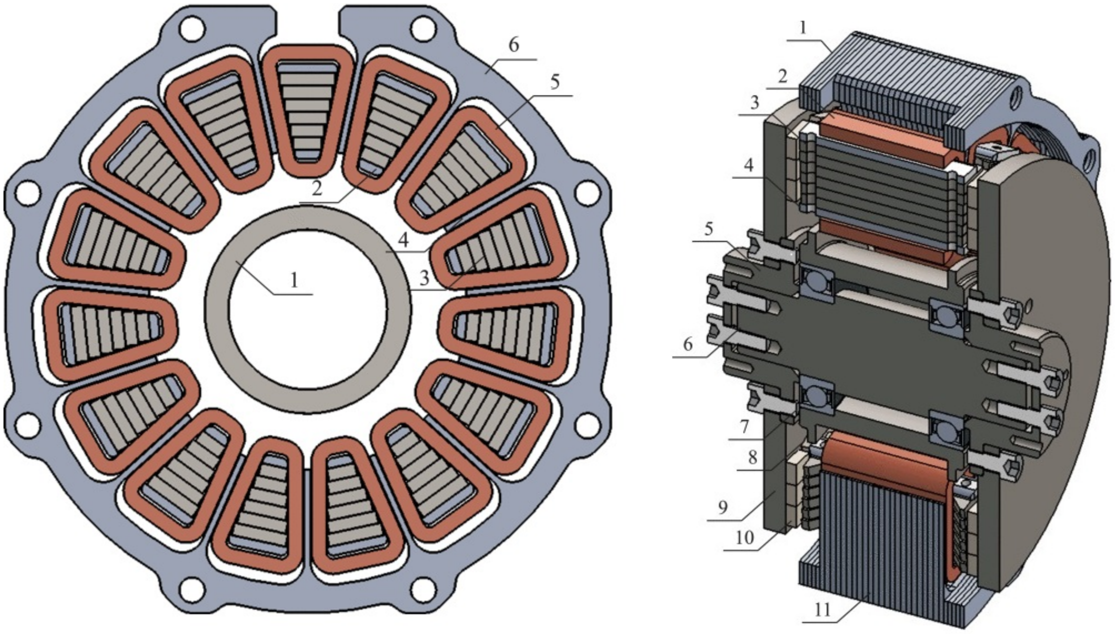

FIGURE 3.11: YASA AFPMSM construction from [53]

Although stator for both the YASA AFPMSM and the YASA AFSRM require a nonmagnetic structural support, the YASA AFSRM does not suffer as severely from frame losses as flux may be directed through the stator pole, and may be "turned off" when the rotor segments pass between stator poles. Structural members of the rotor may also contribute to parasitic losses, as in [49] where a conductive rotor cover plate was found to induce 694 watts of eddy current losses for a 3.7 kW machine. The rotor retention is of special concern for high-speed machines, where higher strength retention materials are necessary, but the potential for parasitic losses is higher. For these reasons, carbon-based composites such as carbon-fiber, glass-fiber and Kevlar are common [54].

3.4.2.4 Successful Prototypes

AFSRMs have been proposed in literature with some successful prototypes. Madhavan investigated a toroidal-wound OSIR machine in [55], using a wound stator and segmented rotors. The stator in this prototype was achieved with machining the winding slots into the pre-wound stator core. Labak and Kar present a C-core AFSRM in their paper [46], with an emphasis on exploiting the C-core geometry to maximize winding effectiveness and heat transfer. The prototype machine achieved a winding fill factor of 40.9%. In [56], Goto presents an OSIR AFSRM with yokeless rotor with tangential flux bridging for a city commuter vehicle with 0.3mm airgap length and 62% winding fill factor. In [41], the authors realize a 80 kW, 20kRPM ORIS AFSRM with segmented rotors. Special consideration is given to the rotor structure, which experiences high centrifugal loads at full speed, and requires a high degree of support for the relatively weak rotor pole segments. In [49], the authors construct a 3.7 kW ORIS AFSRM with segmented stator and single-piece rotors. The rotors are formed by removing material in between poles with an electric discharge machining (EDM) process. The airgap achieved was 0.3mm. Four example machine 3D models can be seen in Figures 3.12

3.4.3 Benefits of AF Structure for SRMs

The AFSRM has the benefit of more compact design as the torque production does not depend on axial length. The pole segments may be produced individually, which introduces the potential for machine winding the conductor directly on the pole segment. The winding process of an AFSRM may be simplified by using a modular stator, which is not achievable for RFSRMs. Thus, high copper fill factors may be achieved. A shorter flux path is credited for lower iron losses and higher power density compared to RFSRMs [57]. For high-speed SRMs, some radial deformation of the rotor is expected due to hoop stress, which in a RFSRM may cause rotor collision, however expansion of AFSRM rotors will not interfere with the airgap. Additionally, high speed motors will often use retaining sleeves around the rotor surface to

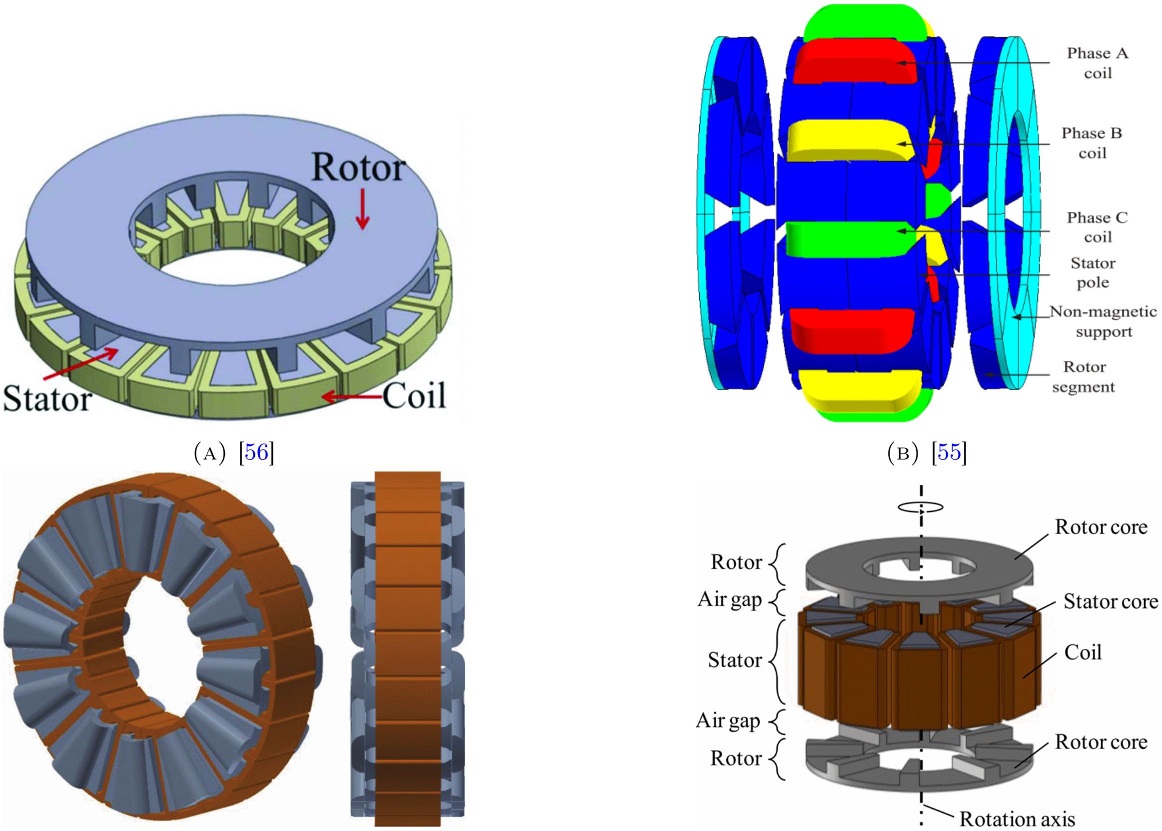

(A) [56]

(B) [55]

(C) [41]

(D) [49]

FIGURE 3.12: Geometry of four AFSRMs from published works

prevent disassembly at speed, which occupies space in the RFSRM airgap, requiring tighter tolerances. However a retaining sleeve in the AFSRM occupies space outside of the magnetic path of the machine, simplifying the sleeve design.

3.4.4 Challenges of AF Structure for SRMs

Due to the 3D flux path, AFSRMs will require isotropic materials for flux-carrying components, particularly for yokeless rotor machines where it is not possible to prevent flux in the radial direction. The mechanical design of the backiron becomes difficult, given the relatively poor mechanical properties of SMCs or single-pole lamination stacks. Unlike RFSRMs, the machine geometry cannot be represented by a 2D cross-section, resulting in exponentially higher computational power required for simulations. The high radial forces in RFSRMs exist as axial forces in AFSRMs, however the disk-shape is not as suited to resist these forces as the cylindrical RFSRM components, leading to high vibrations and risk of collision. Additionally, the bearings must absorb these forces through the balls, whereas radial forces in RFSRMs are balanced through the rotor and stator structures.

Chapter 4

AFSRM Design for Light Electric Vehicles

4.1 Conceptual Design

The AFSRM design in this chapter is built upon the conceptual design by Lin et al. [1]. The motor is a 4-phase, dual external rotor, 8/6 AFSRM with radial flux bridging. Flux is linked from the outer stator segment to the rotor, returning through the inner stator and the opposite rotor for a total of 4 air gap interfaces. A summary of the motor dimensions is given in Table 4.1 and the motor topology is shown in Figure 4.1.

Previous analysis indicates that a machine of this topology and dimensions is capable of producing a continuous 8 N.m at up to 6000 RPM, which is promising for the LEV application. Torque density may be improved by reducing the airgap length and maximizing the usage of winding space.

Component	Parameter	Value
Stator	Pole Numbers	8
	Outer tooth outer radius	96 mm
	Outer tooth inner radius	76 mm
	Inner tooth outer radius	72 mm
	Inner tooth inner radius	38.9 mm
	Axial length	40mm
	Pole pitch	45°
	Pole arc	22.5°
Rotor	Pole number	6
	Outer radius	96 mm
	Inner radius	38.9 mm
	Axial depth	22.6 mm
	Pole pitch	60°
	Pole arc	22.5°
Winding	Axial length	32 mm
	Slot height	4mm
	Number of turns per pole	16
	AWG	11
Airgap	Length per side	0.5 mm

TABLE 4.1: Baseline AFSRM dimensions

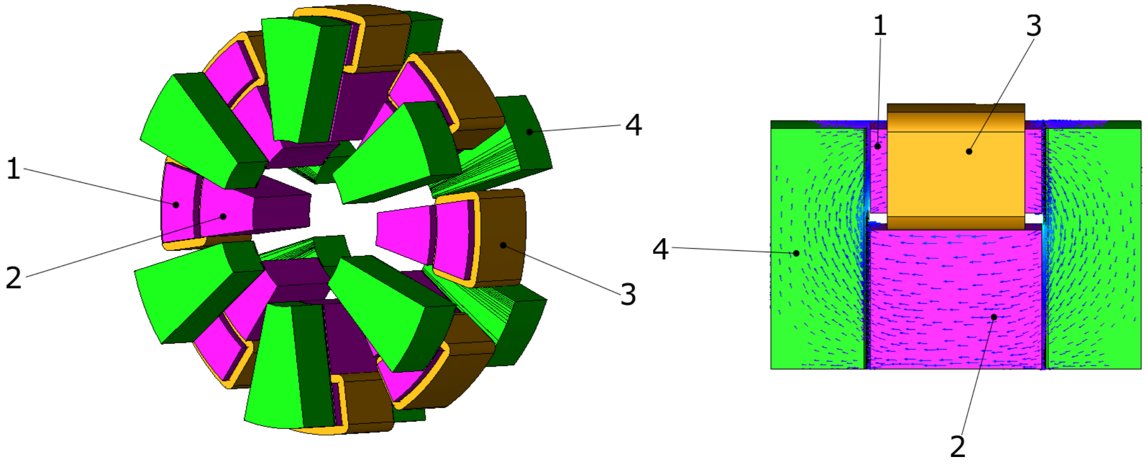

(A) Full motor (B) Flux lines for single pole at aligned position

FIGURE 4.1: Baseline motor design. (1) - Outer stator pole. (2) - Inner stator pole. (3) - Stator winding. (4)- Rotor pole

4.2 Performance Analysis for Design

The AFSRM geometry is analyzed in JMAG to extract electromagnetic performance data such as torque, flux linkage, flux density and axial forces. Due to the 3-D nature of the flux path, 3D FEA is unavoidable, and the model must be reduced to the most simplified representation. [1] showed that the machine topology can be reduced to a quarter-pole, with a natural boundary constraint applied along the stator mid-plane. The natural boundary allows the solver to consider a zero-reluctance path that originates and returns to the defined boundary plane. Due to this condition, the model must be defined with half the stator MMF to accommodate the half of the symmetry plane that is considered to be zero reluctance. The model reduction can be explained with a magnetic circuit, where $\mathscr{R}_{1/2}$ represents half the reluctance seen by a single stator winding during the conduction period.

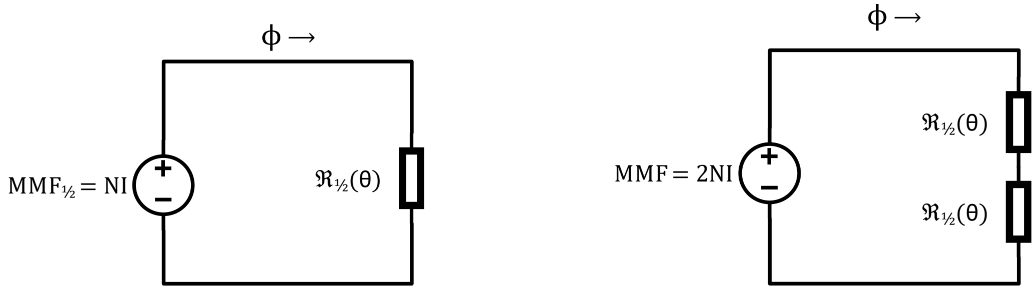

(A) Half pole equivalent circut

(B) Full pole equivalent circuit

FIGURE 4.2: Equivalent circuit for explaining model reduction using symmetry

The flux linkage, $\lambda = \phi N$ must be converted to the full-phase quantity for the dynamic model. If a half quantity turn count is used for N, the flux linkage for the half-pole and full-pole models can be expressed as:

$$\lambda_{1/2} = \frac{N^2 I}{\mathscr{R}_{1/2}} \tag{4.1}$$

$$\lambda_{\text{Full}} = \frac{(2N)^2 I}{2\mathscr{R}_{1/2}} = \frac{2N^2 I}{\mathscr{R}_{1/2}} \tag{4.2}$$

Therefore, the both the torque and flux linkage can be scaled by two to obtain full pole characteristics by using the natural boundary and a halved turn count. Additionally, data can be extracted for the half cycle only, due to symmetry it is assumed that the characteristics from $-\theta_{\text{unalgined}} < \theta < \theta_{\text{aligned}}$ are identical to $\theta_{\text{aligned}} < \theta < \theta_{\text{unaligned}}$, with the exception that the torque in the latter region will be negative. Thus, both the model geometry and angle sweep can be reduced by two by applying symmetry.

The AFSRM analysis targets the prediction of three key performance metrics:

- Torque and Power
- Efficiency
- Torque Quality

The calculation of efficiency relies on the accurate estimation of the machine losses. Copper loss can be accurately predicted with phase currents and resistances calculated from coil dimensions, however traditional iron loss predictions for 3D electromagnetic applications rely on element-wise loss calculations in FEA. While FEA provides an accurate estimation, it is impractical to include in performance analysis workflow, particularly during optimization, where numerous conditions must be evaluated. Thus, a numerical approximation is introduced later in the next chapter to efficiently include iron losses in the analysis workflow. For the purposes of checking the design, certain operating points may be simulated in FEA to predict the iron losses where necessary.

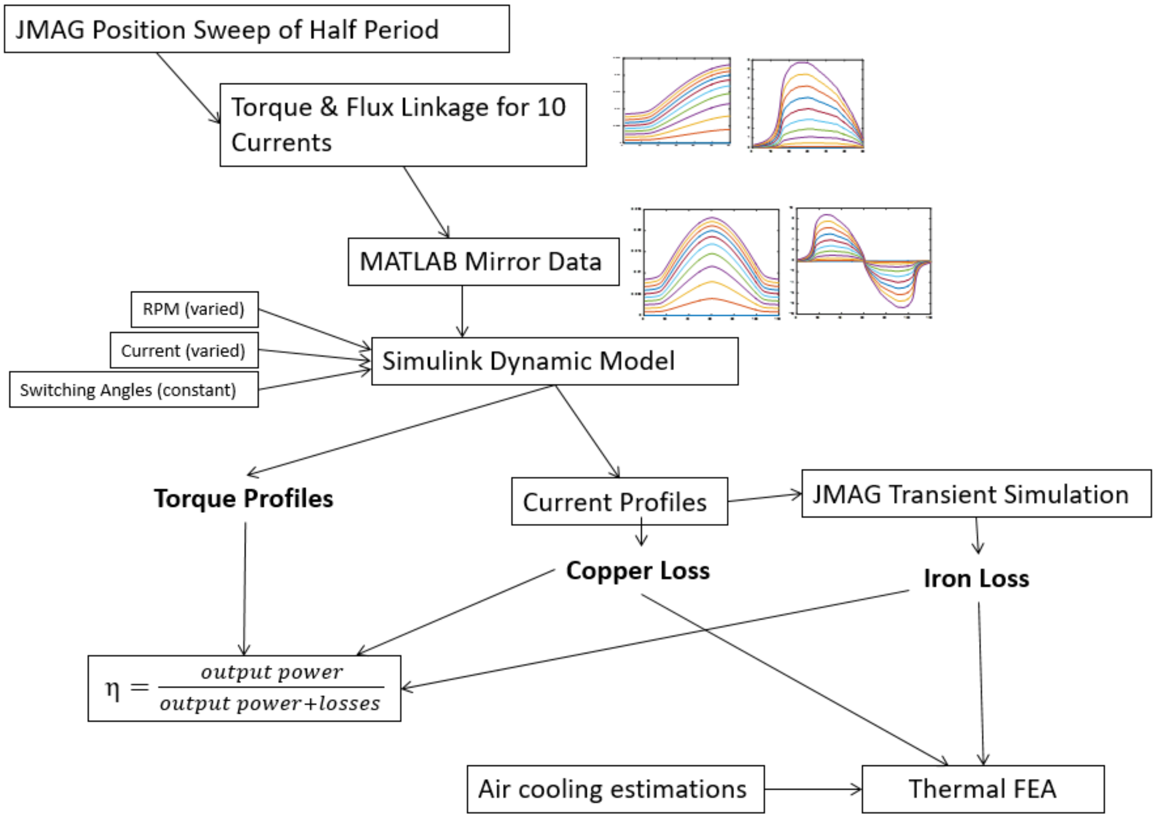

Figure 4.3: Workflow for AFSRM analysis at the design stage

4.3 Winding Material Selection

A winding slot of 5mm x 40 mm was defined for the AFSRM, with a set turn count of 16. The longer slot dimension represents the length from airgap-to-airgap (AG to AG) and the shorter dimension represents the spacing between stator tooth and flux return tooth. A mainwall insulation is required at each interface between backiron and winding, reducing the available with to 4.5 mm. Due to the high currents necessary to drive the machine, copper loss dominates in key operational points. Therefore, effort should be made to reduce the phase resistance as low as possible and maximize the heat removal capability of the windings. While a full-width winding is ideal, it leaves the stator tooth floating, and requires the winding to be a structural and dimensional component of the machine. The narrow slot size limits the types of wire gauges that could be applied. With an aspect ratio of 8, the slot

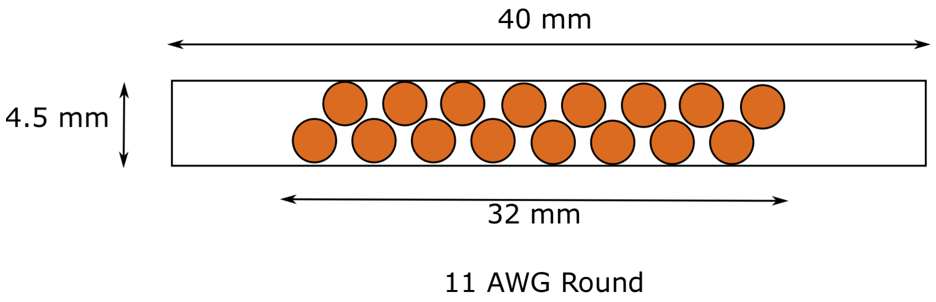

(A) 11 AWG round conductor

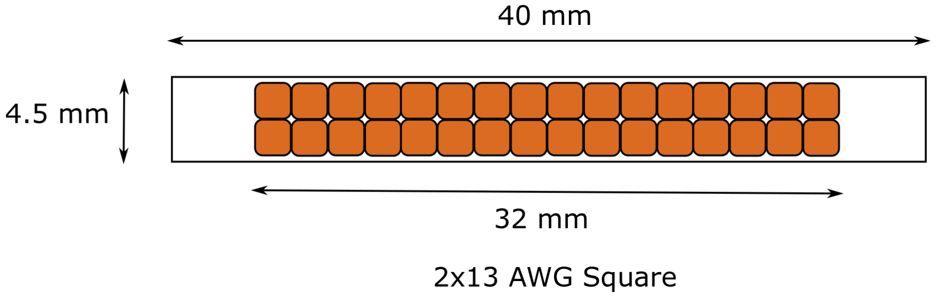

(B) 2 x 13 AWG square conductor

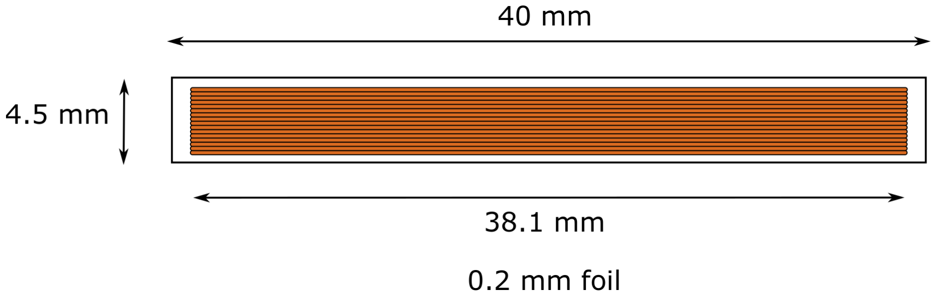

(C) 38.1 x 0.2 mm foil conductor

FIGURE 4.4: Possible conductor patterns for given footprint

cannot accommodate a 4.5 mm diameter round wire gauge stacked in single layer, however 11 AWG may be wound in a dual layer as seen in Figure 4.4a. A full slot height square wire is also not possible, however an arrangement of two 13 AWG square conductors will fill the slot height well, with all 16 turns occupying a 32 mm width. This arrangement is shown in Figure 4.4b. Finally, a copper foil could be wound around the tooth, with nearly full-width turns stacked to fill the 5mm slot height. A 0.05 mm Nomex insulation paper divides the foil layers. This configuration can be seen in Figure 4.4c.

Windings may be compared in terms of overall fill factor, which is defined as the copper area as a percentage of Airgap-to-airgap (AG/AG) area. Alternatively, the fill factor may be calculated using the footprint of the winding. DC winding resistance can be calculated using a constant turn length and the winding cross sectional area:

$$R_{\text{phase}} = 2R_{\text{Winding}} = \frac{2N_{\text{turns}}\rho_{\text{Cu}}l_{\text{turn}}}{A_{\text{C}}} \tag{4.3}$$

Table 4.2 compares the fill factors and resistances of each winding.

Conductor	1.5" Foil	11AWG Round	2x13AWG Square
Conductor Area (mm^2)	7.73	4.17	6.4
Fill Factor (AG/AG)	0.6874	0.3709	0.5689
Fill Factor (Footprint)	0.7218	0.4635	0.7111
Phase Resistance ($m\Omega$)	8.65	16.1	10.5

TABLE 4.2: Winding fill factors and resistances for foil, round and square conductors

The ability for a conductor to carry AC current is determined by the geometry of the conductor cross section, where the skin effect limits utilization of the conductor cross section as frequency increases. Thus, a conductors ability to carry current depends on its cross-sectional perimeter, not just the conductor area at high frequencies. For rectangular geometry, the ratio of perimeter to area increases as the aspect ratio increases. For square and circular geometry, the ratio of perimeter to area diminishes as the size increases. Therefore, a large aspect ratio conductor such as foil is a good candidate for avoiding skin effect losses. The skin depth δ, which describes the depth from conductor surface where current density falls to 37% of the surface current density, is given as:

$$\delta = \sqrt{\frac{2\rho}{\omega\mu}} \tag{4.4}$$

where μ, ρ are the permeability and resistivity of the conductor and ω is the angular frequency of the current. For an SRM with N_{R} rotor poles operating at N RPM, the angular frequency of the current is:

$$\omega = \frac{2\pi N * N_{\text{R}}}{60} \tag{4.5}$$

which is $5026 rad/s$, or $800 Hz$ for a 8/6 machine operating at 8000 RPM. The AC resistance is given by the resistance factor F_{R}, which represents the increase in resistance at a certain AC frequency compared to DC, given in equation 3.12. The argument A depends on the conductor geometry. For round conductor:

$$A = \frac{\pi}{4}\frac{d}{\delta}\sqrt{\eta_{\mathrm{w}}} \quad , \quad \eta_{\mathrm{w}} = \frac{d}{p} \tag{4.6}$$

where d is the wire diameter, p is the wire spacing and δ is the skin depth. Similarly, for square wire:

$$A = \frac{w}{\delta}\sqrt{\eta_{\mathrm{w}}} \quad , \quad \eta_{\mathrm{w}} = \frac{w}{p} \tag{4.7}$$

where w is the wire width. For foil, the argument A is simply:

$$A = \frac{h}{\delta} \tag{4.8}$$

where h is the foil thickness and the porosity factor η is 1. Figure 4.5 shows a sweep of frequencies from DC up to 10 kHz that was performed on the conductor geometries presented in Figure 4.4.

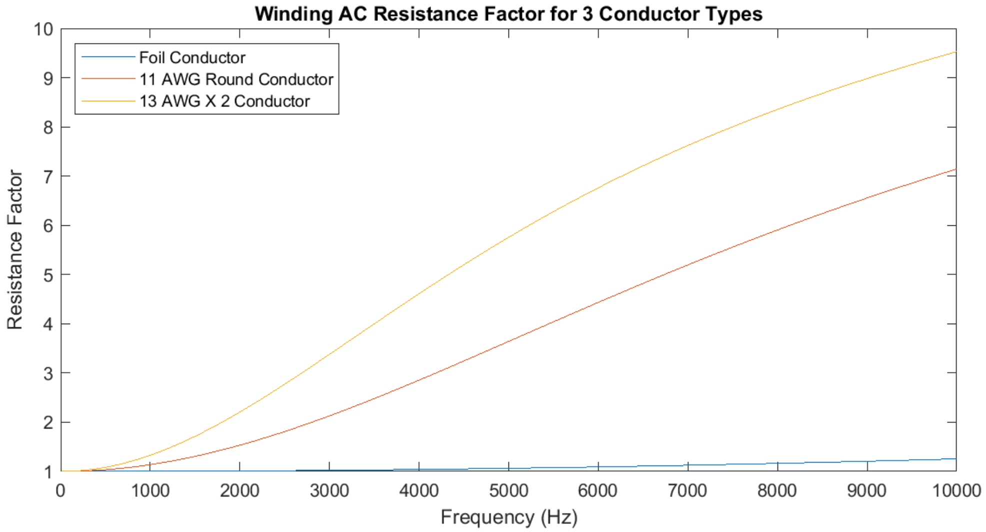

FIGURE 4.5: AC resistance factor for round, square and foil conductors up to 10 kHz

Along with fill factor and AC resistance, the winding types can be evaluated qualitatively in terms of winding manufacturability. The foil winding achieves the best utilization of space, however leaves no room for structural support of the stator tooth. The round and square configurations leave approximately 4mm on each side of the stator to allow the stator pole to interface with a retention component, outlined in the following section. The square conductor winding requires highly accurate control of the winding process to ensure the orientation of each turn and its proximity to the next, whereas the foil conductor winding process is self-orienting and only requires the alignment of each layer to the next.

The thermal performance of each winding depends on the quality of the conductive heat path to the surroundings. The winding has thermal interfaces with inner and outer stator poles, both airgaps and the structural stator ring. Optimal thermal performance is achieved when each layer of conductor in the coil has the maximum contact area with the next. Thus, the round conductor would have poor performance due to the tangential contact interfaces between the conductors. The square conductor thermal performance would rely on the orientation of the conductors against each other. It is assumed that a square or round conductor winding would be encapsulated in a thermoset polymer, both for structural rigidity and thermal conductivity.

Based on the electrical, manufacturing and thermal characteristics, a foil conductor is selected for the AFSRM. In the following section, the stator geometry will be investigated for improvements in electromagnetic performance.

4.4 Stator Design

The AFSRM stator core consists of two segments: the outer pole, contained within the winding and the inner pole, acting as a flux-return path. Their design depends on their electromagnetic performance and manufacturing feasibility. The component manufacturability will be driven by the selection between laminated and isotropic materials. An integral average flux density can be extracted from FEA data in cylindrical coordinates to examine the flux direction behaviour, in order to evaluate the feasibility of using laminations. The cylindrical coordinate system for the AFSRM is shown in Figure 4.6. Figure 4.7 shows that the radial flux is limited, allowing for a laminated core in the $[\theta, z]$ plane.

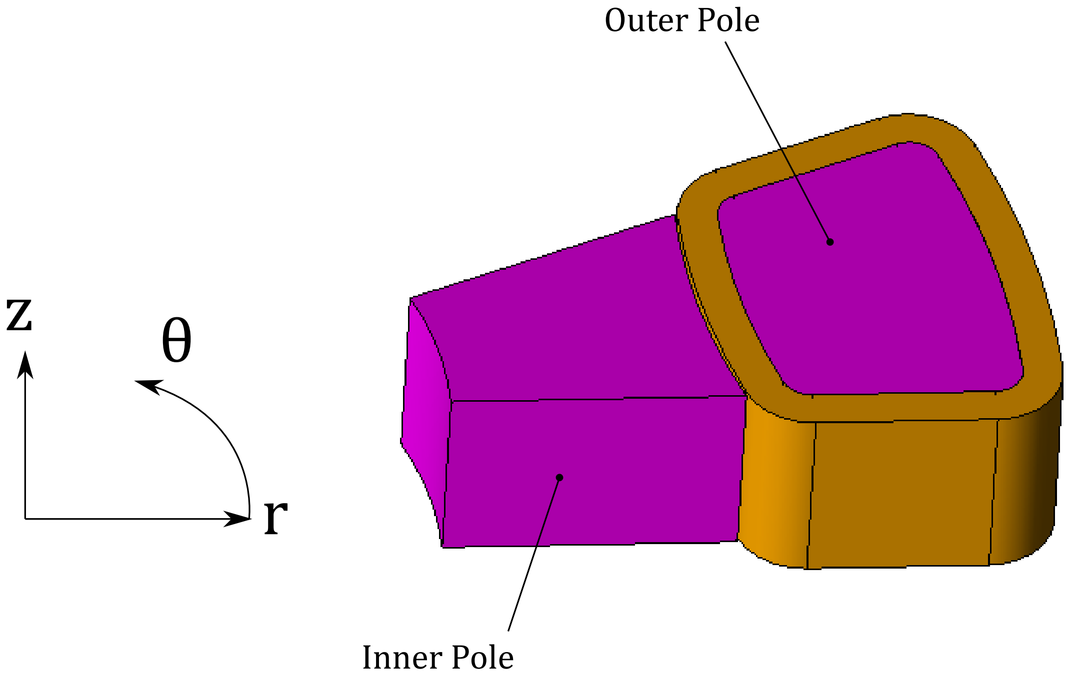

FIGURE 4.6: Cylindrical coordinate system for examining flux directions in the AFSRM

While laminated steel can achieve a higher saturation flux density than SMC, the structural challenges for laminations would introduce a more complex design due to the wedge shape of the pole. Given the increasing width as the laminations are stacked in the radial direction, the wedge shape may only be achieved by producing each lamination uniquely. Additionally the laminations should curve to follow the path of the rotor pole, which is more achievable with a wound-core for a non-segmented stator. Thus, SMC is a candidate of interest for the stator due to its versatility to make up complex shapes. Höganäs AB (Höganäs, Sweden) offers a wide range of SMC products for electric machine applications. One of their highest performing powders is Somaloy 700HR 5P, which exhibits lower core

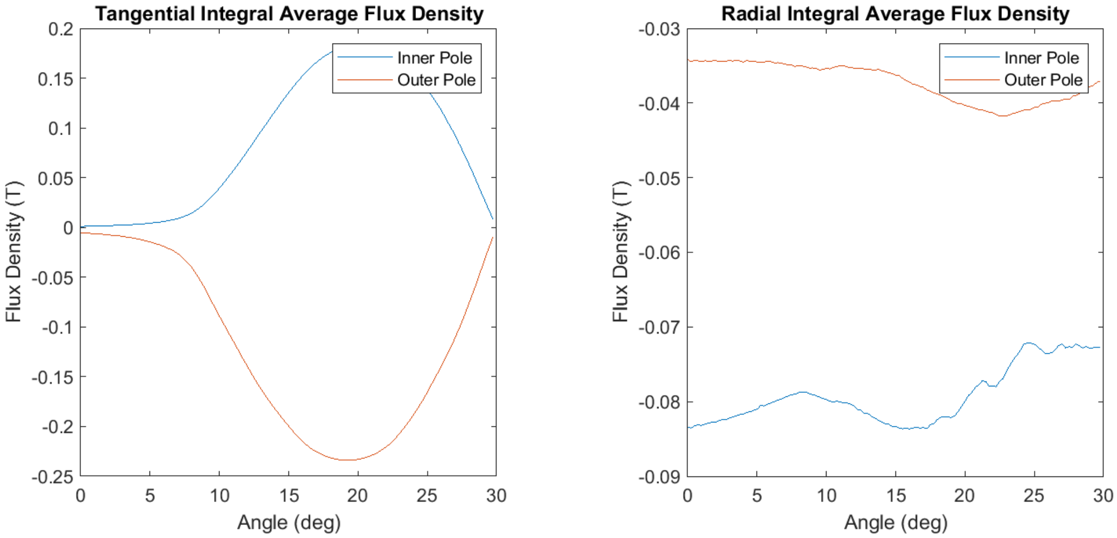

(A) Tangential flux density

(B) Radial flux density

FIGURE 4.7: Integral average flux density plots of both stator segments under 150 A constant current excitation for $0° < \theta < 30°$

losses than others in the Somaloy product line, and the highest relative permeability, at the cost of weaker structural properties. The magnetic properties requires for FEA are made available, including iron loss data. At this stage, the machine design will consider Somaloy 700HR 5P for all analysis.

The base geometry is defined by concentric arc segments that allow uniform rate of change of overlap area with respect to rotation angle. While this design is shown to exhibit a close to sinusoidal torque profile, the stator winding becomes difficult due to the partially concave edge. A flat and convex edge are studied, along with shifting the inner convex edge towards the center of the stator to balance the cross sectional area between inner and outer stator segments. The six profiles studied are summarized in 4.8 and the resulting torque profiles from FEA are shown in Figure 4.9. Geometries D, E and F are created by shifting the convex edge marked in cyan on Geometry C.

The geometry should also be compared in terms of winding resistance due to the change in pole perimeter. The average turn length can be calculated by the average between interior and exterior coil perimeter measured from the CAD model. It is also interesting to compare

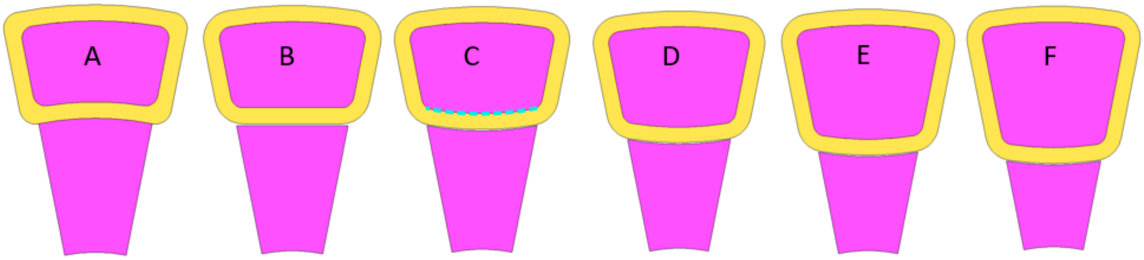

FIGURE 4.8: Stator geometry cases: Cases D, E and F are derived by shifting down the marked edge on Case C

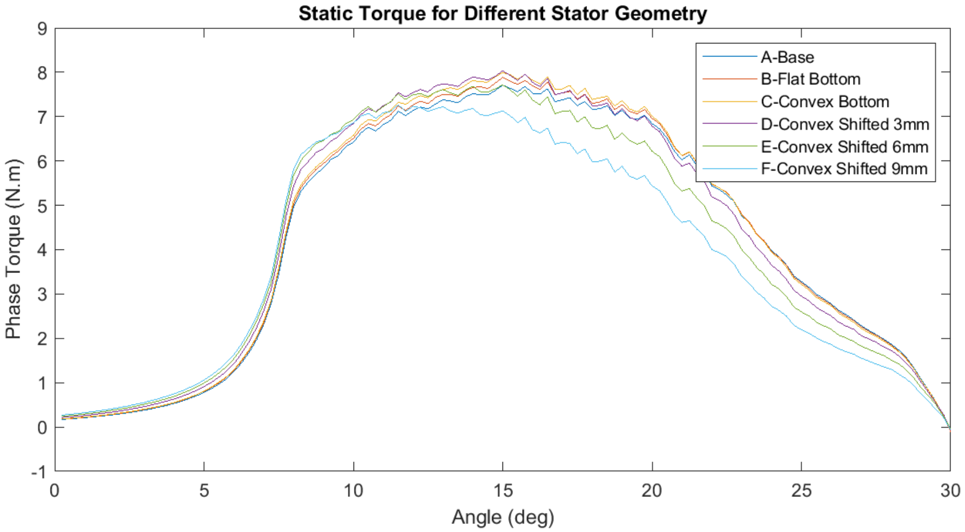

FIGURE 4.9: Static torque for 6 stator geometries

the geometries in terms of the relative area of the inner and outer pole. Neglecting leakage, the equal flux passes through both inner and outer poles, therefore equal areas would allow both segments to saturate together. This ratio is listed as $\frac{A_{\text{out}}}{A_{\text{in}}}$ in Table 4.3 which also compares the winding resistances of the six geometry cases that are studied. The winding resistance is based on the foil conductor from section 3.3 at 25°C.

Label	Name	Average Turn Length (cm)	Pole Area Ratio $\frac{A_{\text{out}}}{A_{\text{in}}}$	Winding Resistance ($m\Omega$)
A	Base	11.5	0.92	4.4
B	Flat Bottom	11.4	1.02	4.35
C	Convex Bottom	11.5	1.11	4.4
D	Convex shifted 3mm	12.15	1.42	4.64
E	Convex shifted 6mm	12.7	1.81	4.85
F	Convex shifted 9mm	13.2	2.33	5.04

TABLE 4.3: Stator geometry comparison

Based on the torque profiles, cases E and F exhibit poor performance as the overlapped angle increases, likely due to saturation of the inner pole. Overall, case D has the highest average torque performance while remaining an easily wound coil. Therefore, the stator pole shape is set as case D.

4.4.1 Stator Pole Retention

The basic stator structure can be seen in Figure 4.10. An outer ring (1) encloses the structure, comprised of stator "modules" (3) arranged around a central hub (2) that holds the bearings.

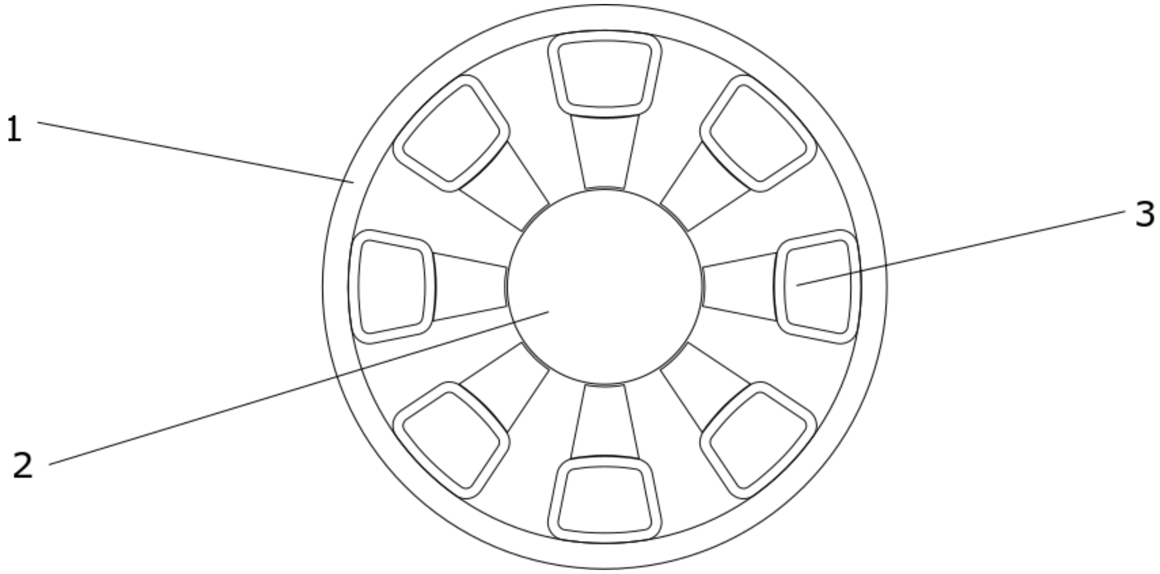

Figure 4.10: Basic structure of the AFSRM stator

In this configuration, the stator modules are constrained in the radial direction, however are susceptible to axial movement. It is proposed that a global encapsulation with a thermoset polymer is applied to the cavity bounded by the outer ring. In this case, adhesion properties from the polymer encapsulation to the various components are critical. Structural elements that provide interfaces between the stator poles and greater stator structure are useful in improving the robustness of the stator construction. Additionally, features may be added to prevent the formation of a sliding contact between the encapsulation and the stator ring, introducing perpendicular surfaces that restrict displacement and decreasing the criticality of shear strength of the adhesive bond. The inner stator segment may be slotted to interface with a structural disk, known as the spine, seen in Figure 4.11. FEA indicates a 2mm x 2mm slot should have negligible effect on the static torque characteristics of the motor. The spine (1) is bolted to a ridge on the central hub (2). Grooves on the inner stator segment (3) constrain the segment axially. The outer stator segment (4) and coil (5) are still left unsupported.

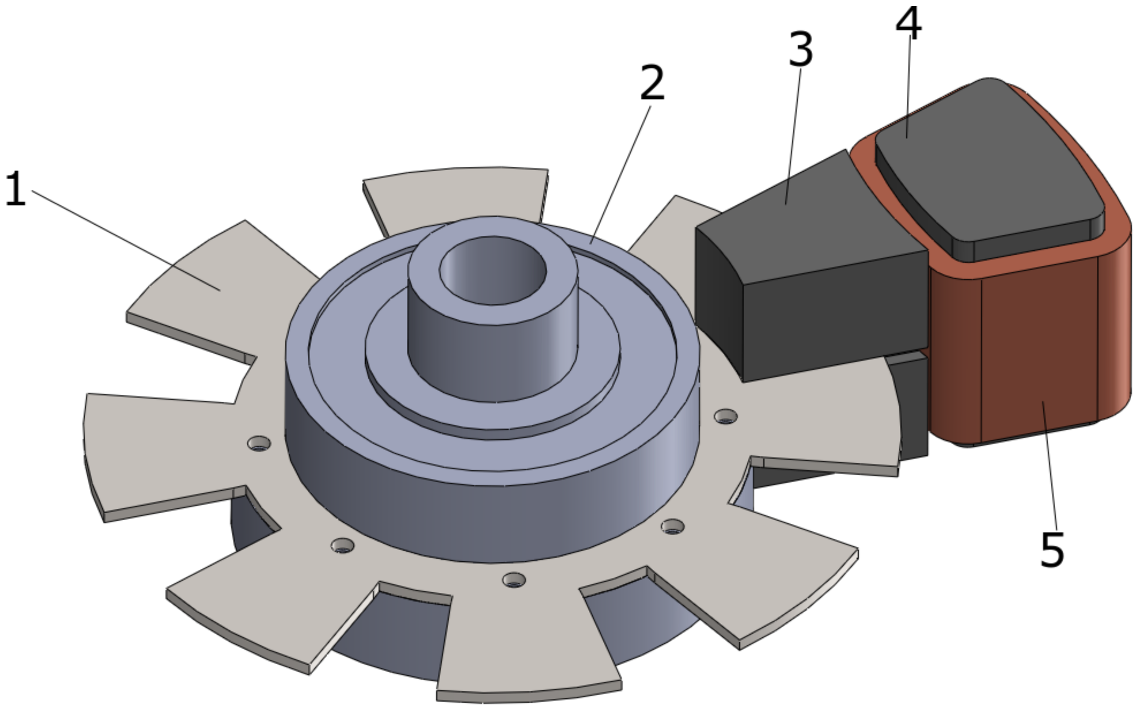

FIGURE 4.11: Inner segment retention with spine and groove

Constraining the outer segment is more challenging due to the winding. A spacer could be cut from stainless steel to lock the outer segment to the inner segment, without compromising the winding. A single spacer design is pictured in Figure 4.12, requiring an additional groove in the inner segment and two notches in the outer segment. Alternatively, dual spacers could be used by notching the edges of both inner and outer segments. This concept is illustrated in 4.13. The static torque sweep is repeated for the stator models with notches to observe the effect of the iron material removal. The resulting torque profiles are plotted in Figure 4.14.

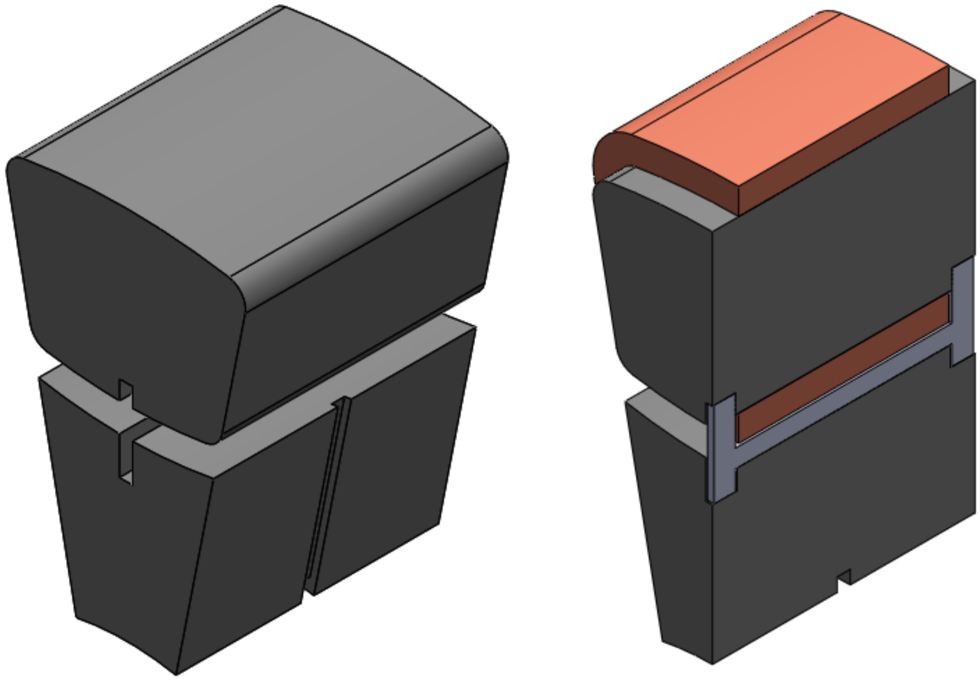

FIGURE 4.12: Stator retention design with single spacer

The dual notch model suffers during the smaller overlap angles, due to the flux concentration on the edges. The central notch model had a less significant reduction and only suffers during the mid-overlap. Not simulated is the eddy current losses in the spacer, which would be significant in the dual spacer model due to the high concentration of time-varying tangential flux in the edges. A non-conductive material could be used to mitigate losses, however the strength and temperature requirements prohibit the use of most common insulator materials. An alternative structural measure is the installation of endplates that could be secured to the outer ring and inner hub by fasteners, and adhered to the stator poles with epoxy adhesive. The endplate structure design is pictured in Figure 4.15.

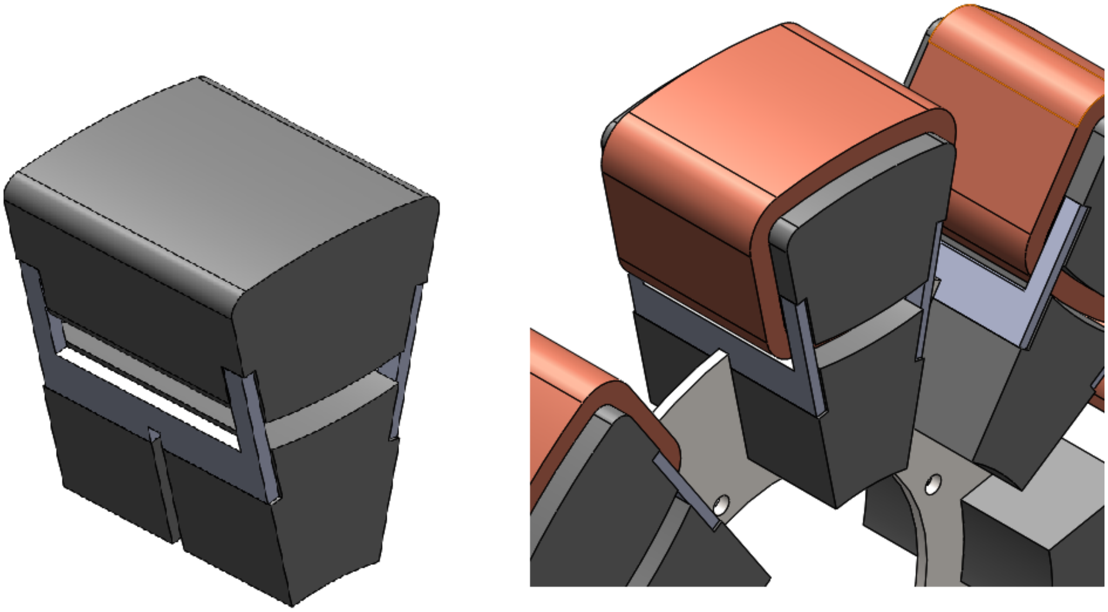

Figure 4.13: Stator retention design with dual spacer

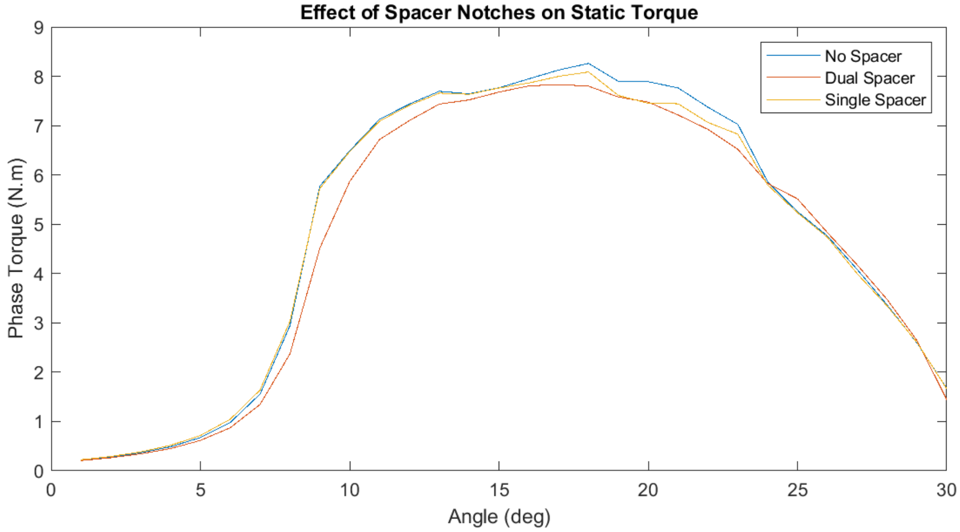

Figure 4.14: Effect on torque of iron removal for spacer interface

This design avoids removal of active stator material, allowing for the static torque characteristics to be unaffected. While the endplates provide secure retention for both the winding and the pole, they should be as narrow as possible to maximize winding space. Should the material be conductive, such as stainless steel, eddy currents must be considered

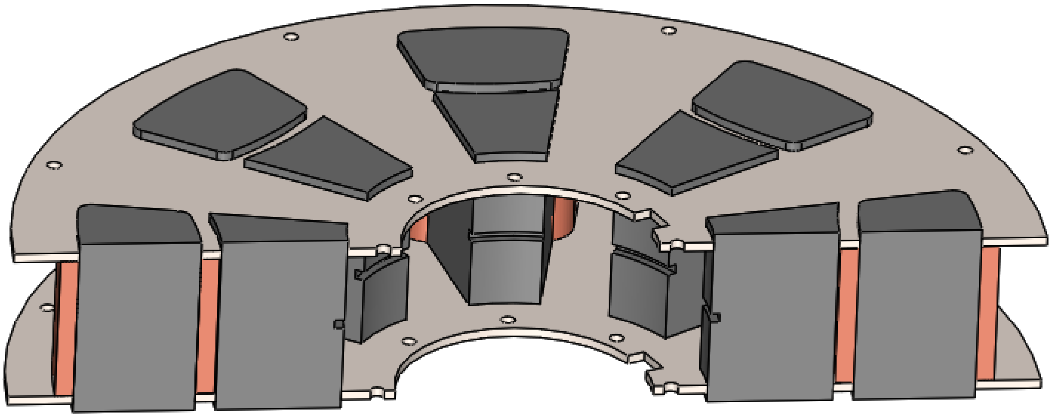

Figure 4.15: Stator retention design using endplates

in the area adjacent to the poles. A JMAG static simulation was set up using 16 gauge stainless steel and maximum current conditions to observe the distribution of flux density in the sheet. Figure 4.16 shows a contour plot of flux density at a critical rotor position. The leakage flux between stator segments occupies some of the stainless steel material between segments. In addition to this, the region just outside the leading edge of the stator poles is subject to unwanted flux density. When the machine is operating at elevated speed, it is likely to induce losses in the plate.

A transient simulation was carried out for $I_{\text{targ}} = 150A$ and $N = 5000RPM$. Figure 4.17 shows the calculated plate eddy current loss in JMAG. The loss profile indicates a current loop being formed around the perimeter of the stator poles, spiking when a transient in stator flux occurs at the beginning and end of the conduction cycle. The elimination of the connection "bridge" between the inner and outer stator segments would open the current loop and reduce induced losses. The loss profile of the endplate with the bridge removed is shown in figure 4.18. Due to cancellation of the in-flowing and out-flowing flux that the cut endplate surrounds, lower losses are resulting. The difference in induced current paths can be seen in Figure 4.19.

Despite the modified plate geometry, the parasitic losses are still unacceptable. An

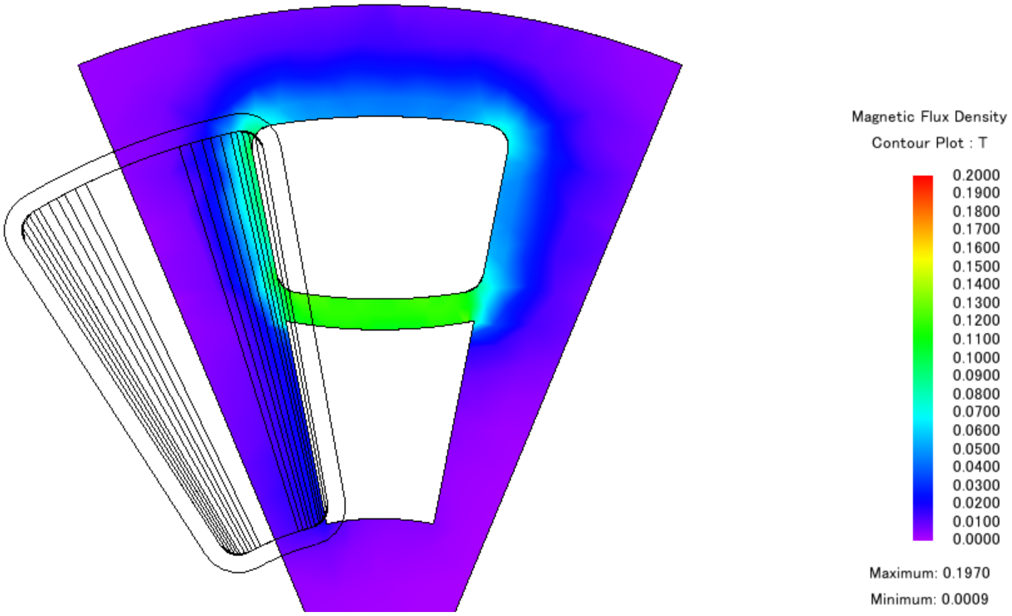

FIGURE 4.16: Flux density contour plot at $I = 150A$ and $\theta = 8.5°$

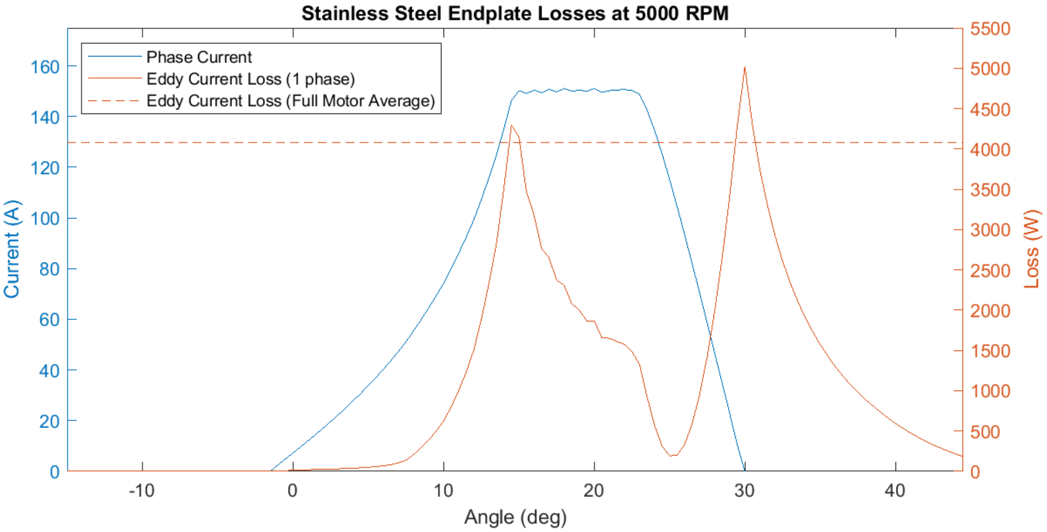

FIGURE 4.17: FEA simulation for eddy current losses in stainless plate

alternative to both the retention spacers and endplates is a structural winding with bonded layers, allowing retentive forces to be transmitted through the winding onto the SMC pole. This can be achieved using an epoxy impregnated insulation paper. Such an insulator is commonly available for the power transformer industry where adhesion is desired and is known as B-staged material. Single-component epoxy is partially cured with a low reactivity

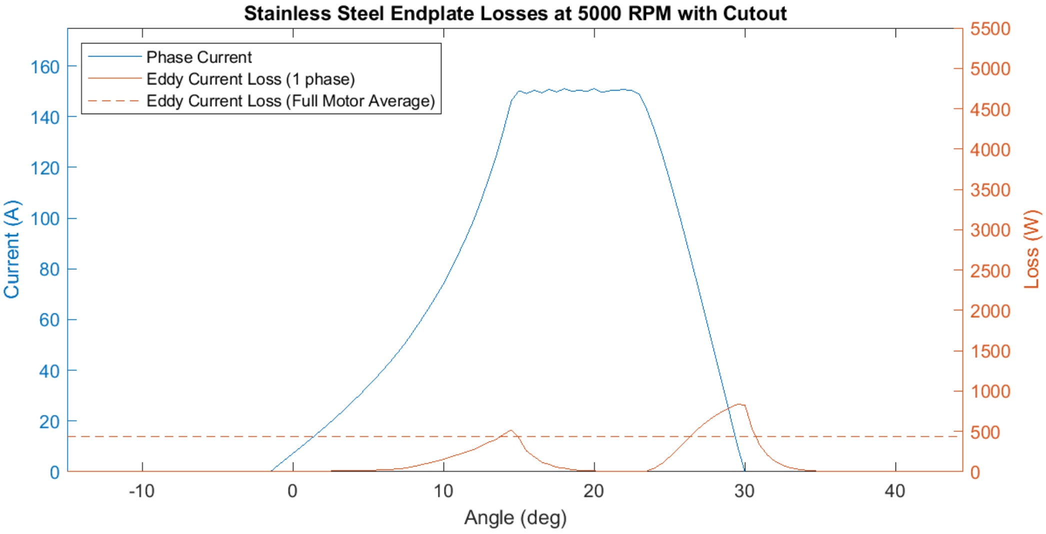

FIGURE 4.18: FEA simulation for eddy current losses in stainless plate with bridge removed

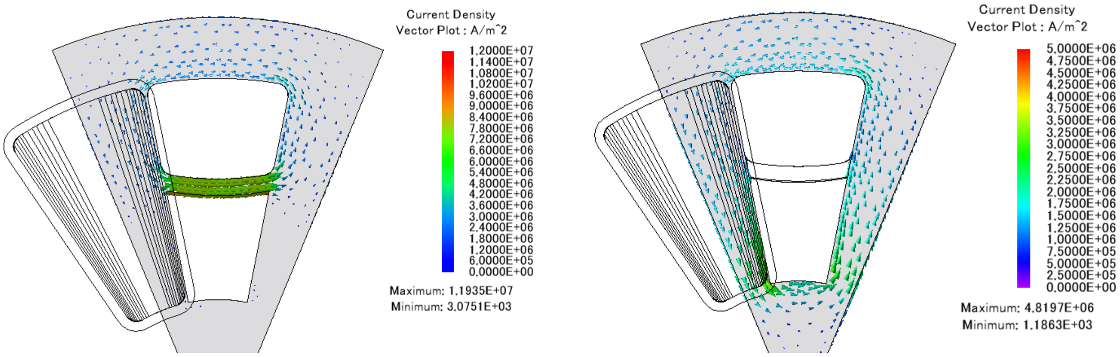

(A) Unmodified endplate

(B) Endplate with bridge cut

FIGURE 4.19: Induced current in stainless steel endplate for $I_{\text{targ}} = 150A$ and $N = 5000RPM$

curing agent to achieve a dry but uncured impregnation of the insulation paper. A permanent cure is achieved with heat and pressure. The selected insulation product is from Flexcon Inc, whose properties are listed in Table 4.4.

Due to the lack of structural elements retaining the outer pole, the segment is left floating and only supported by the surrounding winding. This design allows for a near-full width winding, achieving minimum possible copper losses, however the axial strength and dimensional accuracy now rely on the winding, a component that does not typically serve these functions. It is proposed that a structurally robust and dimensionally accurate foil

Property	Value
Nominal thickness	0.002-0.003"
Thermal class	Class R 220°C
Dielectric strength	1290 V
Cure pressure	50-100 psi
Cure temperature	350°F
Cure time	45 minutes

Table 4.4: B-staged Nomex insulation datasheet

winding can be achieved by layering the B-staged Nomex insulation in between foil layers, then curing with a clamped mold under heat. The shear forces that the winding layers must provide are a function of phase current, rotor position and airgap lengths.

4.4.1.1 Unbalanced Electromagnetic Forces

Axial force is unavoidable in the AFSRM, much like radial force in the RFSRM. Due to the centrally placed stator, it is expected that the stator components will experience balanced forces due to the continuity of flux through the magnetic circuit. The axial force of a magnetic system with an airgap can be found by the rate of change of coenergy with respect to distance:

$$F = \frac{dW_{\mathrm{c}}}{dl_{\mathrm{g}}} \tag{4.9}$$

The coenergy can be found using the flux linkage derived from the equivalent magnetic circuit. Assuming the steel permeability is infinite and the flux travels through four airgaps of length l_{g}, the coil flux linkage is:

$$\lambda = \frac{N^2 I \mu_0 A_{\mathrm{pole}}}{4 l_{\mathrm{g}}} \tag{4.10}$$

Applying this expression into the coenergy integral, the coenergy can be expressed as:

$$W_{\mathrm{c}} = \frac{(NI)^2 \mu_0 A_{\mathrm{pole}}}{4 l_{\mathrm{g}}} \tag{4.11}$$

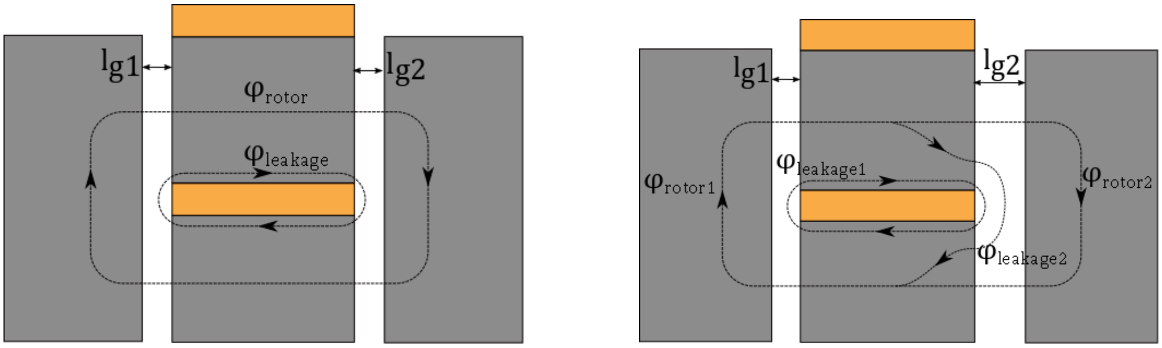

(A) Balanced airgaps $l_{g1} = l_{g2}$ (B) Unbalanced airgaps $l_{g1} < l_{g2}$

FIGURE 4.20: Simplified flux lines for stator cross section at overlap

Solving for force:

$$F = \frac{dW_c}{dl_g} = -\frac{(NI)^2 \mu_0 A}{4{l_g}^2} \tag{4.12}$$

The stator experiences this tensile force on both airgaps, resulting in zero net force. It should be noted that this expression includes a quantity of flux density, which is limited by the saturation of the iron material and therefore limits the production of axial force. In this representation, a dissimilar airgap would change the magnitude of flux passed through the system, however if all components are linked magnetically in series they each carry the same flux. Therefore, any force imbalance must be explained by unbalanced leakage flux due to dissimilar airgaps. Figure 4.20 shows the general flux path at the aligned position. Under balanced conditions, the flux that links through rotor 1 is equal to that of rotor 2. However, with a dissimilar airgap, more leakage flux occurs on airgap 2, creating larger axial magnetic forces on airgap 1.

A sweep of airgap lengths was performed in JMAG to asses the loading requirements of the outer stator pole retention. The resulting force on the segment is displayed in Table 4.5. The effect of saturation is evident due to the similarity of force magnitudes between 150A and 300A. It can be concluded that the outer stator segment should not experience axial forces exceeding 160 N.

The flux density distribution for the final case of Table 4.5 can be seen in Figure 4.21.

Coil Current	Airgap 1 (mm)	Airgap 2 (mm)	Airgap Differential (mm)	Force (N)
150	0.3	0.3	0	0.01
150	0.2	0.3	0.1	40.6
150	0.2	0.4	0.2	75.35
150	0.1	0.5	0.4	153.4
300	0.3	0.3	0	0.147
300	0.2	0.3	0.1	40.65
300	0.2	0.4	0.2	79.9
300	0.1	0.5	0.4	158

TABLE 4.5: Force on outer stator segment for various unbalanced airgaps and currents

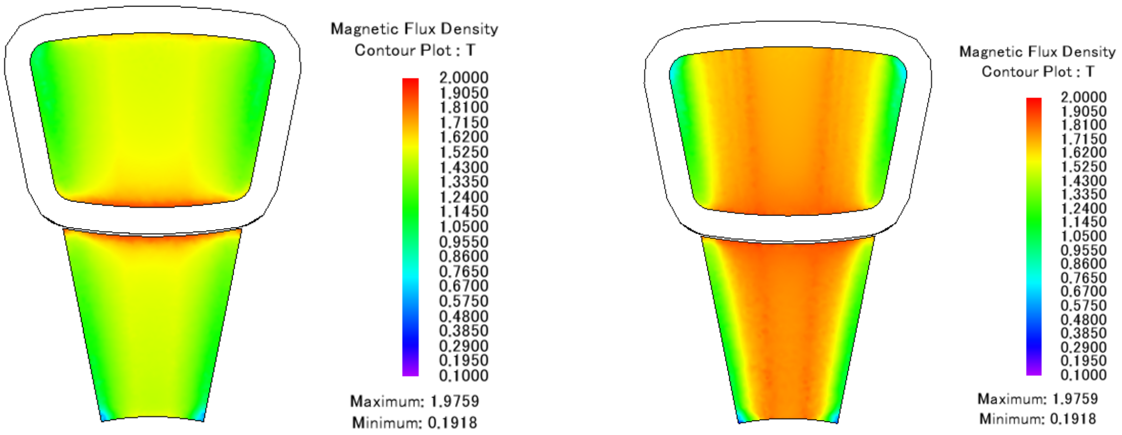

(A) Stator face on 0.5mm side

(B) Stator face on 0.1mm airgap side

FIGURE 4.21: Flux density contour plots of stator faces with unbalanced airgaps

The concentration of leakage flux can be seen on the face with 0.5mm airgap. The face with 0.1mm airgap has a less concentrated distribution of flux, indicating a larger magnetic tensile force on the face.

4.5 SMC Material Selection for Manufacturing

As noted previously, the base magnetic analysis assumed the Somaloy 700 HR 5P material for all active magnetic components. While this material has superior magnetic properties to many other SMC powders on the market, it is not suitable for prototyping due to the lack of binding agent in the powder [58]. A binding agent would enable the part to be machined from a pre-compressed and sintered blank, while SMC powders without binding agents must be compacted and sintered in their final geometry, requiring high tooling costs. Fortunately, Höganäs offers an alternative, Somaloy Prototyping Material (SPM), which does contain a binding agent and therefore is machinable. However, SPM suffers from slightly worse magnetic properties while maintaining the same mechanical properties as 700HR5P.

While the Somaloy material offer good magnetic properties, a more structurally robust material is necessary to sustain centrifugal forces on the rotor. PMG Füssen GmbH (Füssen, Germany) offers a series of machinable SMC products, among them is Siron s400b, which exhibits the highest transverse rupture strength (TRS) of the product line. As a consequence to high strength, the material exhibits a lower saturation flux density than both 700HR5P and SPM. Table 4.6 shows a breakdown of key mechanical and electromagnetic properties of the three materials and Figure 4.22 shows a plot of their B-H curves. Data for s400b at higher field strengths is limited, but may be extrapolated based on the provided saturation flux density and the permeability of free space.

Property	700HR5P	SPM	Siron s400b
Youngs Modulus (GPa)	150	100	130
TRS (MPa)	60	60	135
Thermal Conductivity (W/m^2.K)	21	20	42
B$_{\text{sat}}$ (T)	2.09	1.94	1.64
$\mu_{\text{r,max}}$	600	430	720
Resistivity ($\mu\Omega.m$)	700	300	700
Loss @ 1.0 T / 800 Hz (W/kg)	92	120	111

Table 4.6: SMC Material comparison

Based on the magnetic and mechanical properties of both SPM and s400b, SPM is selected for the stator and s400b is selected for the rotor. The high rotor speed requires highly refined dimensional accuracy and manufacturing quality of the rotor poles, which can be provided by PMG Fussen who has experience in machining SMCs.

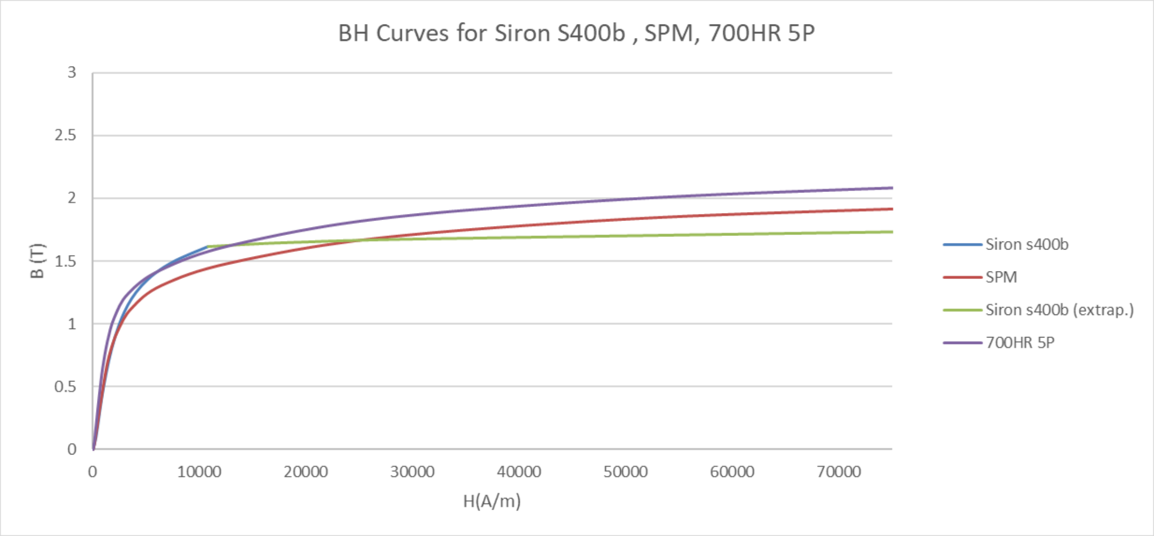

FIGURE 4.22: B-H curve comparison for 700HR5P, SPM and Siron s400b

4.6 Rotor Design

A structure must be built around the rotor poles to accurately retain their position about the stator. The concept for the rotor design is a non-ferromagnetic yoke with embedded SMC poles. This section will discuss design challenges associated with the rotor structure.

4.6.1 Rotor Pole Geometry

Previously, [1] derived a multi-level airgap feature on the rotor pole face to create a sinusoidal flux profile. This was accomplished by defining stepped cutouts on the airgap surface. The leading edge of the stepped cutouts will be used for the AFSRM design, mirrored about the centre plane of the pole segment to create identical torque profiles for both rotational directions. The stepped rotor geometry and resulting torque profile can be seen in Figure 4.23. A sinusoidal torque waveform is targeted in effort to reduce torque ripple, as the gradual rise in torque from one phase will avoid spikes from rapid rise in phase current. In this section, the further development of the rotor pole and the larger rotor structure will be discussed.

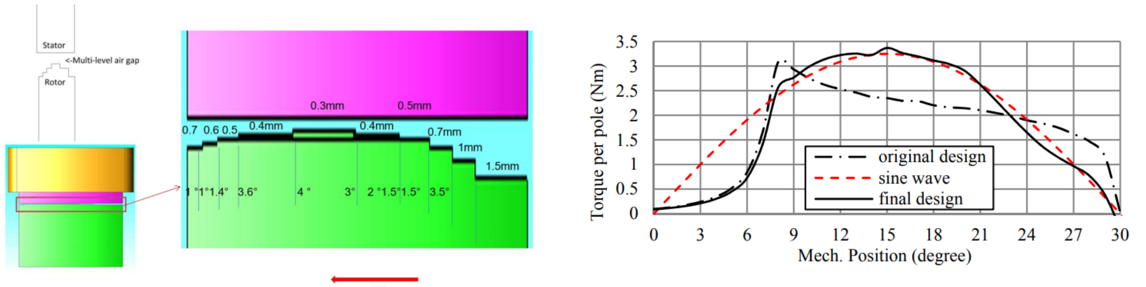

(A) Dimensions of rotor airgap face cutouts

(B) Torque profile of baseline (flat) design and final stepped geometry compared to a reference sine profile

FIGURE 4.23: Multi-level airgap design by Lin [1]

4.6.2 Rotor Pole Retention

The rotor segments must be retained by a structure that provides an accurate path for the segment rotation. The rotor disc must meet the following requirements:

- Prevent rotor/stator collision by providing adequate stiffness in the axial direction
- Prevent rotor pole fracture by providing adequate structural support against centrifugal loads at high speeds
- Minimize additional parasitic induced losses
- Minimize resonant effects of cyclic loading

An aluminum yoke is proposed for the main rotor structure. The pole segments fit into pockets in the yoke. The pole segments can be modified to include a step feature that interfaces with a retention ring, which can be fastened to the yoke. This structure is displayed in figure 4.24. The step feature is defined as a 2.5mm offset from the original pole perimeter, for one half of the pole height.

The retaining ring must provide similar radial stiffness to the yoke, otherwise shear stress will build up in the SMC pole. Additionally, the fit of the SMC pole must have similar tolerances to both the yoke and retaining ring, otherwise the SMC pole will be unevenly loaded. To quantify the potential induced losses near the airgap, a rotor segment

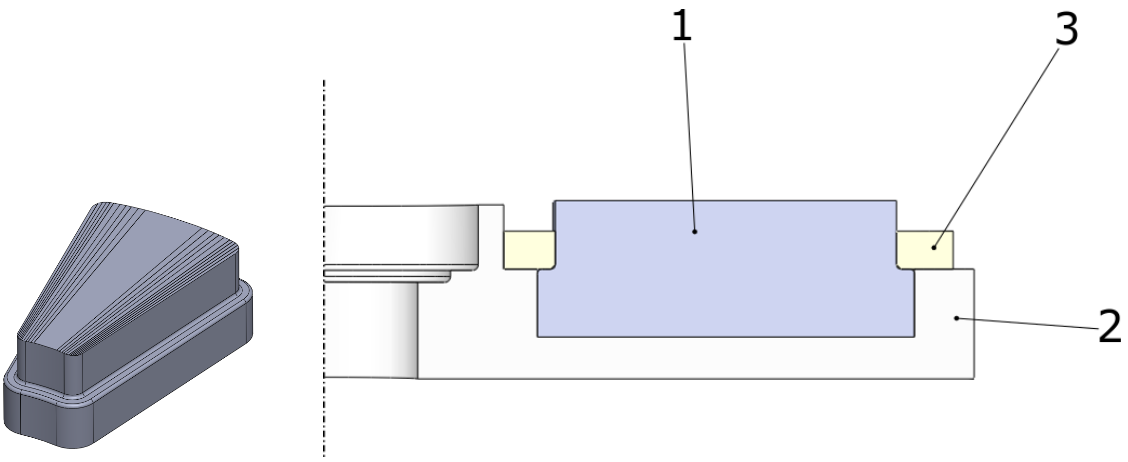

(A) Stepped rotor pole (B) 1- Rotor Pole 2-Rotor Yoke 3-Retaining Ring

FIGURE 4.24: Stepped rotor with retaining ring

was modeled in JMAG with a partitioned aluminum rotor yoke, such that the inner yoke partition occupies the axial length 2mm to 12 mm from the airgap, and the outer yoke partition occupies the remainder. The inner yoke represents the retaining ring pictured in Figure 4.24b. Figure 4.25 shows the partitioned yoke model and the resulting flux density contour plot at 150A. A region of 0.1-0.2 T is observed in the inner yoke, while the outer yoke flux density remains largely negligible. Parasitic losses in the yoke structure could therefore be mitigated by using a non-conductive retaining ring, while an aluminum outer yoke would be sufficient.

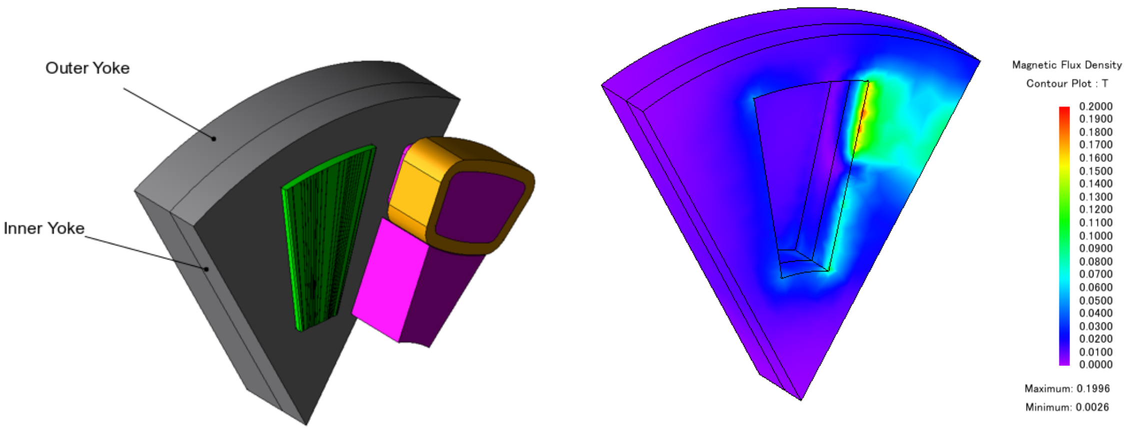

(A) Rotor Yoke partitioning for FEA loss calculation (B) Flux density contour plot for aluminum segmented yoke at 19 degrees from overlap

FIGURE 4.25: FEA simulation of aluminum yoke losses

The structural properties of the yoke and retaining ring should also be considered for the rotor design. At resonance, the relatively weak rotor structure and high axial magnetic loading has potential to result in high axial deflections, risking a rotor-stator collision. Higher stiffness and lower density are desirable to increase natural frequency outside of the range of magnetic loading frequency that is expected in the motor operating range. Additionally, higher specific damping materials are desirable to reduce vibrations that cause acoustic noise. Based on the material property requirements, carbon fiber reinforced polymer (CFRP) is an interesting candidate due to high stiffness, low electrical conductivity and promising damping characteristics compared to that of aluminum. CFRP is available in sheets of various thicknesses, and is categorized by the weave directions. Layers of woven carbon are stacked and impregnated with an polymer matrix material and cured to form a plate. CFRP sheets are available from RockWest Composites Inc (West Jordan, USA) using a 2x2 twill weave of carbon fabric encapsulated with multifunctional epoxy resin. The properties of the CFRP plate are listed in Table 4.7.

Property	Value
Fiber Type	670 GSM 2x2 Twill Weave
PMM Type	Rhino 1411 Multifunctional Epoxy Resin
CF:PMM (vol)	58:42
Thermal class	93°C
Tensile Modulus	65 GPa (0°) 14.4 GPa (45°)
Tensile Strength	103.4 MPa (0°) 482.6 MPa (45°)

TABLE 4.7: Properties of RockWest 4XX-Series CFRP Plate

A 6.1mm CFRP plate was selected for the retaining ring stock. Ducts were placed in between the rotor poles to allow for higher airflow into the airgap. The final rotor assemby model is shown in Figure 4.26a. The structure can be analyzed using a 60° section in FEA. The symmetric boundaries are defined with a frictionless normal force constraint, based on a balanced rotor where points on these planes would only deform in the radial direction. The rotor slice is shown in Figure 4.26b.

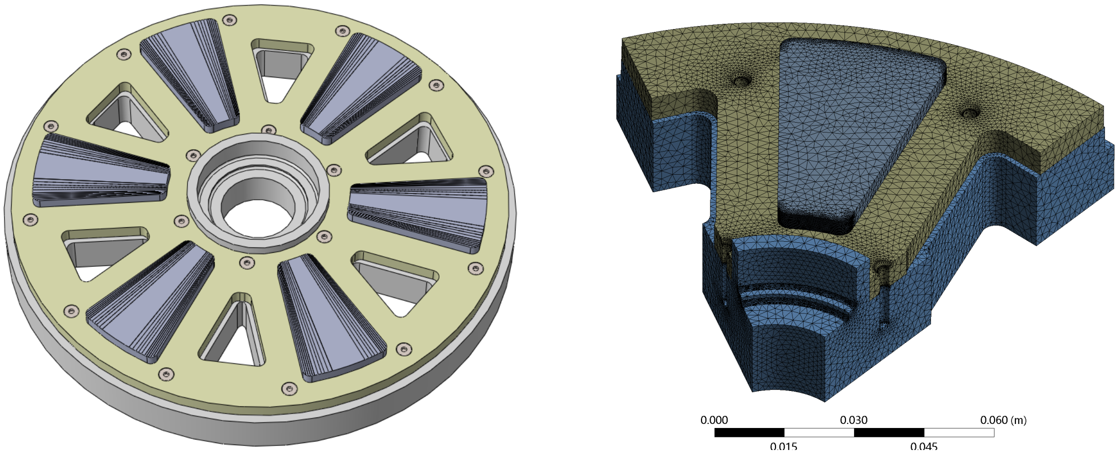

(A) Full rotor CAD model

(B) 60° reduced model in ANSYS

FIGURE 4.26: Rotor model used for structural analysis

4.6.3 Centrifugal Loading

A study of the effect of centrifugal loading on the rotor structure, specifically the relatively weak SMC, is performed in ANSYS Mechanical. The goal of the analysis is to predict fracture of any rotor components under loading, with special concern for the SMC. The anisotropic structure of the CFRP plate presents a unique analytical challenge. Assigning the 0°/ 90° stiffness globally will result in an underestimation of shear loading on the SMC pole, given that the 45° stiffness is 75% less. Ideally, the stiffness of the aluminum yoke should be as close as possible to that of CFRP, otherwise cantilever loading will take place on the pole in the radial direction. SMC loading is also highly sensitive to component fitment, as more load will be taken up by the yoke if there is a looser fit between the SMC and the CFRP. The rotor pole step creates structural weakness, as stress has the tendency to build up in the sharp corners. To mitigate this, a 1mm radius was defined on the inner and outer edges of the rotor step. An opposite radius is defined on the CFRP plate, to maximize contact area, shown in Figure 4.27a. These radii raise the question of manufacturability, where a ball-nose endmill and corner rounding endmill are needed to form the SMC radii, and the latter needed for machining the convex radius on the CFRP. However, the abrasive properties of CFRP will complicate the accurate machining of a rounded outside corner, so a chamfered edge is preferred, as shown in Figure 4.27b.

Frictional joints of $\mu_{\mathrm{f}} = 0.4$ were defined between all mating surfaces. Fixed constraints in the bolt holes were applied to the yoke and retaining ring. A rotational condition of $837 rad/s$ is applied to the assembly, and a normal force of $350N$ is applied to the rotor pole surface to simulate magnetic force.

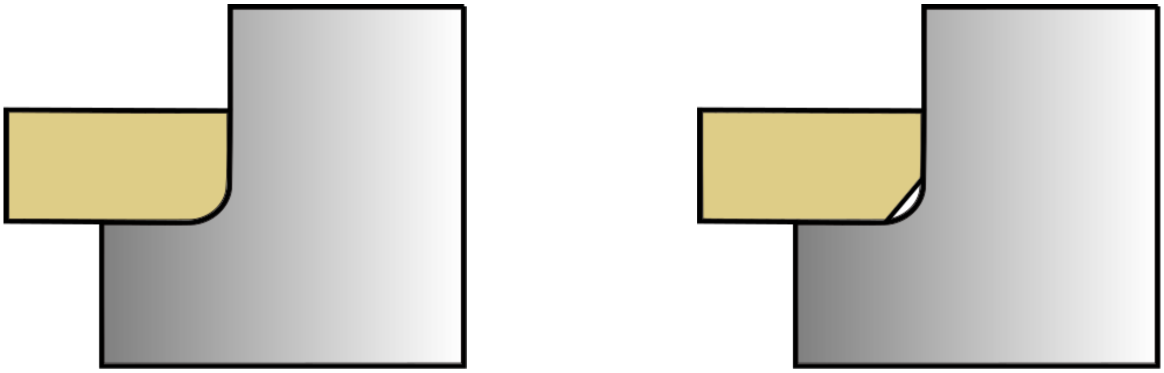
(A) Fillet/fillet

(B) Fillet/chamfer

FIGURE 4.27: Corner interface between SMC pole and CFRP retaining ring

The stress plots indicate a large compressive force on the outer faces of the SMC pole. Maximum stresses here are shown to exceed the listed TRS of 135 MPa, the type of loading must be considered for failure criteria. SMCs typically exhibit a compressive strength 5-10x larger than the TRS or tensile strength [59]. An area of concern is the shoulder on the inner radius, which would experience tensile stress from the centrifugal loading and the stiffness mismatch between aluminum and CFRP. Stress concentration here is a factor of the fillet radius, which should be larger to distribute tensile stress. Despite this, the stress on the inner radius of the shoulder does not exceed 100 MPa, and is considered within the limitations of the material for tensile strength. It should be noted that a stiffer CFRP material model creates larger buildups of compressive stress on the outer radius while alleviating tensile stress on the inner radius. Similarly, the chamfered CFRP geometry provides a relief to stress concentration in the SMC fillet.

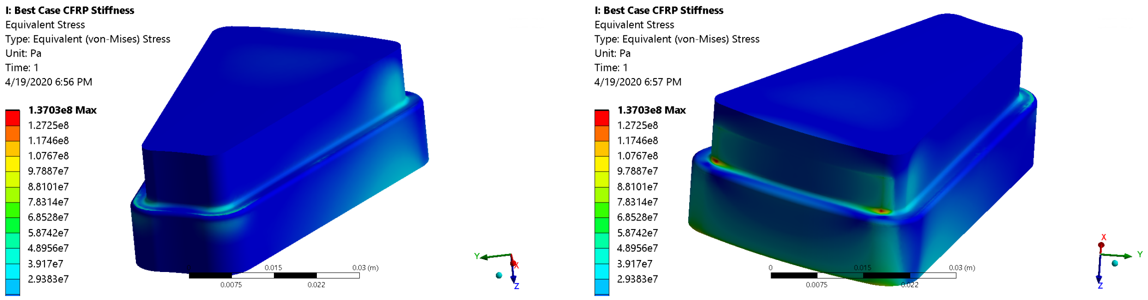

(A) 0° / 90° CFRP stiffness

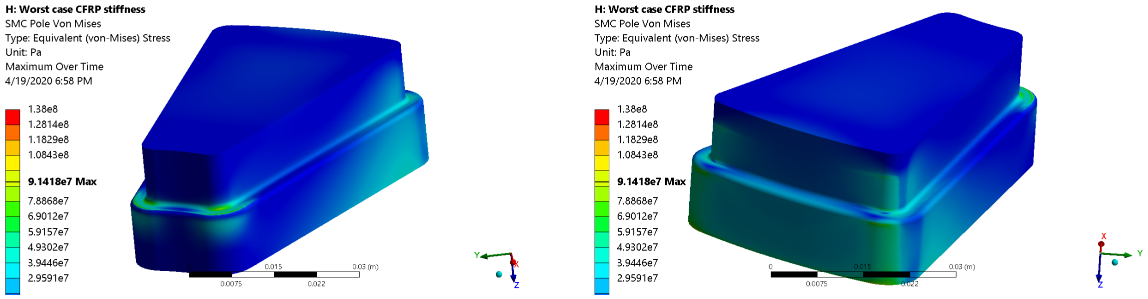

(B) 45° CFRP stiffness

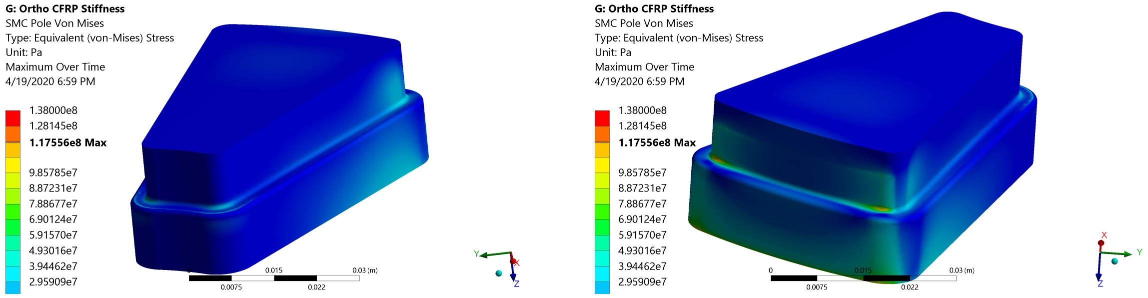

(C) Orthotropic CFRP stiffness

FIGURE 4.28: Stress contour plots of SMC pole with varied CFRP stiffness models, fillet/fillet interface.

The stress plots of the yoke and retaining ring are seen in Figure 4.30. Maximum observed stresses are well within the material strengths. Typical stress concentration in corners and bolt holes are observed. The deflection of the entire structure is seen in Figure 4.31. A 0.09mm deflection into the airgap is observed on the rotor face. This is due to the pivoting trajectory of the pole due to the center of mass location above the yoke pocket.

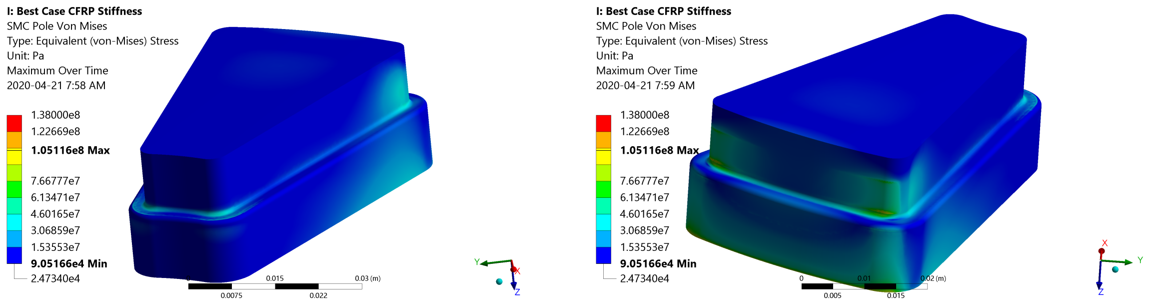

(A) 0° / 90° CFRP stiffness

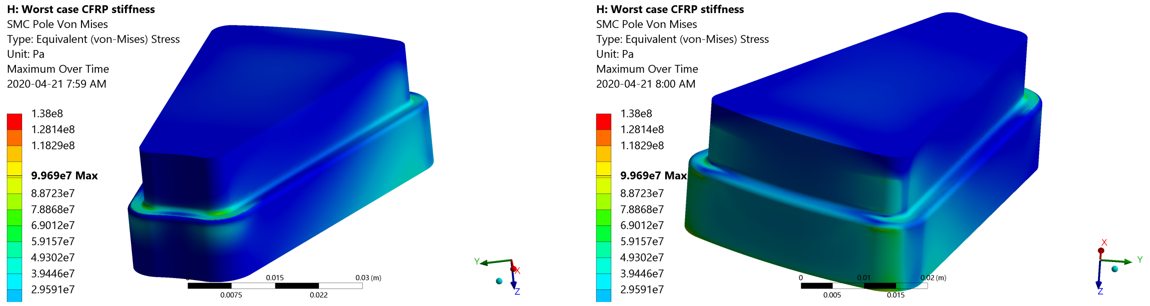

(B) 45° CFRP stiffness

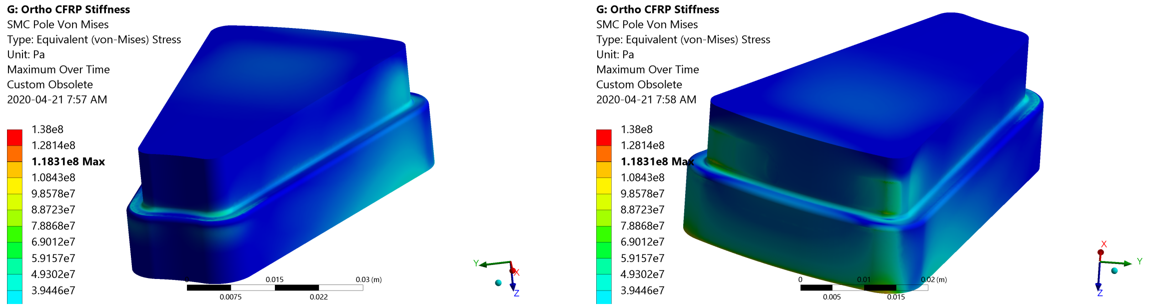

(C) Orthotropic CFRP stiffness

FIGURE 4.29: Stress contour plots of SMC pole with varied CFRP stiffness models, fillet/chamfer interface.

4.6.4 Axial Deflection

Unlike the stator, the rotor is subject to high unbalanced axial magnetic loading. Axial force depends on phase current, angle and airgap length. Rotor angle may be assumed as a direct overlap to assume worst-case conditions. Magnetic forces are opposed by rotor stiffness, and the final airgap $l_\mathrm{g} - \delta_\mathrm{g}$ is the solution to the equation:

$$K_\mathrm{z}\delta = F(I, (l_\mathrm{g} - \delta_\mathrm{g})) \tag{4.13}$$

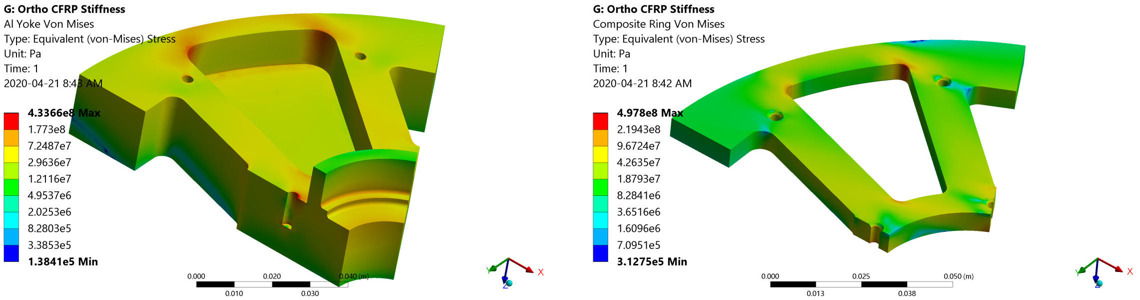

(A) Aluminum yoke (B) CFRP retaining ring

FIGURE 4.30: Von Mises stress in the structural rotor components

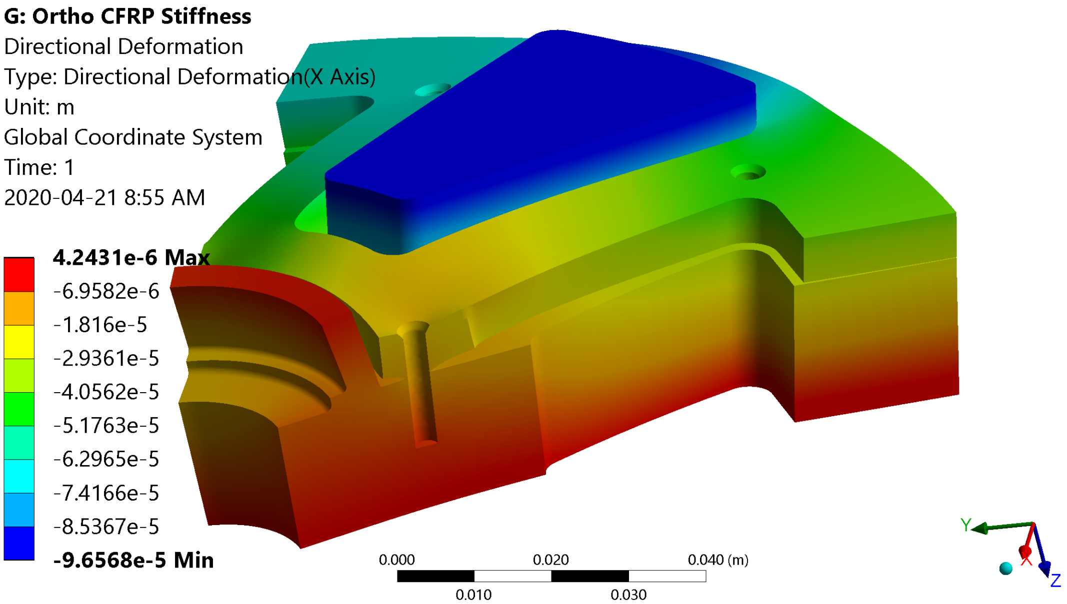

FIGURE 4.31: Deformed rotor structure under loading conditions, 200x deflection

where K_z is the equivalent rotor axial stiffness and x is the undeformed airgap length. If core permeability is assumed unsaturated, the airgap force can be approximately related to the square root of the ratio of current to airgap length. However, due to nonlinear material properties, the force must be mapped with a lookup table. The resulting equation takes the form instead:

$$K_z\delta = LUT(I, (x - \delta)) \tag{4.14}$$

which must be solved iteratively. Rotor axial stiffness was extracted by running several loading cases in structural FEA and observing maximum axial displacement. The equivalent stiffness of the rotor in the axial direction was determined to be 42.553 kN/mm. The axial force was mapped using a static magnetic simulation in JMAG at the overlapped position. The resulting surface is plotted in Figure 4.32

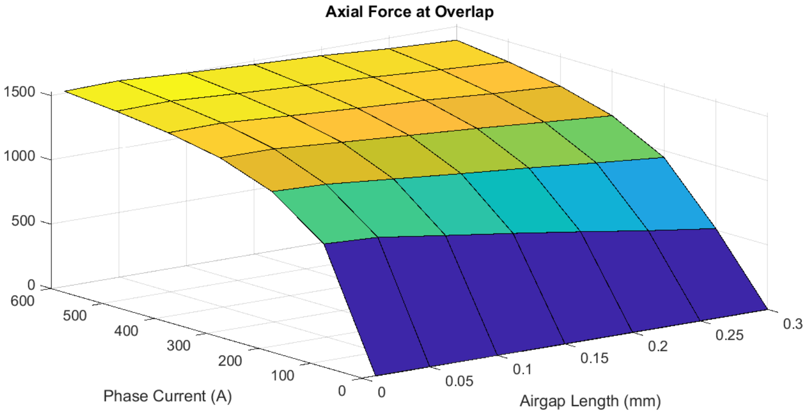

FIGURE 4.32: Rotor axial force map

The iterative calculation is as follows:

$$F_{\mathrm{z}}[k] = LUT(l_{\mathrm{g}}, I) \tag{4.15}$$

$$\delta_{\mathrm{g}}[k] = \frac{F_{\mathrm{z}}[k]}{K_{\mathrm{z}}} \tag{4.16}$$

$$x[k+1] = x[1] - \delta[k] \tag{4.17}$$

The iterative calculation was performed using an initial airgap of 0.2mm and phase current of 400A, and is plotted in Figure 4.33. The maximum deflection converges quickly to 0.0342mm, which closes the airgap from 0.2 to 0.1658 mm . This was deemed an acceptable deflection for the rotor yoke.

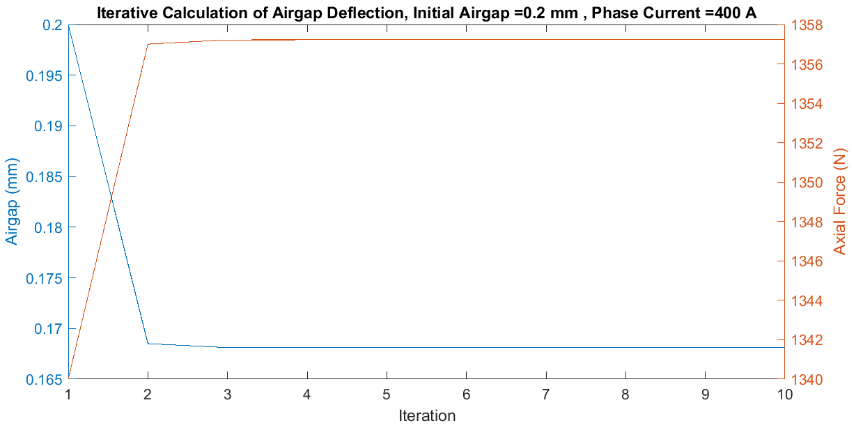

FIGURE 4.33: Iterative calculation of airgap deflection due to magnetic loading

4.6.5 Rotor Vibration Modes

Due to the unbalanced periodic forces on the rotor, vibrations are inevitable, only countered by material stiffness and damping. A resonant scenario is when the loading frequency is close to the natural frequency, and constructive interference is created, amplifying vibrational amplitude. The displacement transmissibility is a measure of vibration amplitude with and without a resonant interaction, and can be calculated as [60]:

$$G = \sqrt{\frac{4\zeta^2 {r_\mathrm{f}}^2 + 1}{(1 - {r_\mathrm{f}}^2)^2 + 4\zeta^2 {r_\mathrm{f}}^2}} \tag{4.18}$$

where ζ is the material damping factor and r_f is the ratio of input frequency to natural frequency $\frac{\omega}{\omega_\mathrm{n}}$. A plot of G is shown in Figure 4.34 and indicates that while damping is effective to combat resonance, avoiding the resonant area where $r_\mathrm{f} = 1$ is the best mitigation technique.

ANSYS Mechanical is capable of calculating vibration mode shapes for structures. The rotor yoke was imported and frictional contsraints between all mating materials was defined as $\mu_\mathrm{f} = 0.3$. Table 4.8 shows the natural frequencies and descriptions of the first six vibration mode shapes. The excitation conditions are provided to describe the nature of forces that

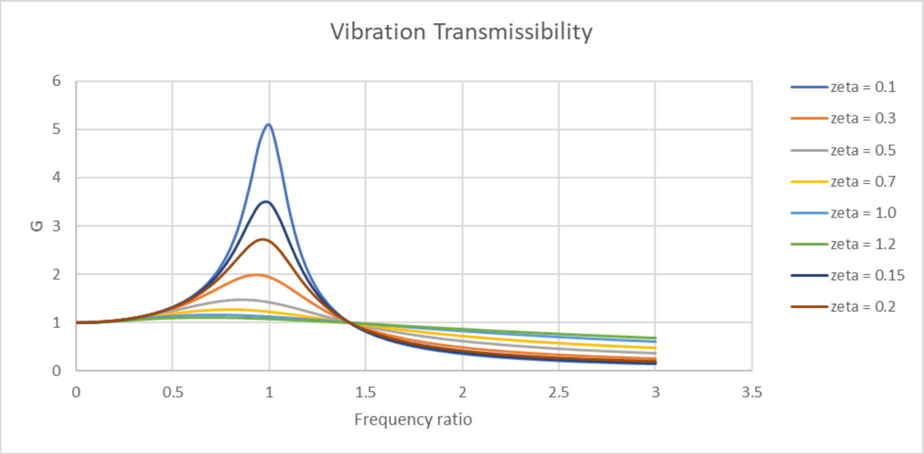

FIGURE 4.34: Transmissibility ratio for $0.1 < \zeta < 1.2$

could generate vibration similar to a mode shape, however do not necessarily reflect realistic electromagnetic loading in the motor's operation.

Mode Shape	Frequency (Hz)	Description	Excitation conditions
A	1489	Axial displacement single poles	Unbalanced axial forces
B	1491	Similar to mode shape A, oscillation points rotated 90°	Axial forces located between poles
C	1854	Torsional vibration of outer circumference	Torque ripple
D	1911	Axial vibration of outer circumference	Synchronized axial forces on all poles
E	2336	Combination of mode shapes A and B	Axial force on opposing poles and regions at 90°
F	2343	Combinations of mode shapes A and B, rotated 90°	Similar to mode shape E

TABLE 4.8: Description of rotor vibration mode shapes A-F

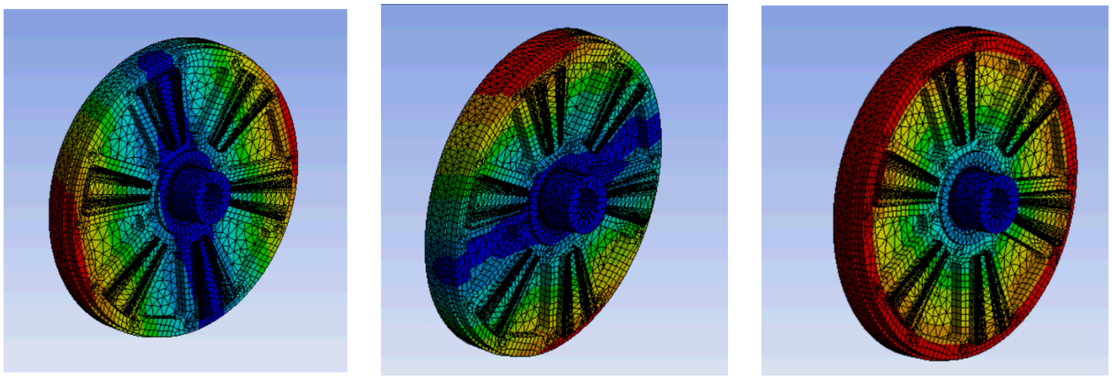

(A) Mode A (B) Mode B (C) Mode C

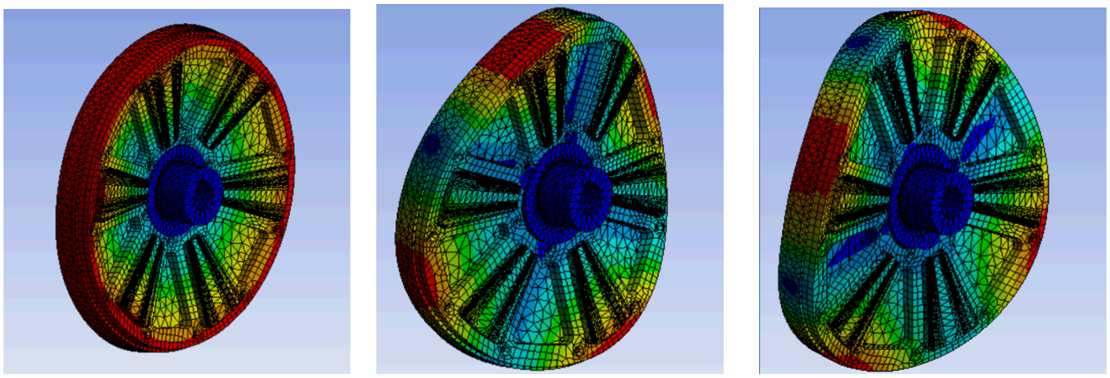

(D) Mode D (E) Mode E (F) Mode F

FIGURE 4.35: Rotor mode shapes A-F.

The main vibration excitation source will be the periodic axial pull of the rotor to the stator. Every rotation, a rotor pole passes 8 stator poles, so the relationship between rotor excitation frequency and speed will be:

$$f_{\text{vib}} = \frac{RPM * 8}{60} \tag{4.19}$$

With a maximum speed of 8000 RPM, the maximum excitation frequency will be $f_{\text{max}} = 1066.7Hz$ or $r_{\text{f}} = 0.71$ for mode shape A. Interpolating on the transmissibility graph for worst case damping $\zeta = 0.1$, the transmissibility ratio is approximately 2.0. While the transmissibility indicates that a minor amplification may occur due to resonance, a more detailed analysis is required to determine what the true effect would be. The axial loading is non-sinusoidal and the harmonic content could excite other higher order modes that are not shown. Additionally, the damping properties of the CFRP material are not fully understood, and while it is expected to provide good damping, experimental work is necessary to characterize the material. To combat this uncertainty, a pattern of threaded holes were designed into the back of the rotor yoke, such that a series of ribs could be bolted on if excessive vibration is detected, shown in Figure 4.36. The ribs are made from the same Al 7075 as the rotor yoke, and may be attached by two countersunk bolts into the back of the rotor yoke.

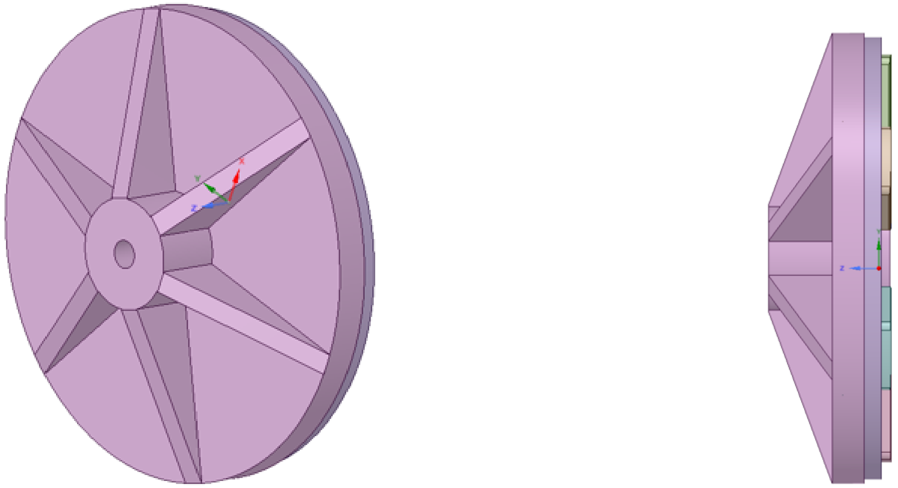

FIGURE 4.36: Bolt-on ribs to increase rotor natural frequency

The vibration mode shapes A-F are identical but natural frequencies are 10-30% higher with the rib features listed in 4.9.

Mode	Frequency (Hz)	Frequency (Hz) with Ribs
A	1489	1865
B	1491	1866
C	1854	2086
D	1911	2484
E	2336	2730
F	2343	2732

TABLE 4.9: Rotor mode frequencies with and without structural ribs

4.7 Motor assembly design

The machine may be arranged as a rotating case (shaft mounted) or rotating shaft (peripheral-mounted) configuration. The rotor design may be held mostly identical between the two designs, however the stator must be reconfigured to allow the phase cables to be routed through the hollow shaft for peripheral-mounted configuration. This configuration is challenging for an SRM of such high continuous current, due to the number of cables of large gauge needed to route through the inner race of the selected bearing. However, the configuration benefits from higher rotor stiffness due to the support on the outer radius of the rotor plates. A qualitative comparison of the two configurations can be found in Table 4.10.

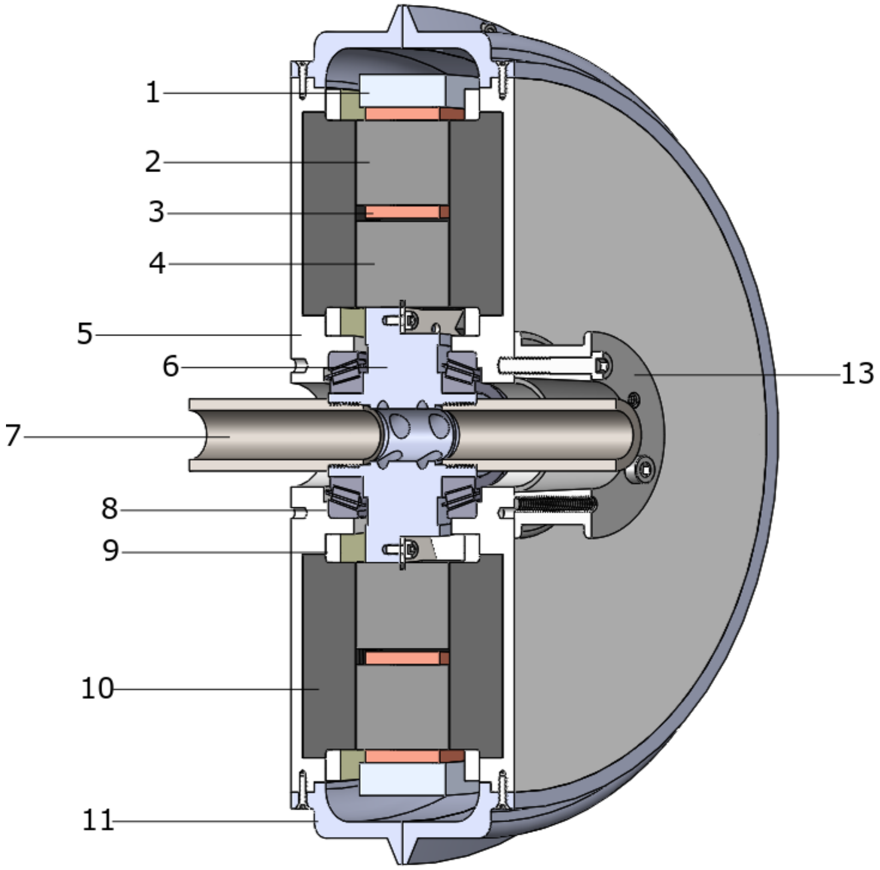

Figure 4.37: Cross section view of shaft-mounted AFSRM

Figure 4.37 shows the cross-sectional view of the shaft-mounted AFSRM. The stator frame (1) is a ring of aluminum that holds all stator poles in place. Each stator "module" is comprised of an outer pole (2), coil (3) and inner pole or flux return pole (4). The central hub (6) supports two bearings (8) and has a pattern of conduits for phase cable routing. Not shown is the stator spine, which connects the central hub to the stator frame with "spokes" that extend in between the stator modules. Hollow half-shafts (7) support the motor structure and would connect to the vehicle frame. The rotor plates (5) support the rotor poles (10) in pockets cut to their profiles. A composite retaining ring (9) fits to the smaller perimeter of the rotor pole and is bolted to the rotor plate to secure the poles axially. The plates are connected by the outer collars (11), which have a flange to bolt together. A timing pulley (13) transmits the torque to the load.

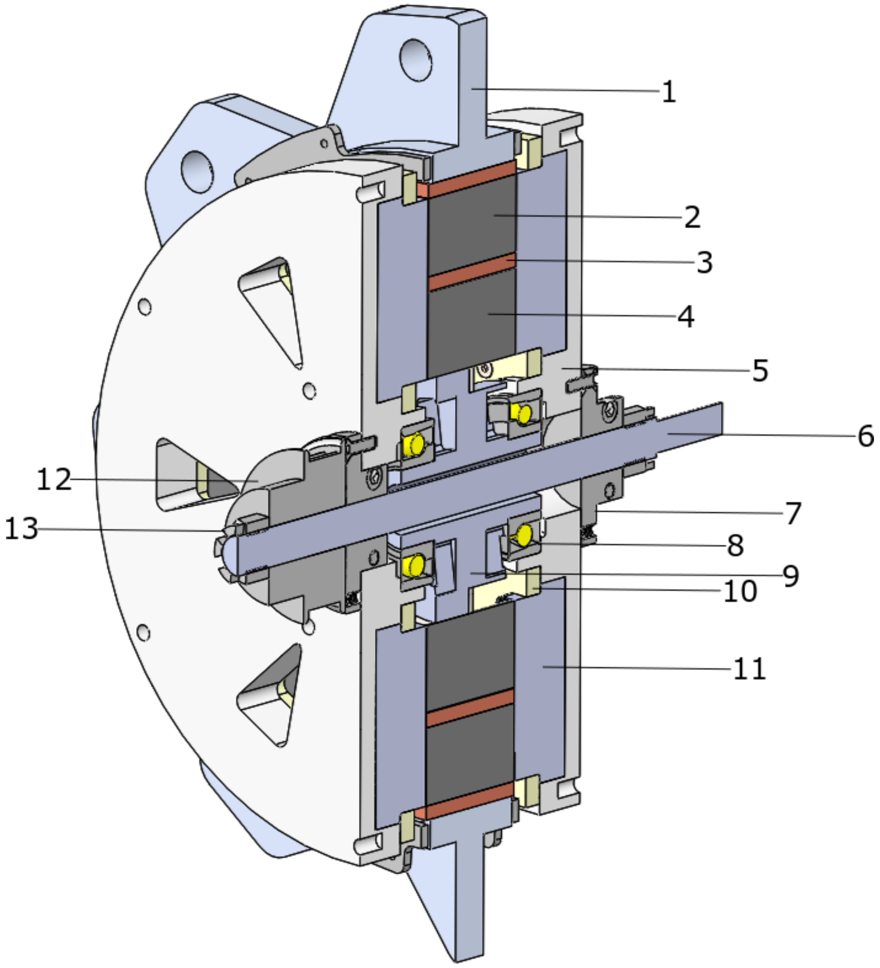

FIGURE 4.38: Cross section view of peripheral-mounted AFSRM

Figure 4.38 shows the cross sectional view of the peripheral-mounted AFSRM. The rotor construction is similar to the shaft-mounted configuration, with poles (11) embedded in the rotor plates (5) and secured with the retaining ring (10). The stator construction is similar, however this design features mounting tabs on the outside of the ring. Two angular contact bearings (8) support the rotor plates. Rotor plates are shown with openings to improve airflow. The rotor plates are connected with a shaft (6) which is keyed to the rotor flange adapters (7), which are bolted to the rotor plates. A timing belt pulley (12) is fixed to the shaft and rotation is locked with a setscrew. Two locknuts (13) pre-load the bearings and retain the shaft axially.

Design Aspect	Shaft-Mounted	Peripheral-Mounted
Heat dissipation	Possibility for air entry through ducts in rotor plate. Poor conductive thermal path from stator coils to mounting components.	Air entry through airgap. Excellent conductive thermal path to mounting components.
Rotor Rigidity	Support for plate on internal and external radii of rotor plate	Cantilever support for rotor forces supported by bearing race and yoke stiffness only.
Cable routing	All phase and sensor cables must be run through center axle	Cables may be run from outer radius.
Airgap Adjustability	Requires specialized spacers for outer radius	Single spacer for bearing seat

TABLE 4.10: Design aspect comparison between rotating frame and stationary frame AFSRM concepts.

Based on the thermal and cable routing advantages, the peripheral mounted design was selected for prototyping. A rotating case machine would be advantageous for in-wheel applications, however the torque speed characteristics of this AFSRM do not justify it. An exploded view of the assembly is visible in Figure 4.39.

4.7.1 Stator Assembly Design

The assembly is achieved by first bolting the spine to the hub. Inner stator poles are slid into their slots on the spine. The spine is then bolted into the stator ring. The outer poles with the completed windings are then inserted into the ring. While fitting the rotor, circular shims of 0.1mm thickness are placed on the hub to space out the airgap. The stator is then filled with encapsulant and left to cure. Finally, a cable retention ring can be bolted onto either side of the stator to hold the foil tabs flat. The cable retention ring also allows the outer surface of the stator ring to act as a tray for the intra-phase cables.

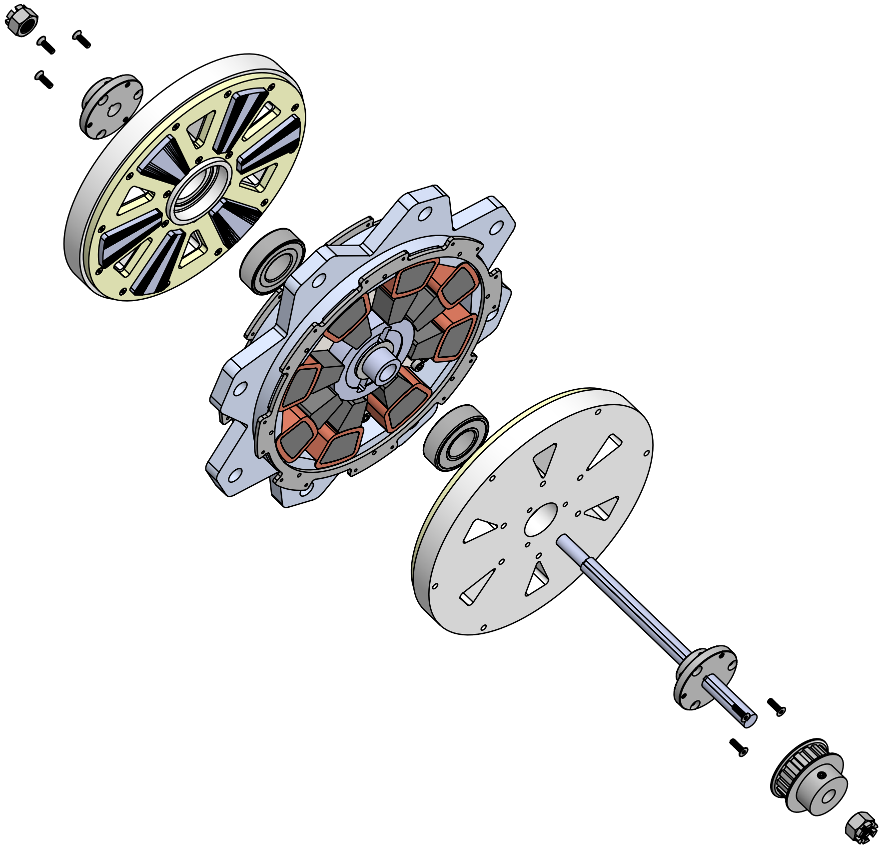

Figure 4.39: Exploded view of AFSRM assembly

The encapsulation mold is an aluminum plate with recesses for the stator poles. The mold plate creates the flat surface between the poles and the recesses locate the poles axially. The stator is bolted to the mold through the hub and clamped on the mounting tabs, then filled with the epoxy encapsulation. A drawing of the mold is shown in Figure 4.44.

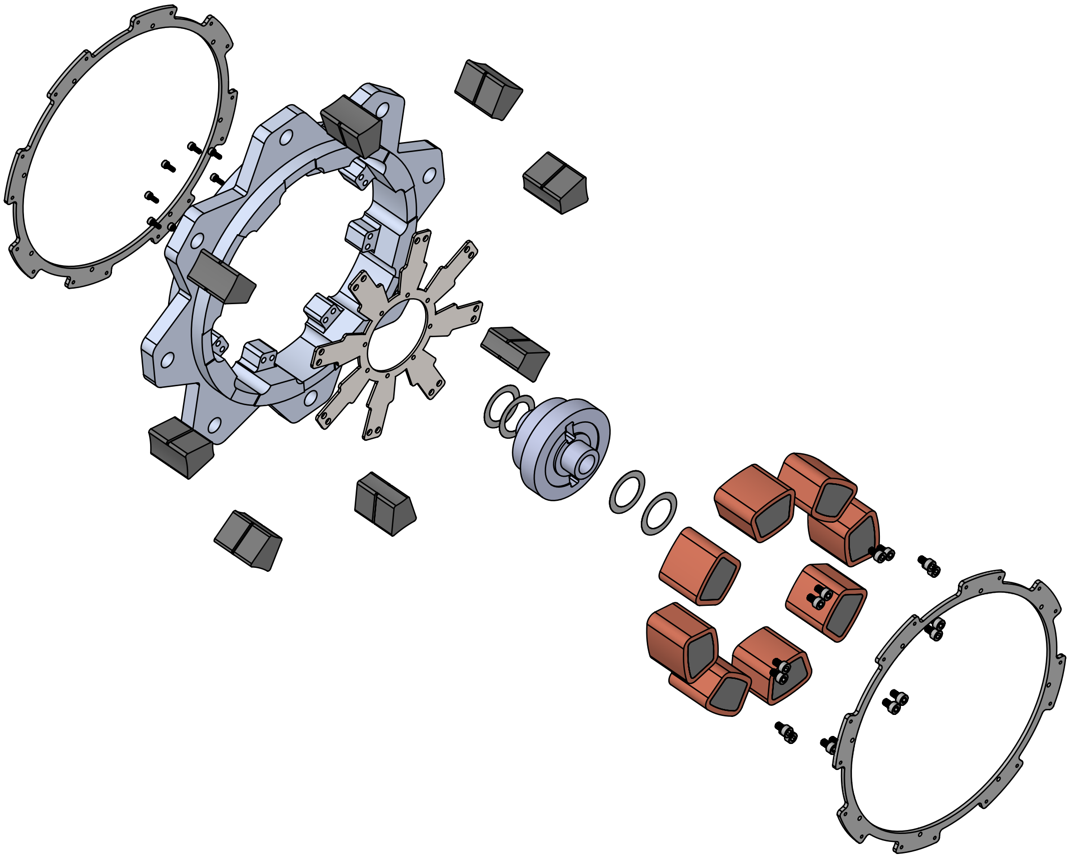

Figure 4.40: Exploded view of AFSRM stator

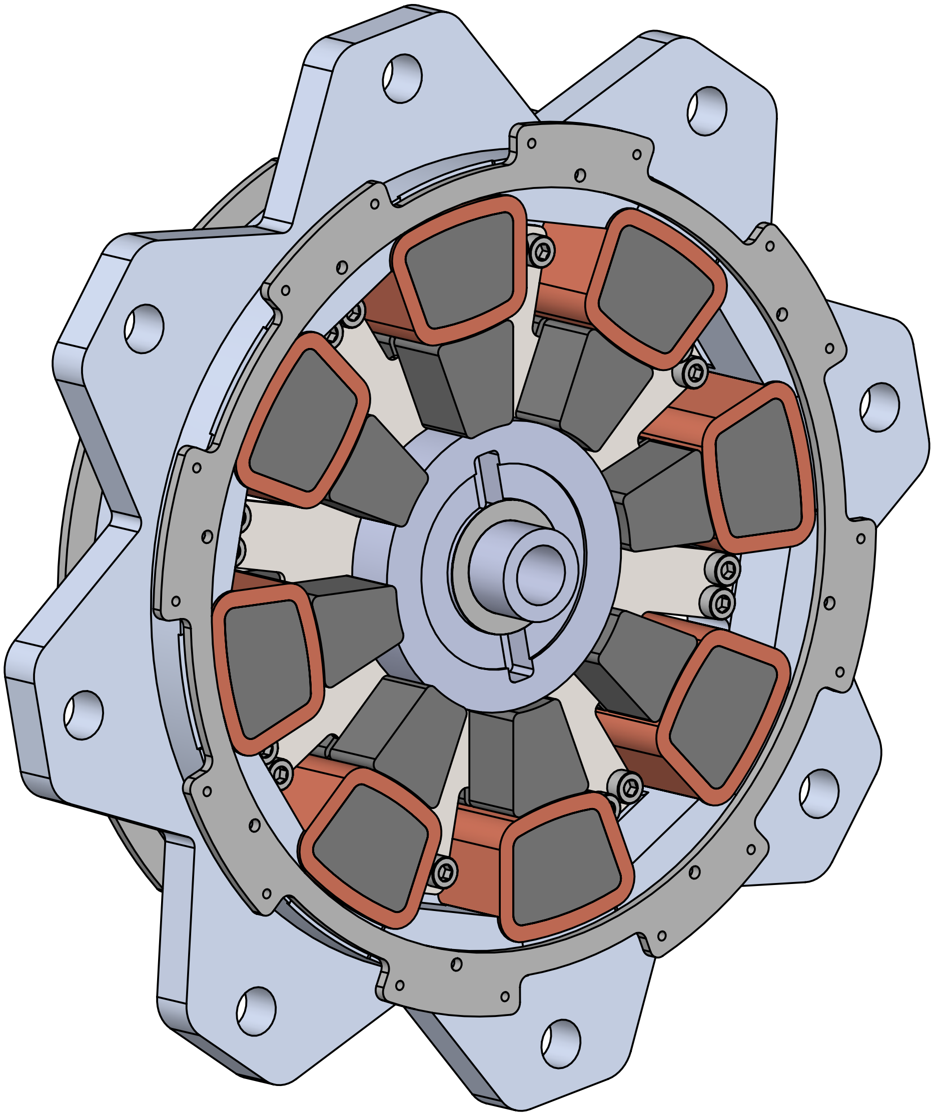

Figure 4.41: AFSRM stator assembly shown without encapsulation

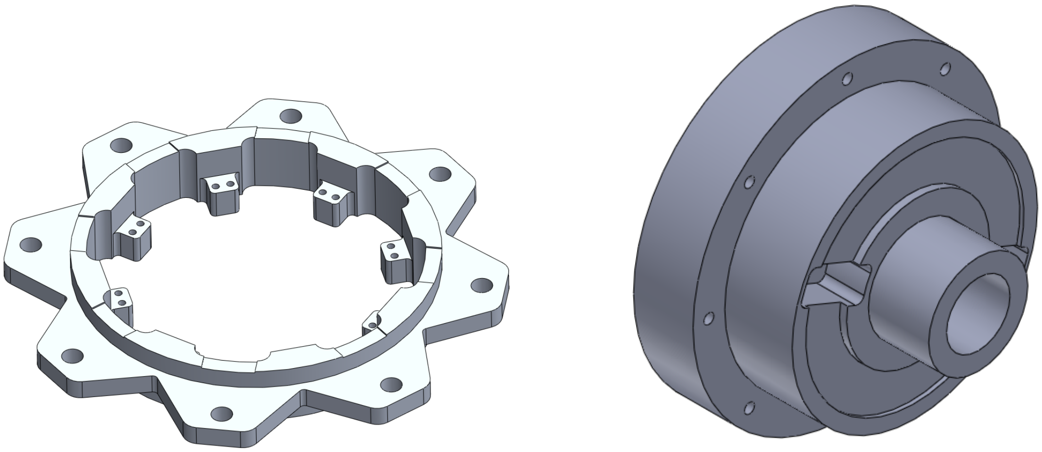

(A) Aluminum ring that houses all stator components (B) Aluminum hub that holds bearings and spine

Figure 4.42: Stator hub and ring

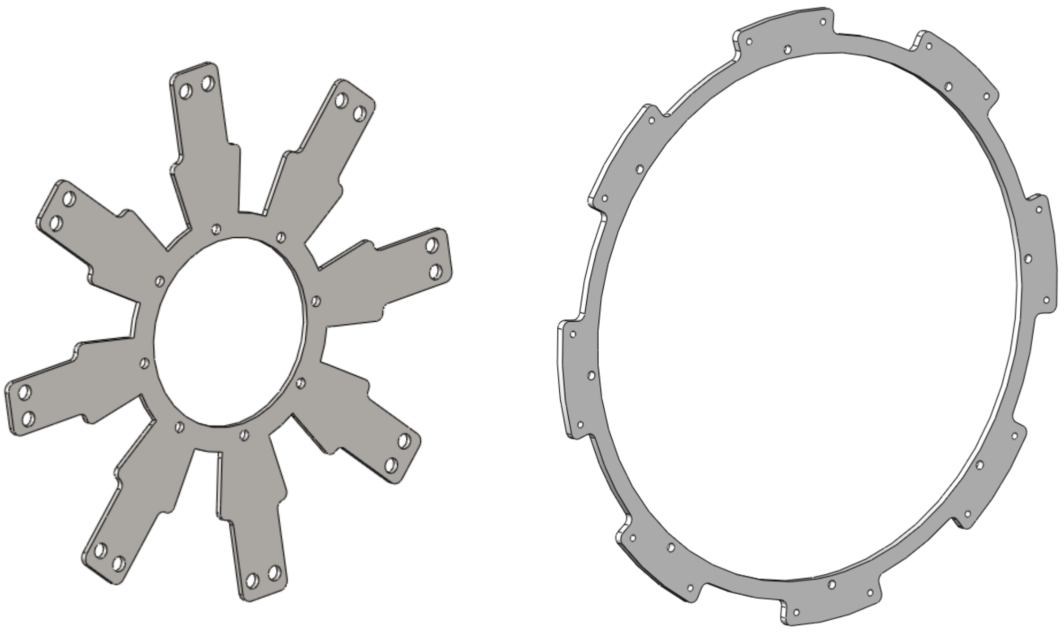

(A) Stainless steel spine with extended spokes to interface with outer ring

(B) Stainless ring that bolts around stator circumference to ensure foil tabs and cables stay in place

Figure 4.43: Stator spine and cable retention ring

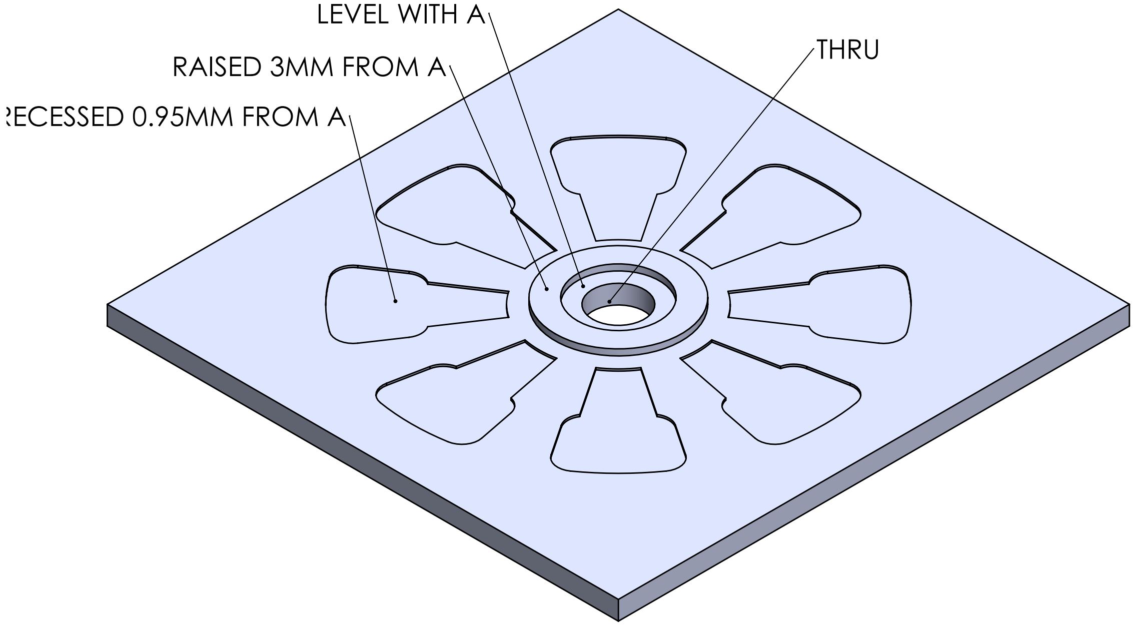

Figure 4.44: Encapsulation mold plate

4.7.2 Bearings

The selected bearing is an angular contact ball bearing from SKF, model number 7205-BE-2RZP. Angular contact was selected based on the high axial loading and tight airgap tolerances. The manufacturer calculation tool indicates a maximum bearing friction of 41.4 N.mm at maximum speed and loading conditions. A preload of 100 N is also specified. The tolerances for the bearing racings to the stator hub and rotor yoke are as follows:

- Inner race to stator hub: K6/p6 for a 25mm diameter (transition fit)
- Outer race to rotor yoke: H7/h5 for a 52 mm diameter (sliding fit)

Bearing puller pockets are designed into the stator hub to allow clearance when extracting the bearings. The fit to the rotor yoke is intended to facilitate removal and reinstallation of the rotor plates during assembly.

4.8 Summary of Overall Dimensions

The overall dimensions of the motor design are shown in Figure 4.45. The mass estimates from the CAD model are listed in Table 4.11.

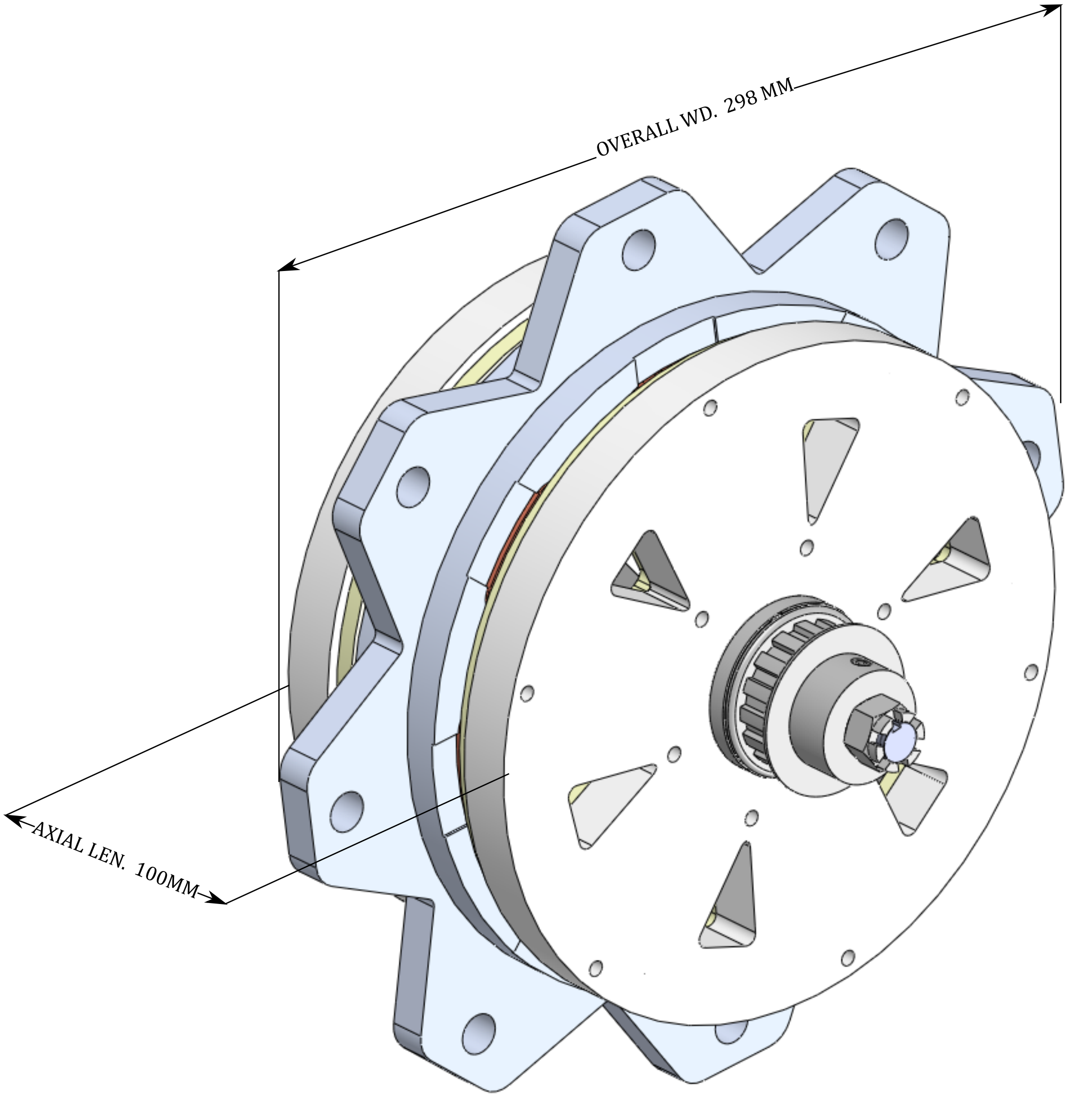

Figure 4.45: CAD Model of AFSRM assembly

Item	Mass (kg)
Copper	1.13
Stator Iron	3.18
Rotor Iron	3.50
Total Active	7.81
Full Motor	14.4

TABLE 4.11: Mass breakdown of the AFSRM

Chapter 5

Detailed Performance Analysis

This chapter will use the static characteristics of the frozen motor design from Chapter 4 and attempt to accurately predict its performance in a traction application. A numerical model for the iron losses is tuned with corner cases in FEA. The control trade-offs are studied, and switching angle tables are computed for both optimal efficiency and optimal torque quality. Finally, a Lumped Parameter Thermal Model (LPTM) is developed to predict the continuous and instantaneous loading capability.

5.1 Motor Characteristics used for Performance Analysis

Figures 5.1, 5.2, 5.4 below show the static characteristics used for detailed performance analysis on the AFSRM. Additionally, the dynamic voltage at 4000 RPM is plotted in Figure 5.3.

5.1.1 Iron Loss Calculation

In order to simulate the efficiency of the AFSRM, a numerical model for the iron losses must be developed. Conduction angles are typically determined by optimization, which requires

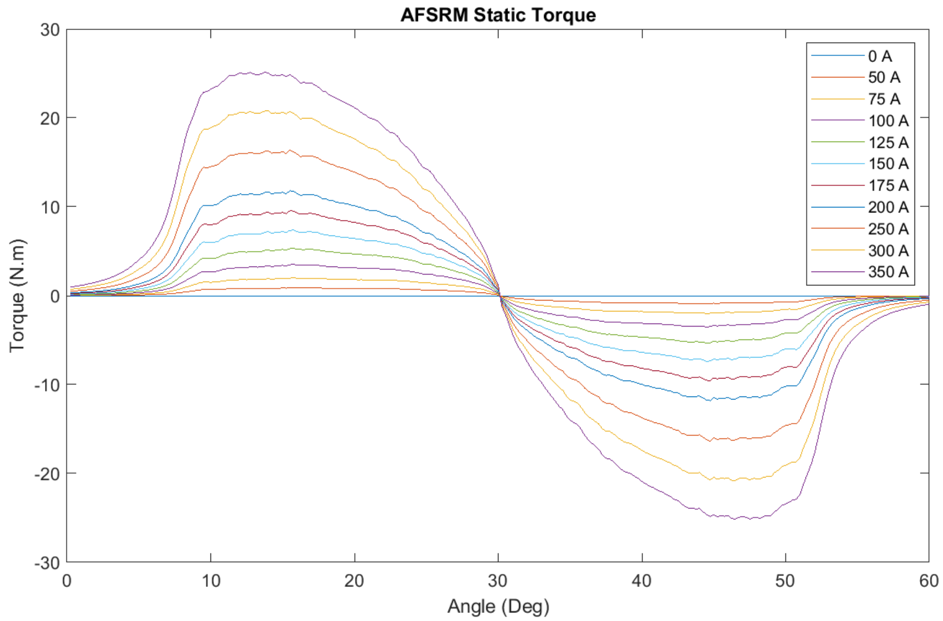

Figure 5.1: Static Torque Characteristics

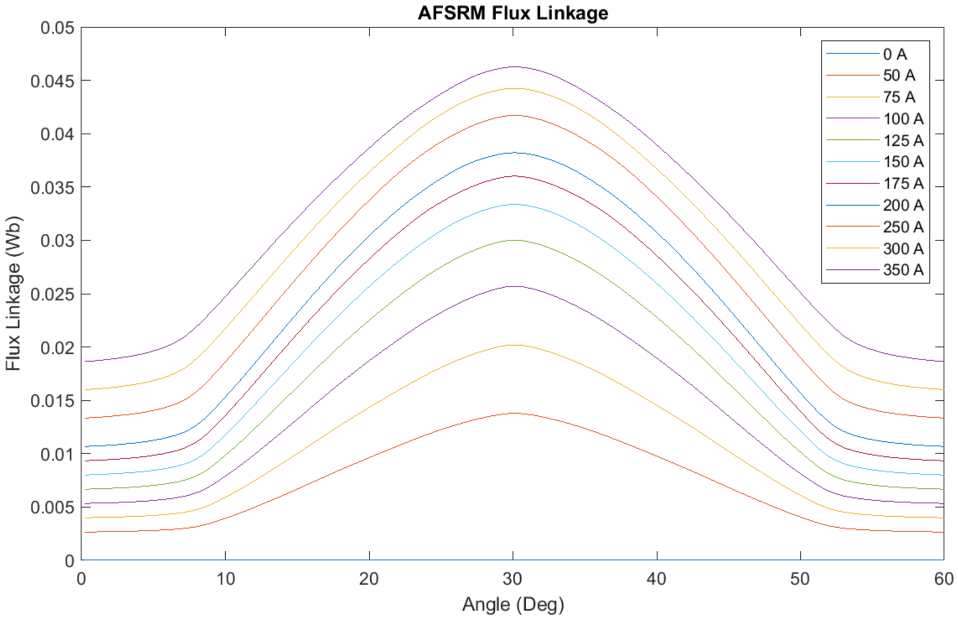

Figure 5.2: Static Flux Linkage

a cost function. The iron losses can be generated from FEA however the calculation time is prohibitive for a cost function. A lookup table would also be tedious to populate due to the

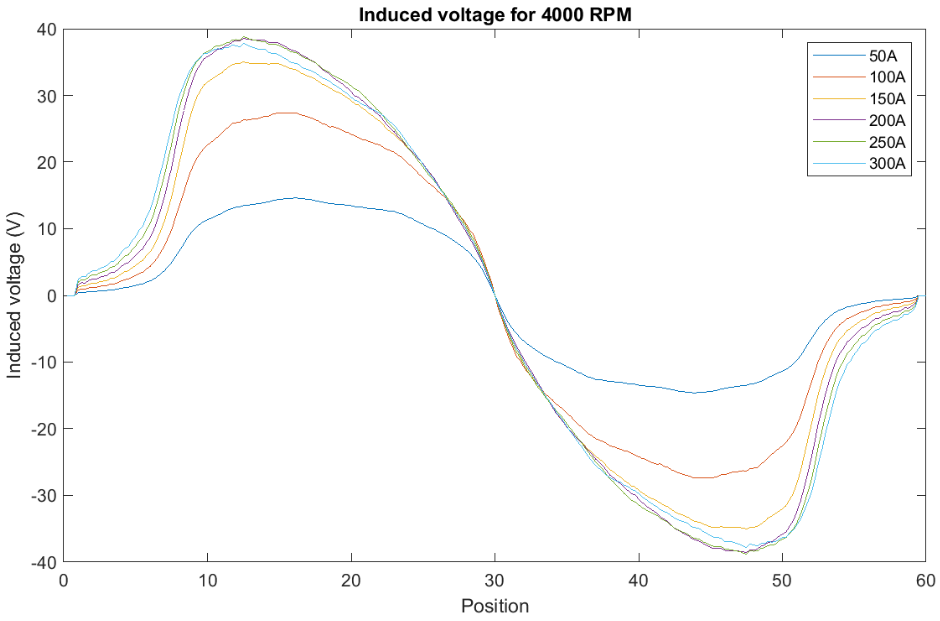

Figure 5.3: Dynamic Voltage

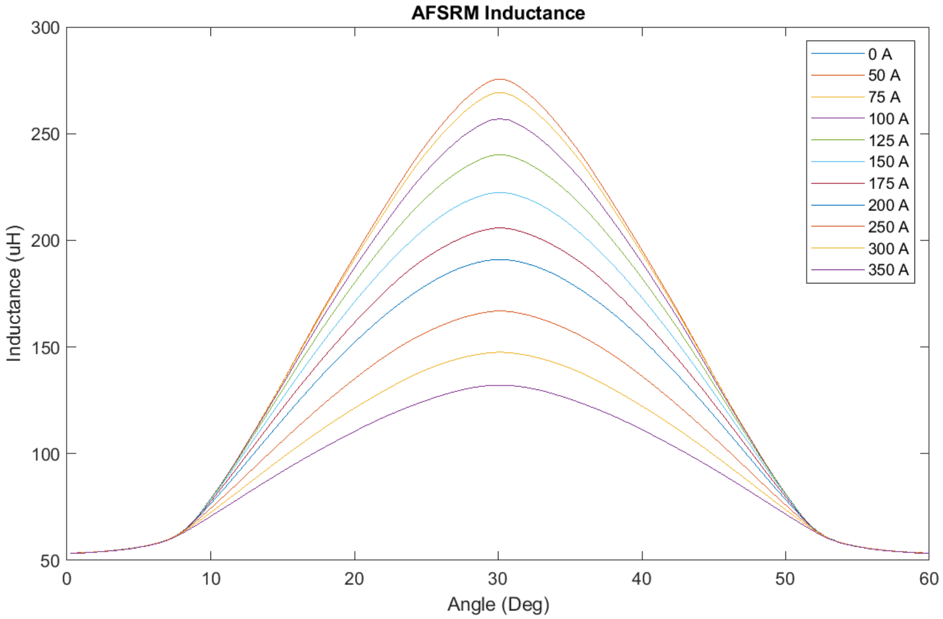

Figure 5.4: Inductance

large number of combinations of switching angles. Therefore, a numerical model should be built for iron losses.

The flux density in the ferromagnetic components can be quantified by an average elemental flux density from FEA. The average elemental flux density weighted by the element volume is known as an integral average flux density, which is computed by:

$$\bar{B} = \frac{\sum B_{\text{element}} V_{\text{element}}}{V_{\text{body}}} \tag{5.1}$$

where B_{element} is the flux density in the element, V_{element} is the volume of the element and V_{body} is the volume of the meshed body. An integral average is suitable for components with refined meshes in critical flux path areas and coarser mesh in others. For each AFSRM component, the integral average $\bar{B}$ is calculated for each position and current of the static characteristics FEA simulations. The resulting data is used to populate a LUT in the dynamic model, returning a flux density profile $\bar{B}(t)$ for each component during the simulation of a single electrical cycle, which can then be used to calculate the iron losses in each lumped body:

- $\bar{B}_{\text{r}}(t)$ the flux density profile for the rotor segment
- $\bar{B}_{\text{os}}(t)$ the flux density profile for the outer stator segment
- $\bar{B}_{\text{is}}(t)$ the flux density profile for the inner stator segment, or flux-return piece

The trace is sampled for one 60° electrical cycle, whose duration can be calculated from the speed in RPM:

$$t_{\text{elec}} = \frac{\theta_{\text{elec}}}{6 * RPM} \tag{5.2}$$

The frequency that the stator components will experience the flux density profile repeating is at $\frac{1}{t_{\text{elec}}}$, thus the stator flux density profile is concatenated onto itself once to provide realistic data for transformation into the frequency domain. However, the rotor poles will experience the magnetization cycle at $\frac{8}{6}$ times the frequency due to the larger number of stator poles. Thus, the rotor flux density profile is concatenated onto itself with a $\frac{3}{4}$ electrical cycle. The flux density profile is transformed into frequency space using the fast Fourier transform (FFT), and taking the absolute value as the amplitude. Once the average flux density signal is decomposed into sinusoidal components, an analytical model can be used to calculate the iron losses. The transformation can be seen in Figure 5.5.

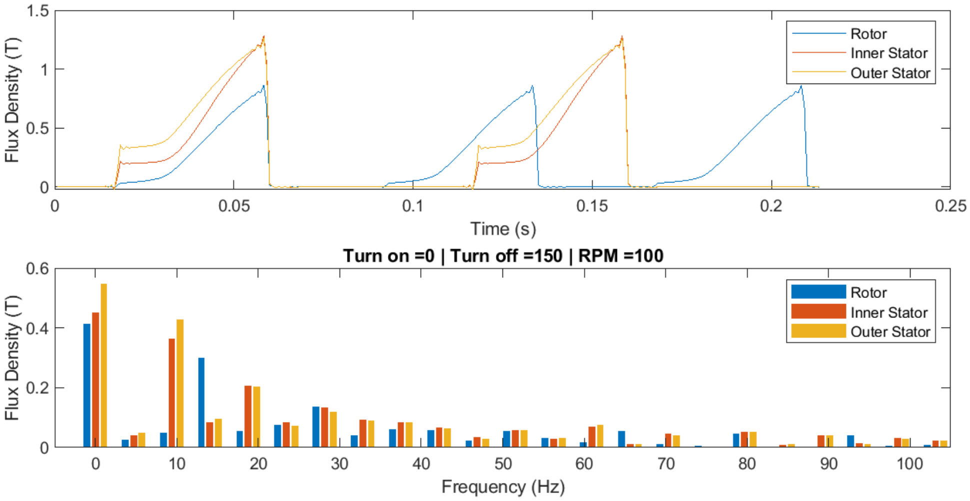

FIGURE 5.5: Average flux density profiles for $I_{\text{targ}} = 150A$ and $N = 100RPM$ and their representation in frequency domain.

The iron loss can be estimated using the Bertotti equations:

$$P_{\text{Fe}} = K_{\text{ec}}(B_{\max} f\delta)^2 + K_{\text{hyst}} f B^{\alpha} + K_{\text{excess}} f^{1.5} B^{1.5} \tag{5.3}$$

where K_{ec}, K_{hyst} and K_{excess} depend on the material properties. Loss properties are provided by the manufacturer in the form of tabular data from measurements and coefficients cannot be directly interpreted. Coefficients can instead be obtained by fitting to a sparse sweep of loss cases in FEA. By generating flux density signals for a variety of combinations of switching angles at various speeds and simulating the iron losses of each case in FEA, a baseline is established which can be used to fit coefficients to the Bertotti model. The 27 cases were generated using the combinations of the following operating conditions:

$$\theta_{\text{on}} = 0^{\circ}\ ,\ 45^{\circ}\ ,\ 60^{\circ} \tag{5.4}$$

$$\theta_{\text{off}} = 90^\circ \;,\; 120^\circ \;,\; 150^\circ \tag{5.5}$$

$$N[RPM] = 100 \;,\; 3000 \;,\; 7000 \tag{5.6}$$

$$I_{\text{targ}} = 150A \tag{5.7}$$

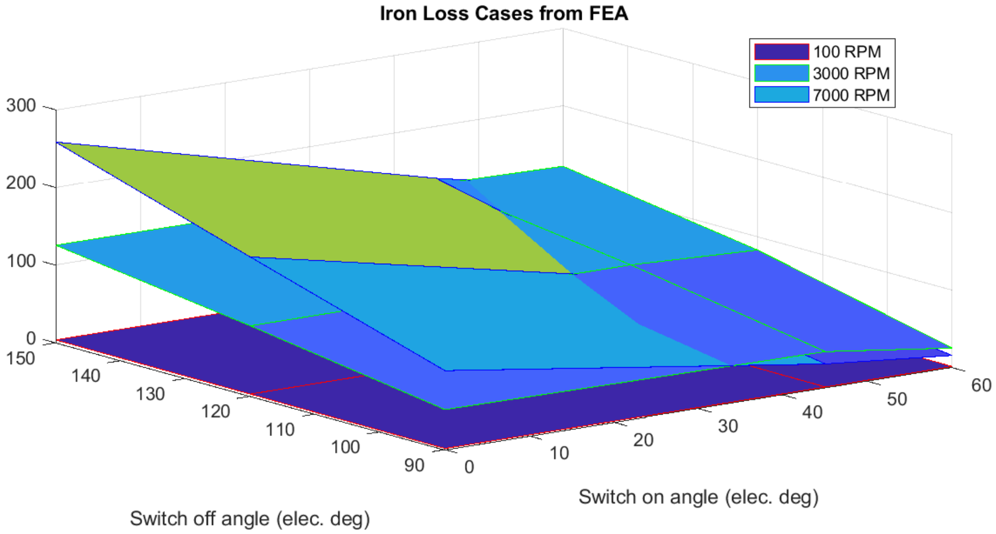

Figure 5.6: Iron loss results for swept conduction angles from FEA

Several trends can be observed from the FEA results plotted in Figure 5.6. Firstly, a longer conduction event results in higher overall iron loss, due to the larger buildup of flux. Secondly, higher speed will produce a larger loss providing the phase is switched on early in the cycle. For switch on angles 45° and 60.0°, induced voltage is preventing a buildup of flux in the phase, lowering the losses above the base speed. Finally, a delayed switch off angle will produce higher losses due to the high flux density near the aligned position.

While the dynamic model is provided average flux density lookup tables for each component, the direction of flux is not taken into account. Therefore, a situation in which the average rotor flux density is constant as it sweeps across the stator pole would see little change in average flux density, however the directional rate of change would induce significant losses. While the FEA is able to calculate these losses on an element-wise scale, the Bertotti equation employed by the dynamic model would not account for the directional rate of change of constant absolute flux density. To combat this discrepancy, a fourth coefficient K_4 is introduced that scales the product of average flux density over the conduction cycle and the frequency of the flux density:

$$P_{\text{Iron}} = P_{\text{Bertotti}} + K_4 B_{\text{avg}} f \tag{5.8}$$

Both 3-coefficient and 4-coefficient models were fitted to the FEA results using MATLAB function fminsearch. The cost function is defined as the root mean square error (RMSE) between all loss cases. The RMSE from both models are shown in Table 5.1. The optimized coefficients are listed in Table 5.2.

Material	3 Coefficient RMSE (W)	4 Coefficient RMSE (W)
Siron s400b	4.341	3.890
Hoganas SPM	3.527	2.260

Table 5.1: RMSE of iron loss fit to FEA results

Material	K_{ec}	K_{hyst}	K_{excess}	K_4
Siron s400b	0.13887	9.74689e-05	0.00023923	0.075827
Hoganas SPM	0.049885	0.00011123	1.11873e-05	0.037664

Table 5.2: Optimized coefficients for iron Loss model

The losses are validated with two other operating points, also computed in FEA, however were not part of the model fitting. A summary of the loss calculation is shown in Table 5.3.

Point	Speed (RPM)	I_{targ}	θ_{on} , θ_{off}	FFT Rotor loss (W)	FEA Rotor loss (W)	FEA Stator loss (W)	FFT Stator loss	%Error (Rotor)	%Error (Stator)
1	4000	175 A	24°, 132°	83.36	84.72	78.49	77.18	-1.6%	-1.7%
2	6000	100 A	15°, 102°	39.28	37.5	38.60	40.49	4.7%	4.9%

Table 5.3: Validation of FFT model against two operating points

Although an exact numerical replication of the FEA loss calculation is not possible by lumping the steel components with constant flux density, the trends are sufficiently captured. With an analytical model of the material losses, the full characteristics of the motor are outside of FEA and the switching angle optimization can be investigated.

5.2 Switching angle optimization

The performance of the machine is highly sensitive to the turn-on and turn-off angles set by the controller. Generally, the switching angles should be advanced as the speed increases, due to higher induced voltage, the current will take longer to reach desired target when switching on. Depending on the duration of the phase demagnetization, the phase must be turned off well before overlapped position otherwise risking negative torque. An initial sweep of the switching angle space is shown in Figures 5.7. It is clear that the torque quality is a tradeoff with torque and efficiency. It should also be noted that the optimal efficiency for this speed and current setpoint is not at the maximum torque.

5.2.1 Introduction to the Genetic Algorithm

The genetic algorithm is an optimization method that uses the principles of natural selection to find a minimum of a cost function. A population is first defined by evaluating the cost function for random values of its input parameters. The smallest (most fit) outputs survive the generation, and combine their input parameters to form "children". The children input parameters undergo a mutation, or a random adjustment in value. The process then repeats with a new population. In the case of motor control, the switching angles may be considered the input parameters, and the motor performance (or anti-performance) is the cost function. In the sections below, the AFSRM control parameters are optimized using the genetic algorithm in Matlab. For each operation point, a genetic algorithm of 5 generations,

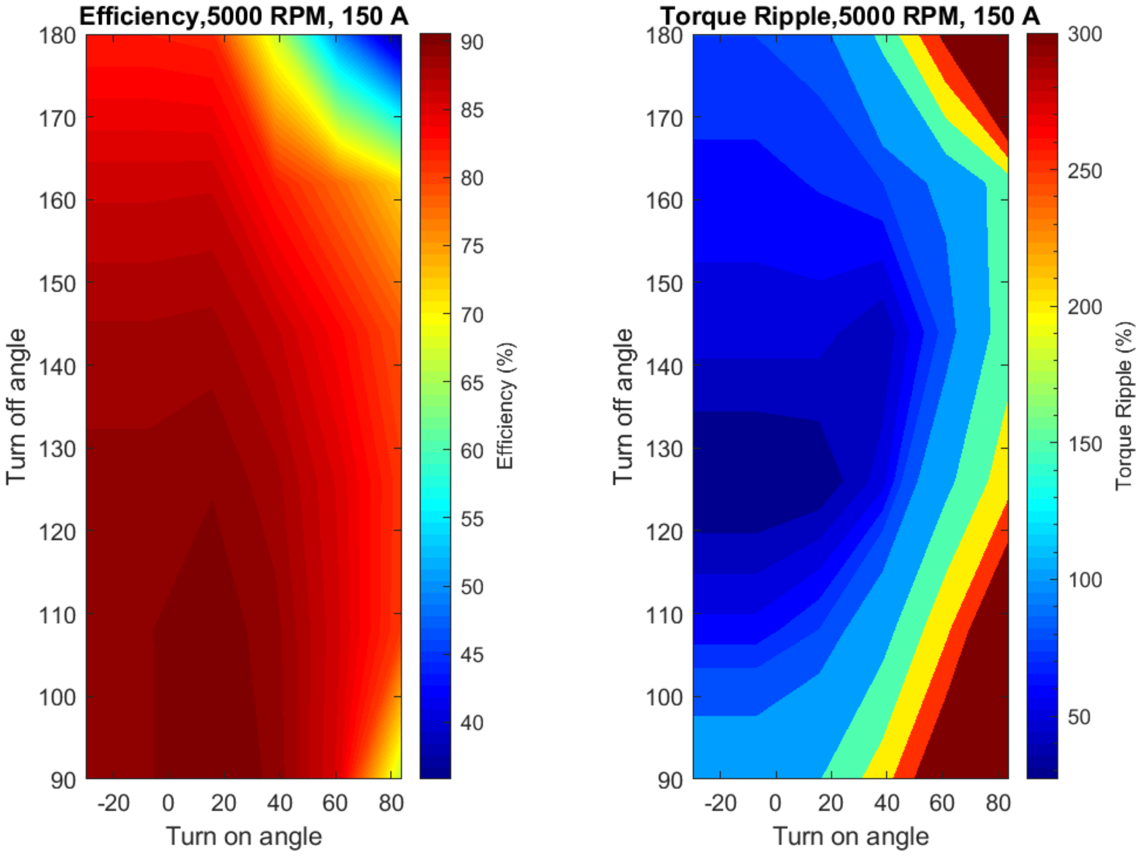

(A) Efficiency

(B) Torque Ripple

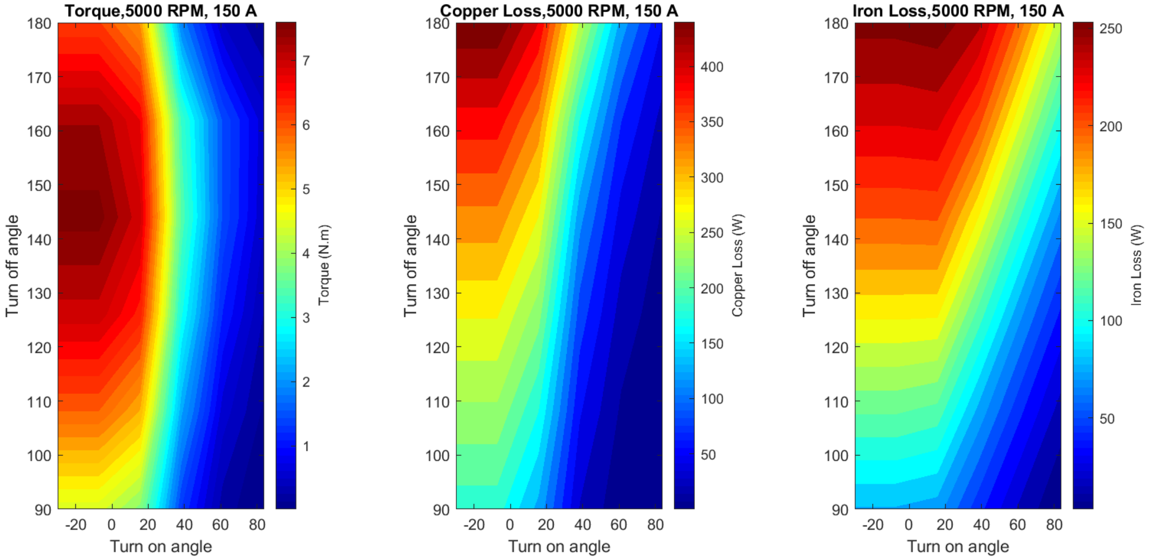

(C) Torque

(D) Copper Loss

(E) Iron Loss

FIGURE 5.7: Sweep of sweep of switching angles for $-5° < \theta_{\text{on}} < 14°$ and $15° < \theta_{\text{off}} < 30°$

with population of 25 per generation, is used to solve the best switching angles and target current for a given performance metric.

5.2.2 Torque Speed Curves with Optimized Switching Angles

Figures 5.8 and 5.9 below show the torque-speed and power-speed curves for 150A and 300A current setpoints with optimized conduction angles. These curves reflect operation with switching angles optimized for average torque production.

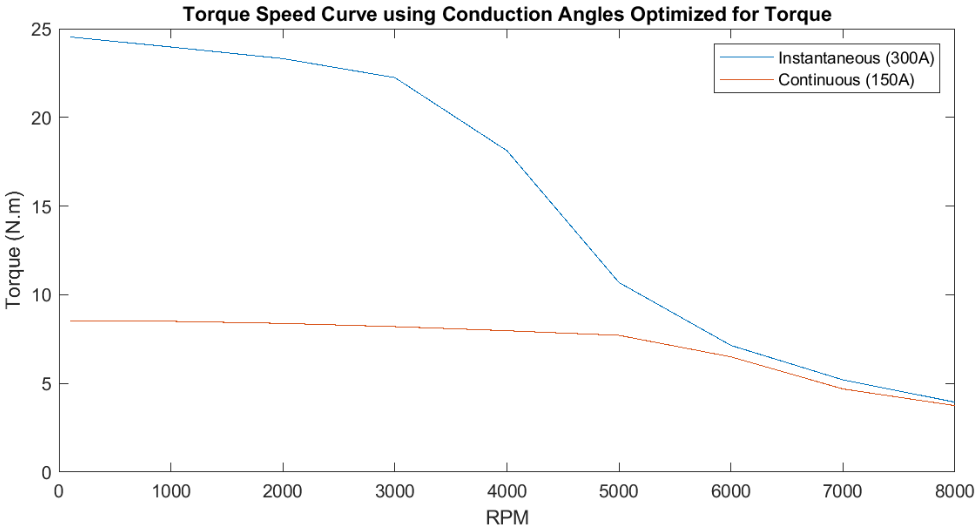

FIGURE 5.8: Torque speed curves for 150A and 300A setpoints with optimized conduction angles

With the optimizer set to value only average torque, and current setpoints fixed, the selected conduction angles result in the maximum achievable torque. It should be noted that the machine experiences a base speed of 5000 RPM at nominal current and 3000 RPM at peak current. While these curves establish a baseline for the machine's capabilities, more detailed analysis of torque ripple and efficiency are required to fully characterize the machine.

5.2.3 Optimization Setup

The conduction angle control of the AFSRM has three parameters at a given speed:

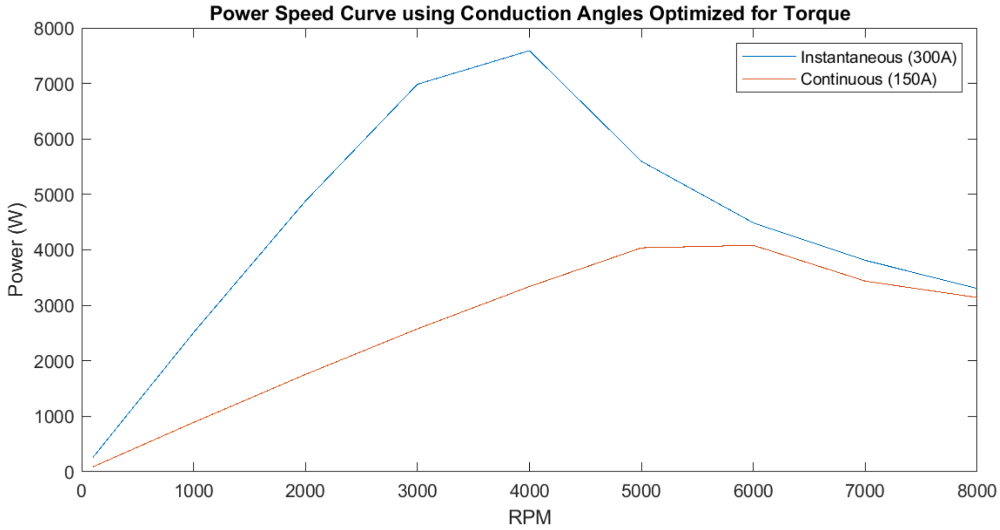

FIGURE 5.9: Power speed curves for 150A and 300A setpoints with optimized conduction angles

- Turn on angle θ_{on}
- Turn off angle θ_{off}
- Target phase current I_{targ}

For each combination of control parameters, a set of performance metrics exist, namely:

- Average Torque T_{ave}
- Efficiency η
- Torque Ripple t_{r}

An optimization routine may be defined for input parameters $[\theta_{\text{on}}, \theta_{\text{off}}, I_{\text{targ}}]$ and cost function f_{c} which is based on the performance metric of choice. The switching angles may be optimized over the entire operation range by defining a series of torque and speed setpoints with sizes N_{t} and N_{ω}. At any point on the torque-speed grid, the turn on and turn off angles may be found, for a total of $N_{\text{t}}N_{\omega}$ operating points. The maximum torque may be found by constraining the control to $I_{\text{targ}} = 300A$ and assigning full weight to average torque in the cost function. As the maximum torque $T_{300\mathrm{A}}$ at each speed is established, the remaining torque targets are defined by dividing the $\mathrm{T}_{300\mathrm{A}}$ into $N_{\mathrm{t}} - 1$ setpoints. In the interest of determining the limits of the performance trade-offs, the optimization is run for both best torque quality and best efficiency. To optimize the switching angles at each setpoint (whether an efficiency-based or torque ripple-based cost function is used), an additional term is added onto the cost function that penalizes deviation from the torque setpoint by calculating the torque error cost. This forces the optimizer to converge to the desired torque setpoint while also optimizing the performance metric. The torque error cost is defined as the square of the torque error divided by the error tolerance:

$$C_{\mathrm{torqueError}} = \left(\frac{\%error}{errorTol} \right)^2 \tag{5.9}$$

Where $errorTol$ is a small tolerance in torque error, such as 0.05. A visualization of the efficiency and torque ripple optimization can be seen in Figure 5.10. The red torque-speed curve is calculated by maximum torque at 300A, whereas the green torque-speed curves represent divisions below the maximum torque on which to optimize efficiency or torque quality. To mitigate the devaluing of the efficiency or torque ripple variables, a lower saturation limit of the torque error cost was set to 1.0. Thus, once the optimizer achieves a torque within 5% of the target, the cost of the efficiency or torque ripple are not neglected by a near-zero coefficient.

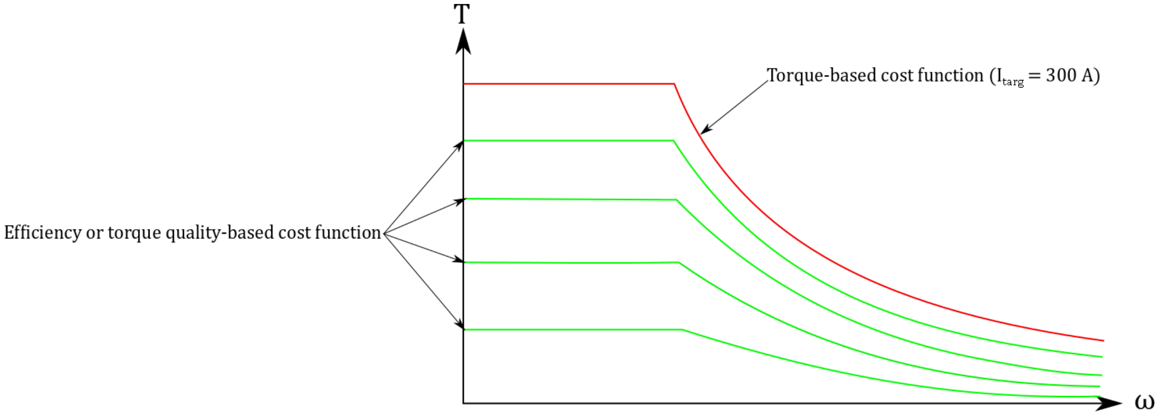

FIGURE 5.10: Segmentation of the torque-speed range for switching angle optimization

5.2.4 Machine Characteristics when Optimized for Maximum Efficiency

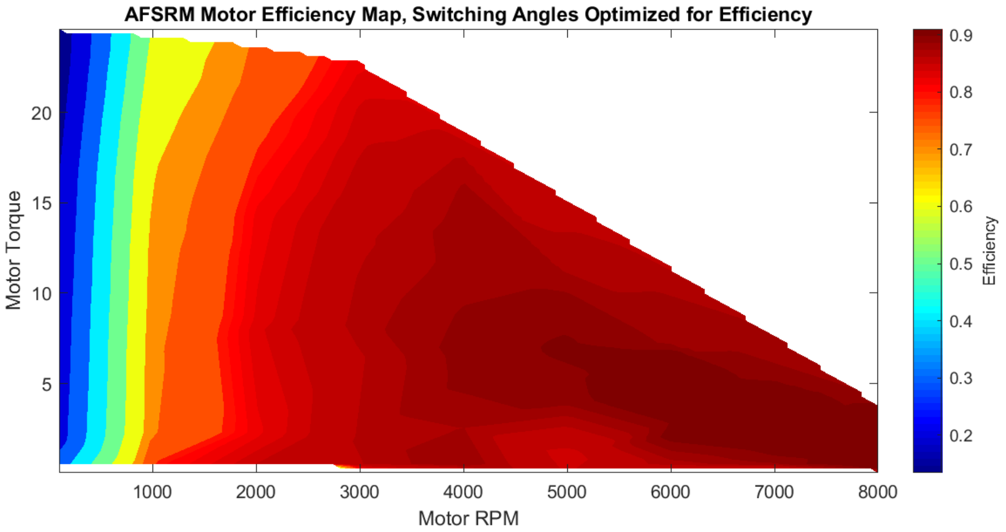

Figure 5.11: Efficiency Map using conduction angles optimized for maximum efficiency

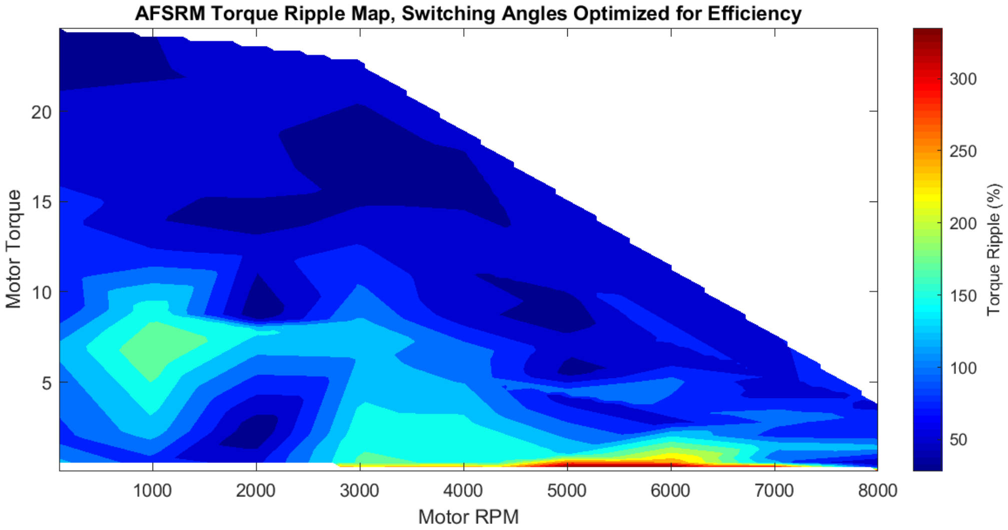

Figure 5.12: Torque ripple map using control optimized for maximum efficiency

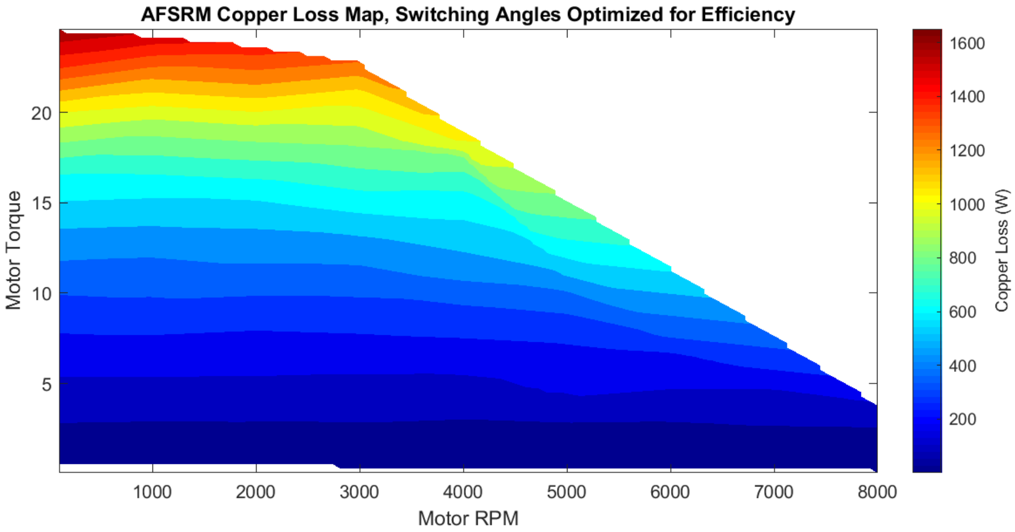

FIGURE 5.13: Torque ripple map using control optimized for maximum efficiency

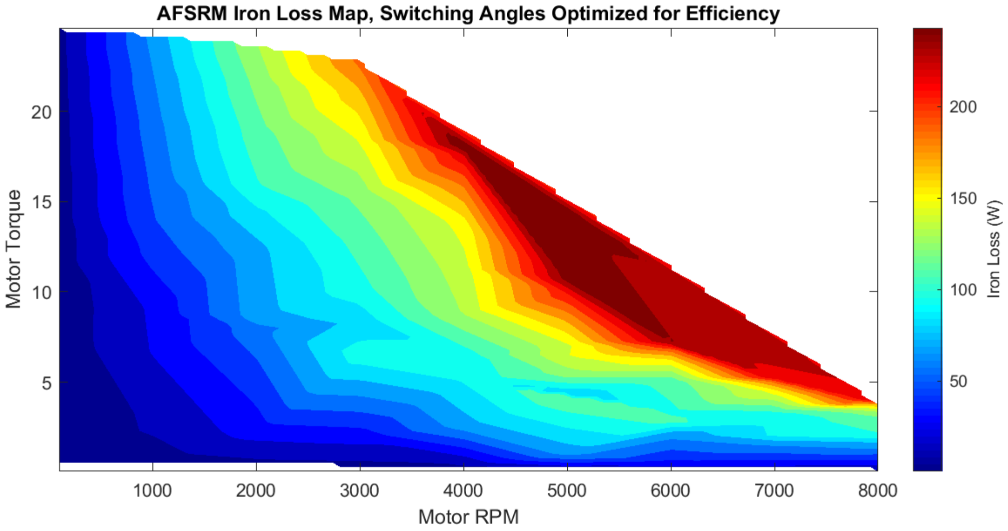

FIGURE 5.14: Iron loss map using control optimized for maximum efficiency

5.2.5 Machine Characteristics when Optimized for Torque Quality

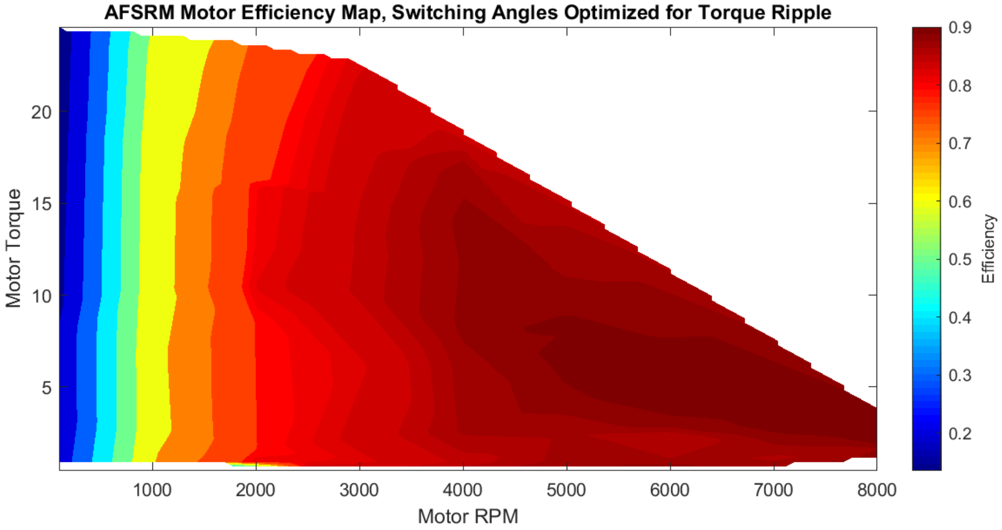

FIGURE 5.15: Efficiency Map using control optimized for minimum torque ripple

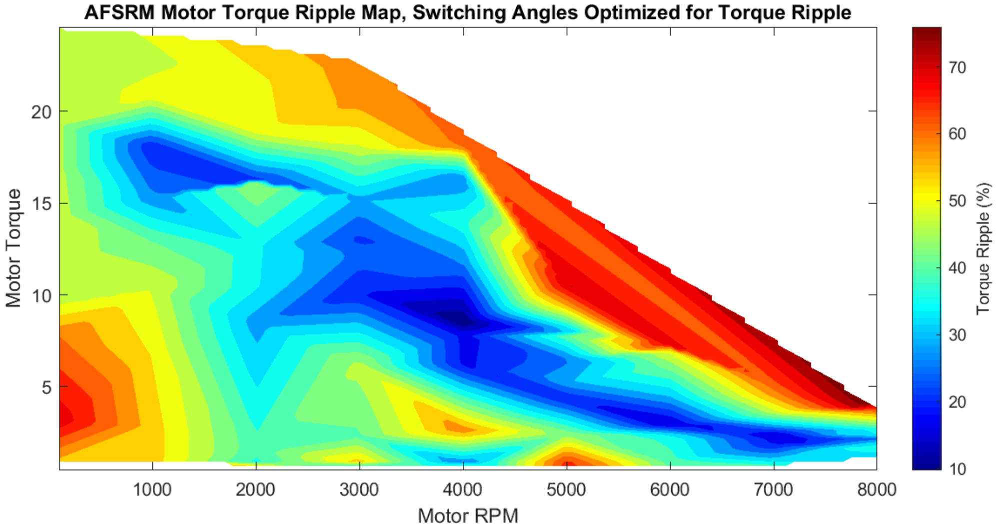

FIGURE 5.16: Torque Ripple Map using control optimized for minimum torque ripple

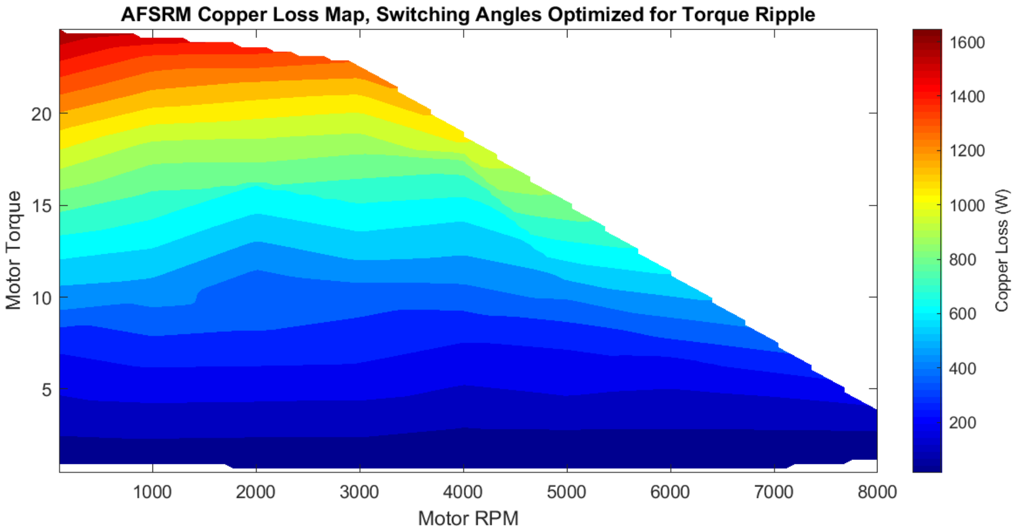

FIGURE 5.17: Copper loss map using control optimized for minimum torque ripple

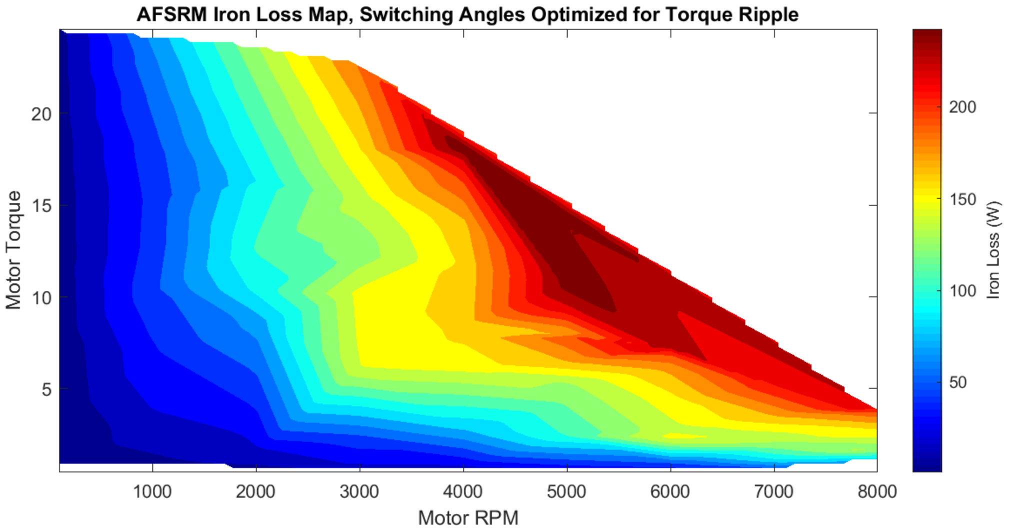

FIGURE 5.18: Iron loss map using control optimized for minimum torque ripple

5.2.6 Key Operating Points

Operating points at $4000RPM$, $8.5N.m$ and $6000RPM$, $3.5N.m$ are plotted below with control inputs optimized for either efficiency or torque quality.

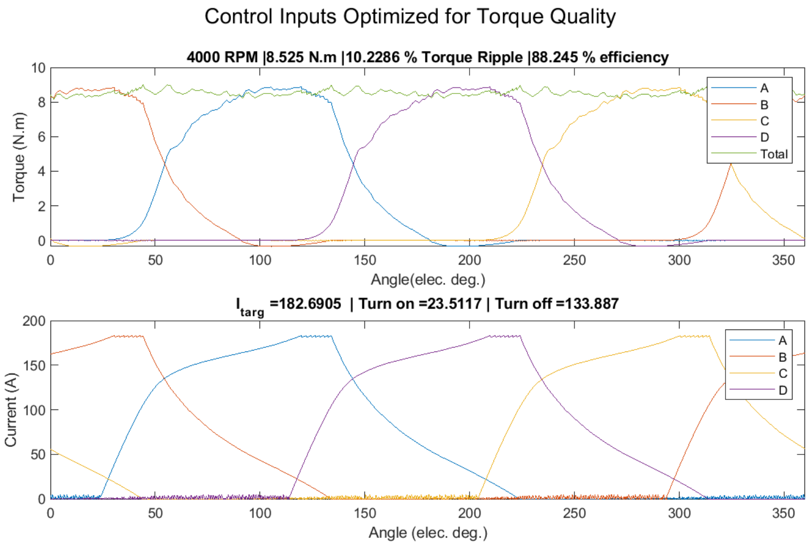

FIGURE 5.19: Operating point 1, best torque quality

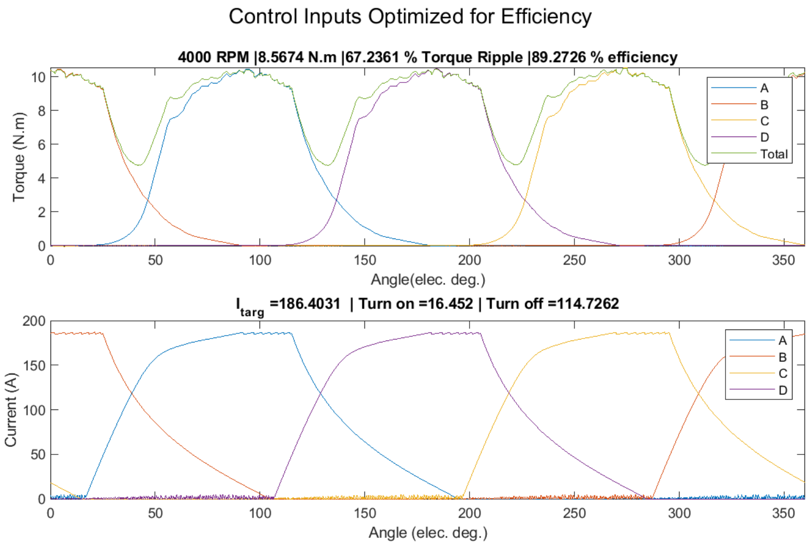

FIGURE 5.20: Operating point 1, best efficiency

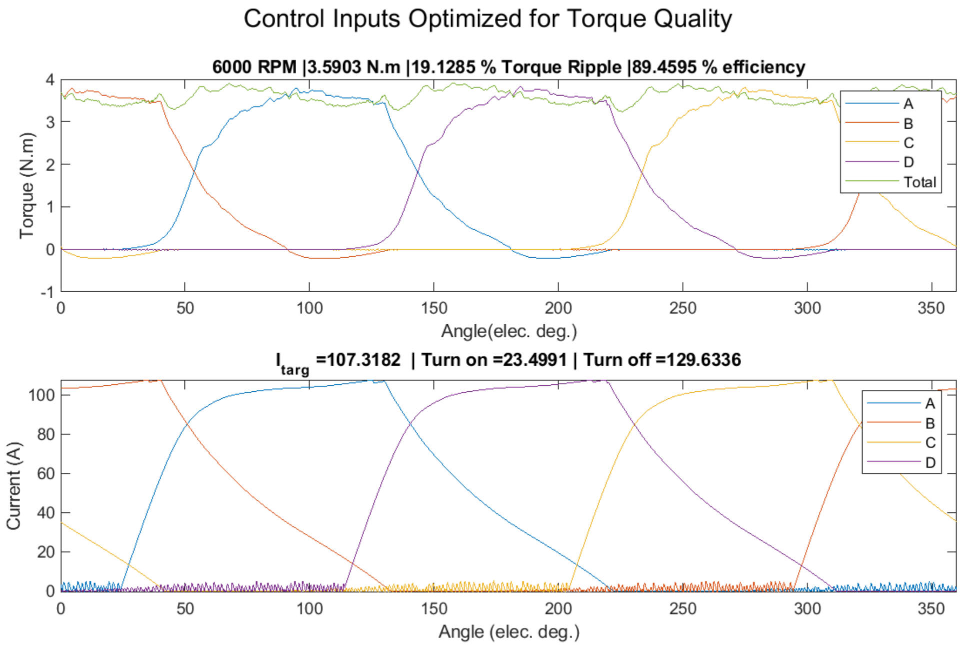

Figure 5.21: Operating point 2, best torque quality

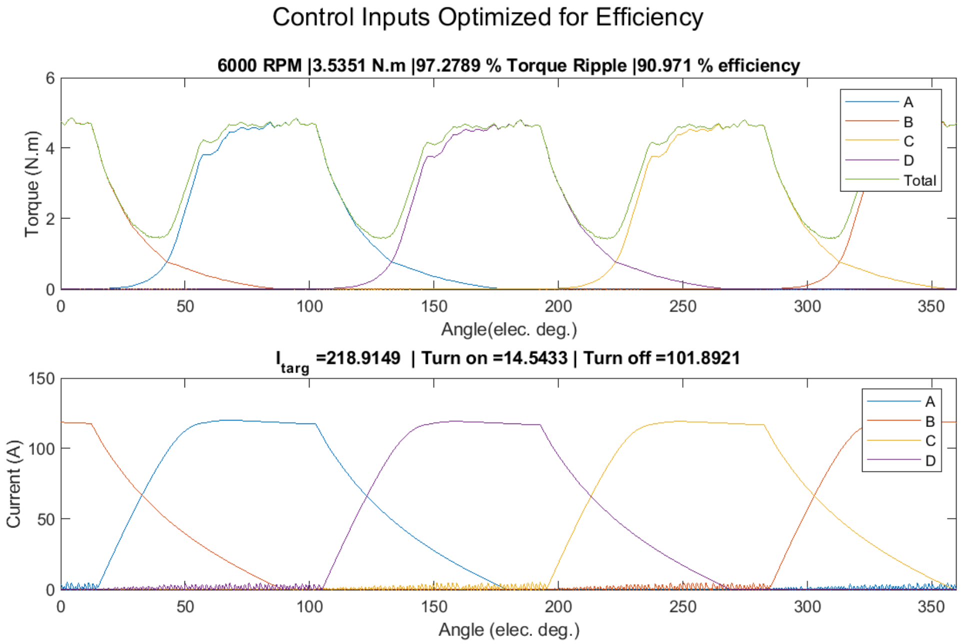

Figure 5.22: Operating point 2, best efficiency

A trade off between torque quality and efficiency is evident. Although operating for optimized efficiency gains 1-3%, torque ripple is shown to increase by 40-60%. While the difference in torque quality does suffer more in terms of value, the application would dictate what are appropriate weights to assign torque quality and efficiency. Additionally, while the increase in efficiency is small for the selected operating points, the different in net energy usage can be significant. This is illustrated in Figure 5.23 which is the energy usage of the motor for the drive cycle in Chapter 2, run for both optimized torque quality and optimized efficiency. Approximately 0.2 kWh is conserved by accepting poor torque quality.

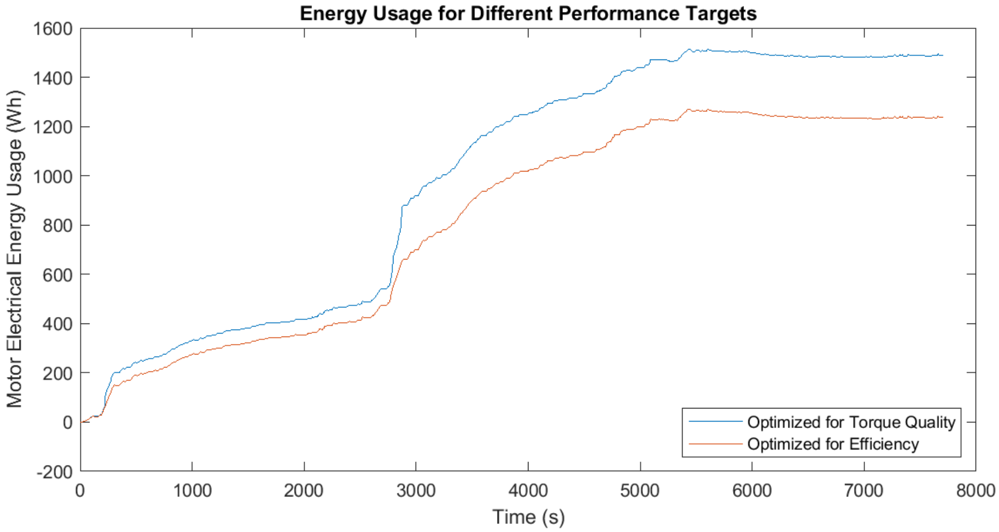

Figure 5.23: Electrical energy usage of the AFSRM for the LEV drive cycle from Chapter 2

5.3 Thermal analysis

The machine's continuous power capability will be determined by effective removal of heat. The thermal performance is especially critical for the stator, for several reasons. First, the rotor does not possess any temperature-sensitive parts due to the lack of permanent magnets. Secondly, the rotor poles are expected to exhibit excellent heat removal due to the surface area in contact with the aluminum yoke. Lastly, the stator is the source of high density copper losses, which threaten to damage the insulation or encapsulation material at high temperatures. The copper loss heat removal can be summarized by two main mechanisms:

- Convective heat transfer in the airgap
- Conductive heat transfer to the casing, resulting in convective heat transfer from the mounting structure.

A small quantity of heat will pass through the ball bearings to the rotor, which is assumed to operate much cooler. The heat relies on a small contact patch between the bearing race and the ball bearing, which is improved by thrust loads. A study by Jin et al [61] predicts the thermal resistance of a similar sized bearing to be approximately $50K/W$.

5.3.1 Airgap Convection

The main mechanism of heat removal for the AFSRM is through airflow in the airgap. The convection heat transfer coefficient h_{c} is given by [62]:

$$h = \frac{k_{\mathrm{air}} Nu}{r} \tag{5.10}$$

where k_{air} is the thermal conductivity of the air, r is the machine radius, and Nu is the Nusslet number, which is the ratio of convective heat transfer and depends on the flow characteristics. The Nusslet number for a disc airgap follows the general form:

$$Nu = C_1 Re^{\mathrm{C}_2} \tag{5.11}$$

where C_1 and C_2 are fit parameters. In [63], Howey showed that in the turbulent region, C_1 increases drastically as the airgap ratio $\frac{g}{R}$ decreases while C_2 exhibits a weak positive correlation. This was achieved through measurement of a mock-AFPM rotor on a flat stator with 3.5° gaps between magnet protrusions. Using a gap ratio of 0.003, Howey's measurements of A and B can be extrapolated with a linear approximation:

$$Nu = 0.0803 Re^{0.6354} \tag{5.12}$$

The flow is classified by the Reynold's number, which is an indication of the flow turbulence. The Reynold's number for an airgap between rotating coaxial disks is given from:

$$Re_\theta = \frac{\omega R^2}{v} \tag{5.13}$$

where ω, R, v are the machine angular velocity, outer radius and the air kinematic viscosity, respectively. The estimated airgap convection coefficient is plotted in Figure 5.24. It should be noted that this flow model is determined by extrapolation of experimental results, and is heavily dependent on the surface features and inlet locations. The AFSRM rotor has relatively larger protrusions at a larger spacing, which is expected to increase the turbulent behaviour of the airflow in the airgap increasing the effective convection coefficient. Therefore, this model is considered a "worst-case" cooling scenario.

5.3.2 Finite Element Thermal Model

The stator thermal model may be reduced to $1/16$th using assumptions of symmetry. Firstly, it is assumed that on average, no heat transfer will occur between stator poles due to equal

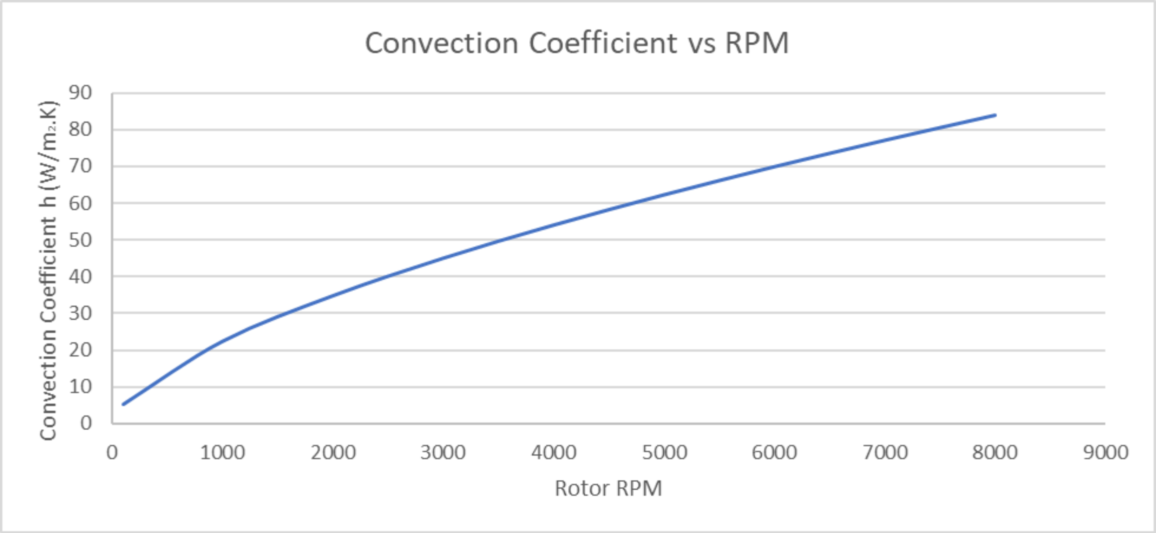

FIGURE 5.24: Estimation of airgap convection coefficient for AFSRM speed range

losses and equal heat removal due to symmetry. Secondly, no heat flux will pass through the mid-plane due to the stator pole symmetry. This transformation is shown in Figure 5.25 .The structure is modeled bolted to a 12.5mm thick, 430mm diameter aluminum plate, similar to what will be used for testing. A 1/32nd model is possible by considering the plane between airgaps as a symmetry plane as well, however this would negate the asymmetry of the mounting tab.

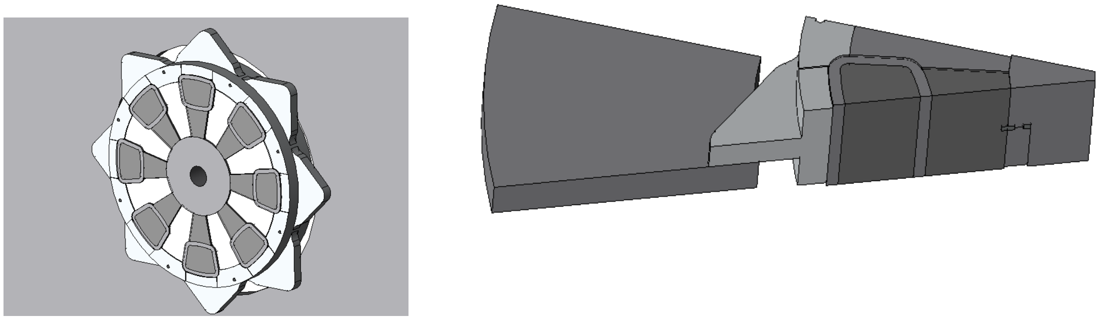

(A) Full model

(B) 1/16th model with symmetry

FIGURE 5.25: Symmetrical reduction of stator thermal model

5.3.3 Lumped Parameter Thermal Model

While an FEA model is sufficient for understanding the temperature distribution in the components, it is too cumbersome for implementation over a drive cycle. A lumped-parameter thermal model (LPTM) can be solved with much less computational effort. The LPTM uses an electric circuit analogy to represent heat transfer in the stator. Conduction and convection phenomena may be represented by thermal resistances, heat capacity may be represented by capacitance and generated heat by a current source. A LPTM was built in the Simulink Simscape environment using material properties and dimensions of the stator. An overlay of the LPTM with a generalized stator geometry is shown in Figure 5.26.

Thermal resistances of the LPTM depend on the segmentation of the geometry into elements of a representative length with an approximate cross sectional area. The stator winding is segmented into a lumped copper element, a lumped insulation element and a mainwall insulation element, each defined with the thickness of the total number of layers for each material. Similarly, thermal elements are arranged to contact a central node in the part, with the length and cross sectional area defined as the face area from the adjacent part and length to centroid.

The validity of the LPTM can be assessed by comparing the the FEA model under various conditions. A good match would indicate sufficient approximation of the geometry into thermal elements, however validity to a prototype depends on the material properties and quality of bonds between components. A number of thermal cases were chosen for comparison between the LPTM and FEA models. The conditions are listed in Table 5.4. Figure 5.27 shows the LPTM temperatures plotted alongside the winding temperatures from FEA.

Loss Condition	Copper Loss	Stator Iron Loss	RPM
1	300 W	150 W	100, 1000, 3000, 4000, 8000 RPM
6	500W	50W	100, 1000, 3000, 4000, 8000 RPM

Table 5.4: Thermal conditions for comparing LPTM and FEA

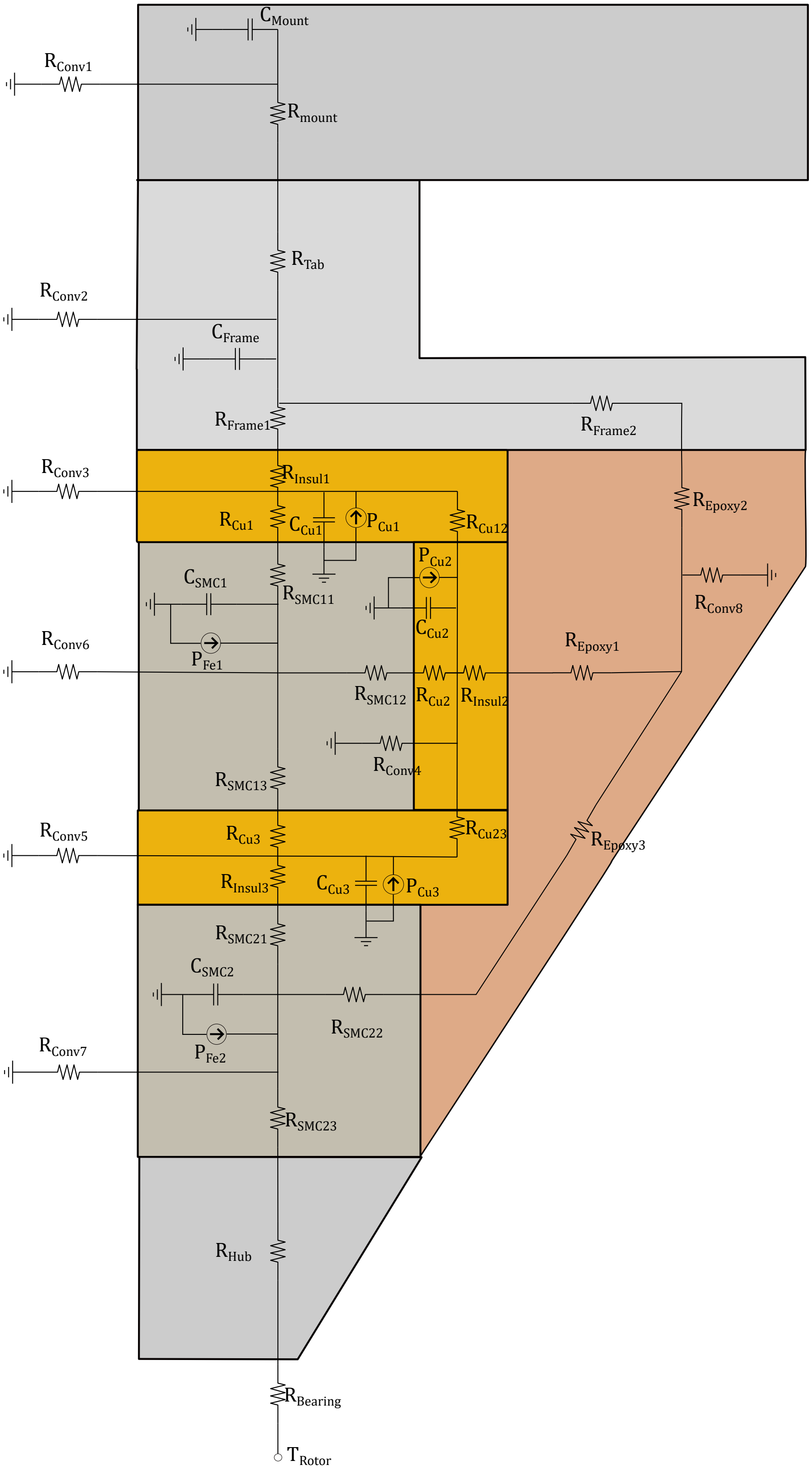

FIGURE 5.26: LPTM

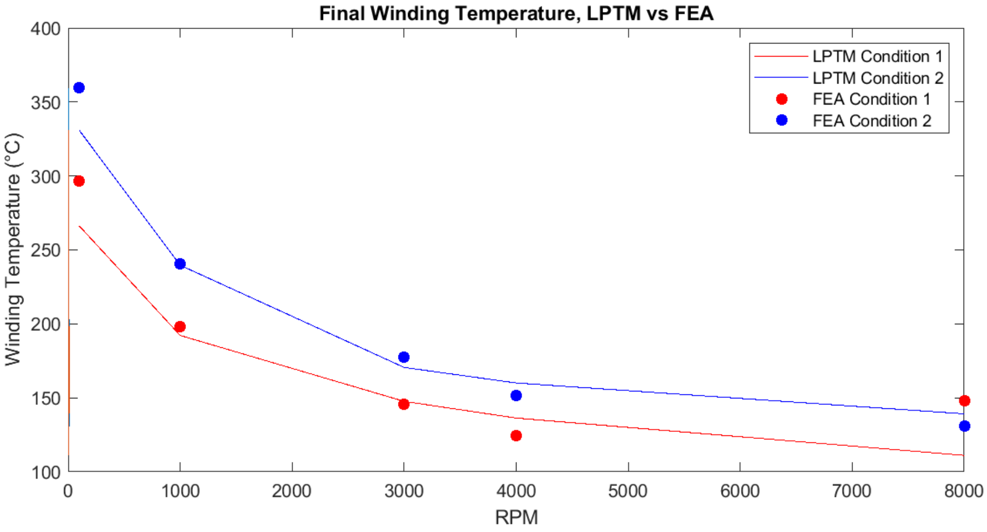

FIGURE 5.27: Comparison of final winding temperatures for FEA and LPTM

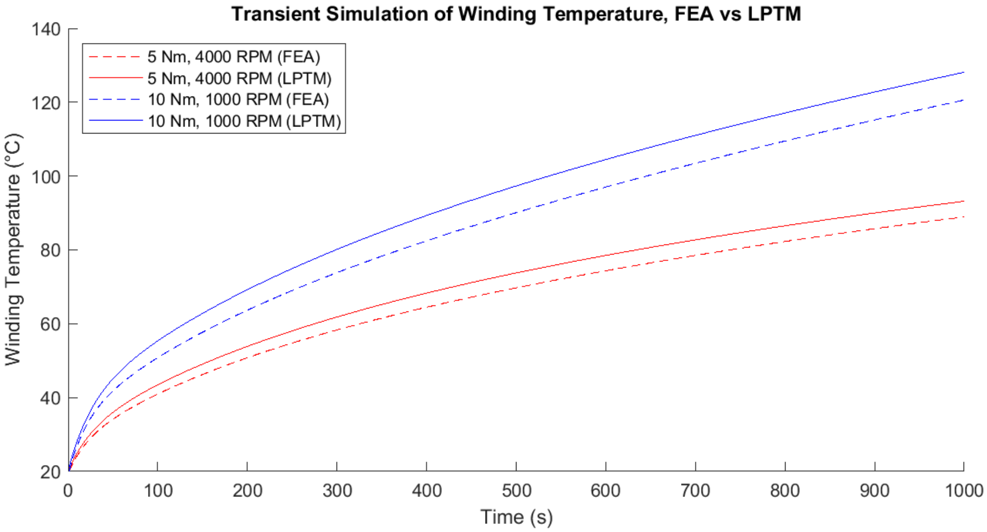

FIGURE 5.28: Transient winding temperature for two operating conditions with LPTM and FEA

With the LPTM established as a good approximation to the stator geometry, an evaluation of the thermal performance over the torque-speed curve is possible. Using the loss data from Figures 5.18 and 5.17, lookup tables were defined to return the scaled heat production for both stator winding and core based on operating point. A map of final temperatures is shown in Figure 5.29.

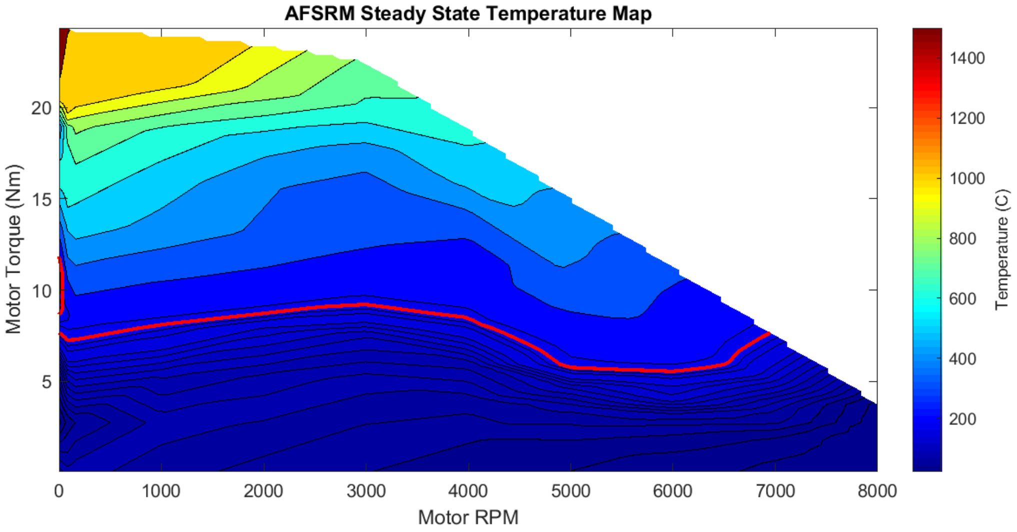

FIGURE 5.29: Steady state winding temperature map with 180°C line marked in red

High temperatures are observed at steady state for operating points outside of 8 N.m, however the short-term capability is not reflected with steady-state temperatures. The transient performance of the AFSRM can be better understood by mapping length of time that an operating point can be sustained, shown in Figure 5.30. It is evident that intermittent performance is possible for extended periods of operation due to the large thermal mass in the stator, for example operation at 200% continuous torque is possible for up to 10 minutes.

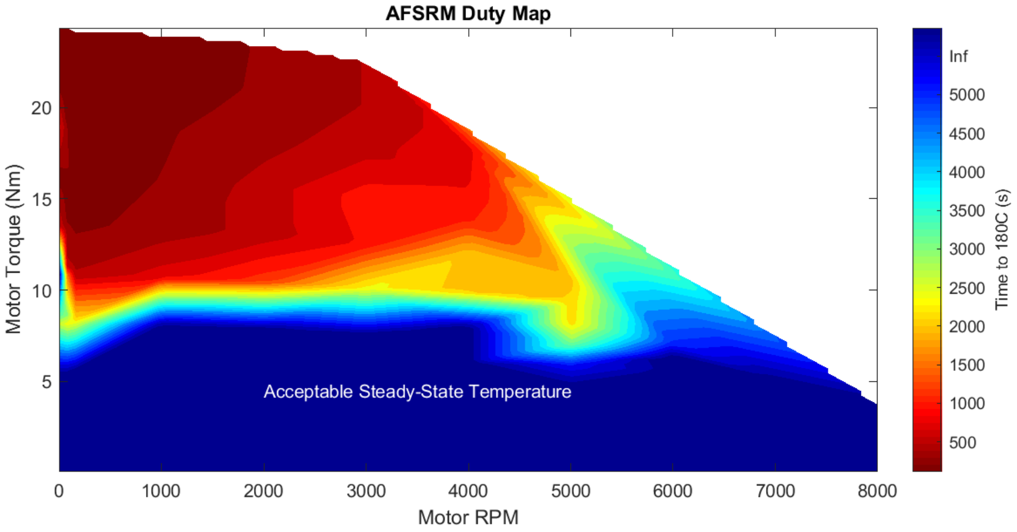

FIGURE 5.30: Time for winding to reach 180°C from 20°C

With a full thermal characterization, the motor can be evaluated in terms of power per unit mass. Table 5.5 below lists several performance ratings that may be used to benchmark the machine against others:

Rating	Value	Unit
Continuous Power	4.76	kW
Peak Power	7.12	kW
Continuous Specific Power (active mass)	0.61	kW/kg
Peak Specific Power (active mass)	0.91	kW/kg
Continuous Specific Power (full mass)	0.33	kW/kg
Peak Specific Power (full mass)	0.49	kW/kg

TABLE 5.5: Power ratings of the AFSRM

The motor performance in the LEV application can be evaluated with the target drive cycle. Lookup tables for stator losses are used to relate motor operating point to heat generation. A scaling factor based on the temperature coefficient of copper resistivity was applied to scale the copper losses according to the operating temperature. A plot of winding temperature over the drive cycle from Figure 2.6 is shown in Figure 5.31.

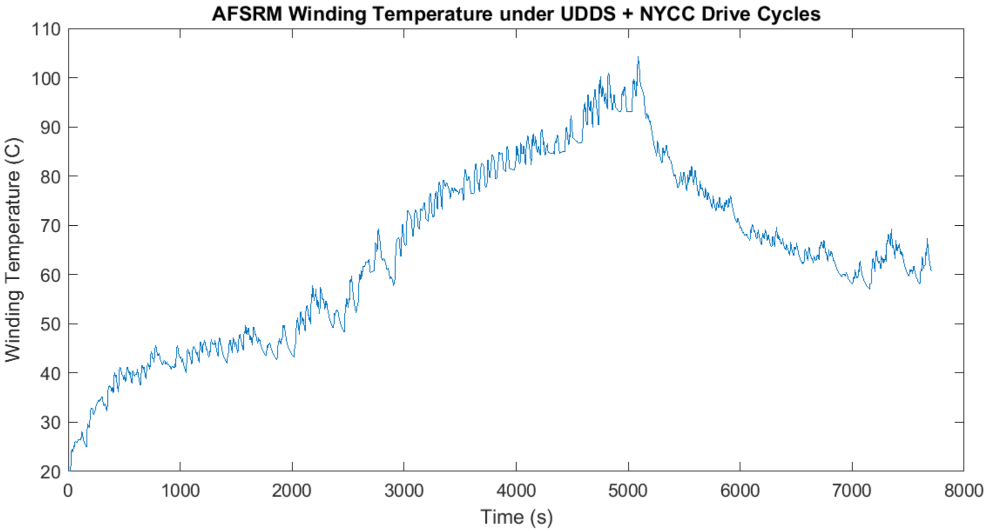

FIGURE 5.31: Winding temperature for UDDS + NYCC drive cycles

The temperature rise over the drive cycle is seen to peak at 105° C during the end of the inclined drive cycle segment, and fall during the decline segment to a final temperature of 66°C.

5.4 Summary

In this chapter, the numerical AFSRM model was expanded to include a calculation of iron loss. The iron loss model enabled fast calculation of the AFSRM efficiency, which is necessary for switching angle optimization. A map of switching angles was generated for both optimal efficiency and optimal torque quality, and the performance difference over a drive cycle was simulated. Finally, the continuous and instantaneous power limitations were determined through a LPTM and the temperature rise was predicted over the drive cycle.

Chapter 6

Prototyping of the AFSRM

This chapter will document the prototyping of the AFSRM. A combination of off-the-shelf and fabricated components make up the assembly. A bill of materials of the fabricated components is shown below in Table 6.1.

Part	Quantity	Manufacturing Strategy
Outer Stator Pole	8	Machine on CNC mill from pre-sintered SMC blank
Inner Stator Pole	8	Machine on CNC mill from pre-sintered SMC blank
Stator Winding	8	Wind directly on outer pole on lathe
Stator Spine	1	Waterjet cut 14 Ga stainless steel by vendor (Vykan Inc)
Stator rim	1	CNC mill from aluminum billet by vendor (Advantage Machining Inc.)
Stator hub	1	CNC Lathe + Mill from aluminum bar stock by vendor (Advantage Machining Inc.)
Rotor Yoke	2	CNC Mill from aluminum billet by vendor (Merq Inc)
Rotor Retaining Ring	2	CNC mill from 0.24" CFRP plate by vendor (Merq Inc)
Rotor Pole	12	CNC mill from pre-sintered SMC blank by vendor (PMG Fussen GmbH)
Shaft	1	Stainless steel bar stock turned and threaded on manual mill by vendor (Advantage Machining Inc.)

Table 6.1: AFSRM Bill of Materials and procurement strategy

6.1 Machined Stator Components

The central hub and outer ring were machined by Advantage Machining Ltd, pictured below.

Figure 6.1: Central hub

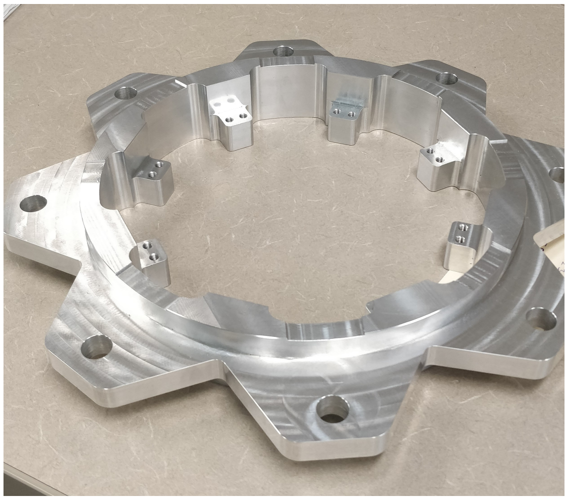

Figure 6.2: Outer ring

6.2 Stator Pole Machining

A number of machining recommendations should be followed with SMC. High brittleness will make machining operations susceptible to breakage, which may be mitigated by using climb milling instead of conventional milling [64]. The material removal should always be away from final part surfaces, for example drilling through the stock should be accomplished by drilling halfway through then completing the hole from the other side. Tools must be sharp and modified to decrease the length of the cutting surface.

The stator poles are machined from Hoganas SPM blanks, 40mm height, 8mm diameter. The profiles of three poles are first milled into the surface at 12mm depth. The poles are separated with a bandsaw and re-inserted to a set of custom jaws. The profile was then machined on the remaining 28mm height.

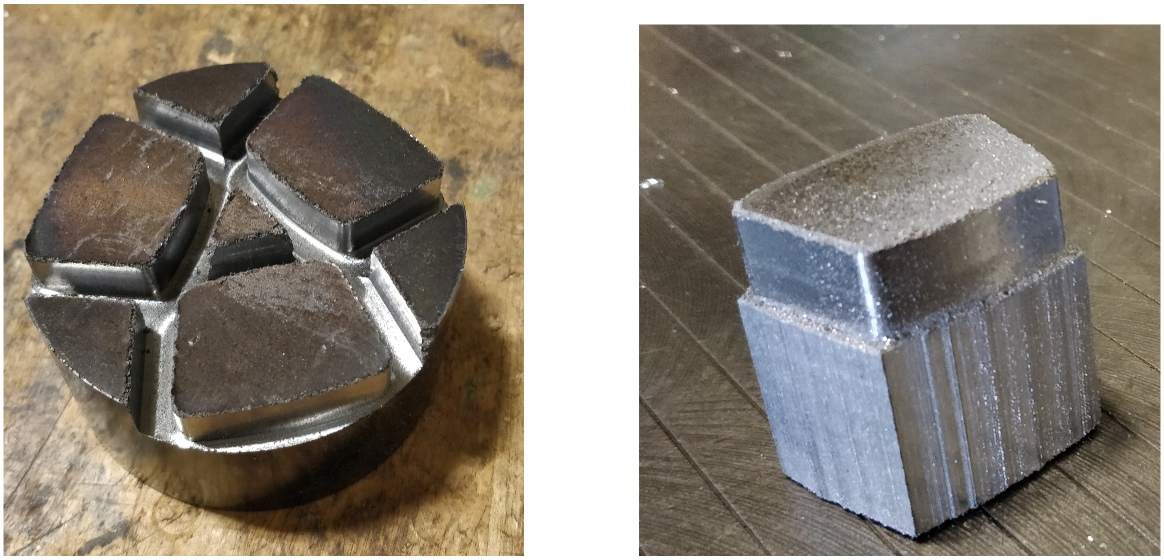

(A) Profiles cut at 12mm depth

(B) Poles separated with bandsaw

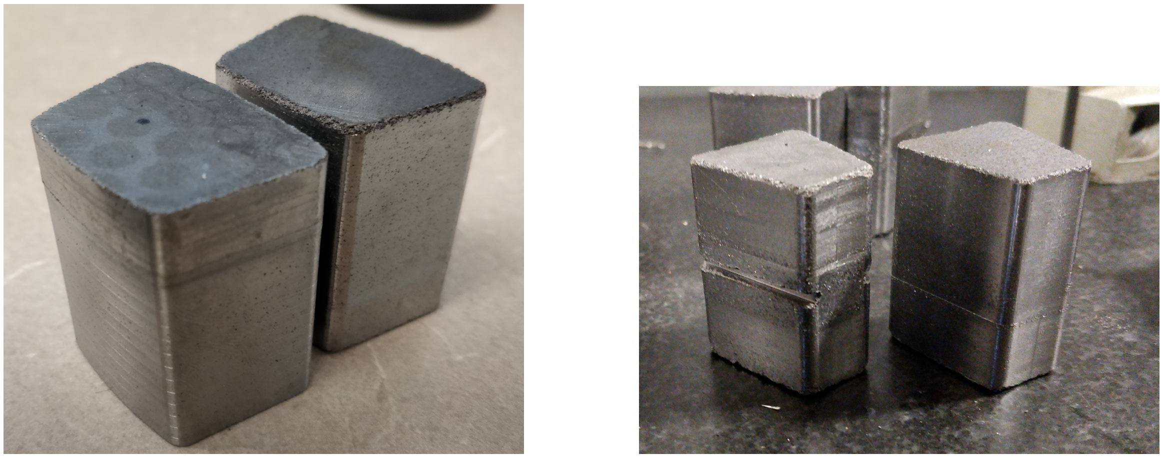

(C) Outer pole

(D) Inner pole

Figure 6.3: Stator pole machining

The edge quality is highly sensitive to the sharpness of the tool. In Figure 6.3c, the first pole to be machined (left) is pictured with the final pole (right). It is apparent that the sharpness of the tool degraded over the course of the machining. The result is an approximate

1 mm x 1 mm chamfer across all edges. Additionally the sharp corners on the inner pole had to be rounded to avoid breakage. The as-machined geometry was re-analyzed in JMAG to observe the effect on the static torque characteristics, shown in Figure 6.4.

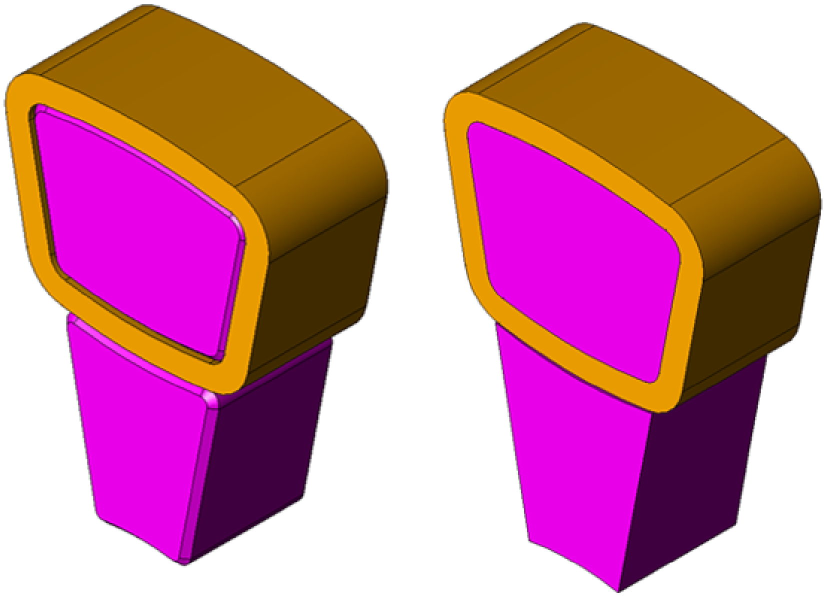

(A) Chamfered edges and rounded corners on stator iron

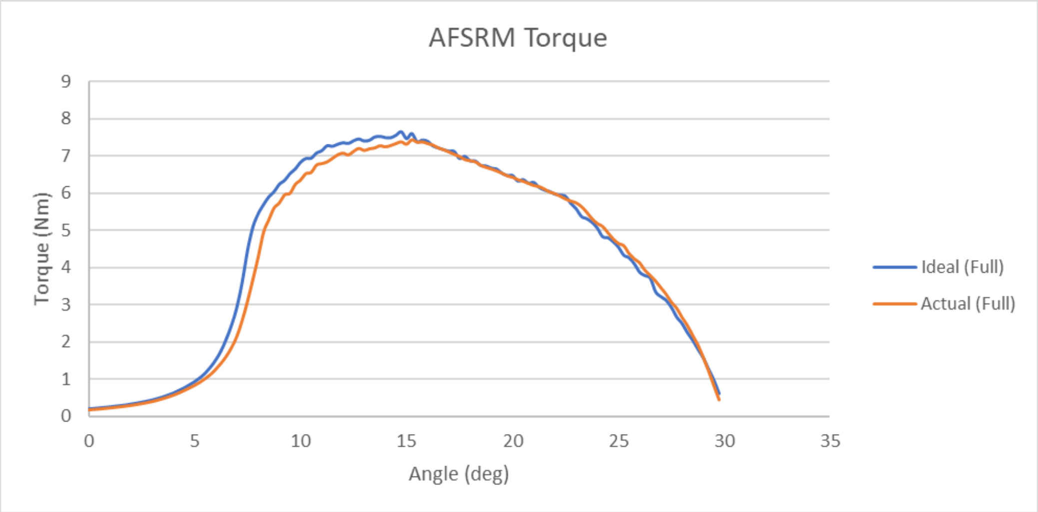

(B) Static torque effects

Figure 6.4: Effect of poor edge quality calculated by FEA

6.3 Stator Winding

The success of the winding process depends on the alignment of the foil and insulation layers. The insulation paper should protrude between layers of conductor, otherwise a turn-turn short circuit is possible. The widths of the winding components are listed in Table 6.2.

Coil Component	Width	Tolerance
Pole	40 mm	+/- 0.1 mm
Foil	38.1 mm	+/- 0.25 mm
Insulation Paper	40 mm	+ 1mm

TABLE 6.2: Winding component widths

If centered, the winding should sit with 0.95mm on either side of the pole. However, the windings were wound shifted to one side, to allow more clearance on the other side for machining down the airgap face. The desired placement of conductor on the pole is instead 1.4mm from one side and 0.5 mm from the other. A three-piece guideway was machined to allow the accurate layering of the foil and insulation. The guideway has slots machined for the foil and insulation, shown in Figure 6.5. The quality of the winding is dependent on the inner-most turn of foil, which must not create any bumps that could cascade into larget defects as the coil is wound. Folding the foil to a 90° bend produced poor quality of

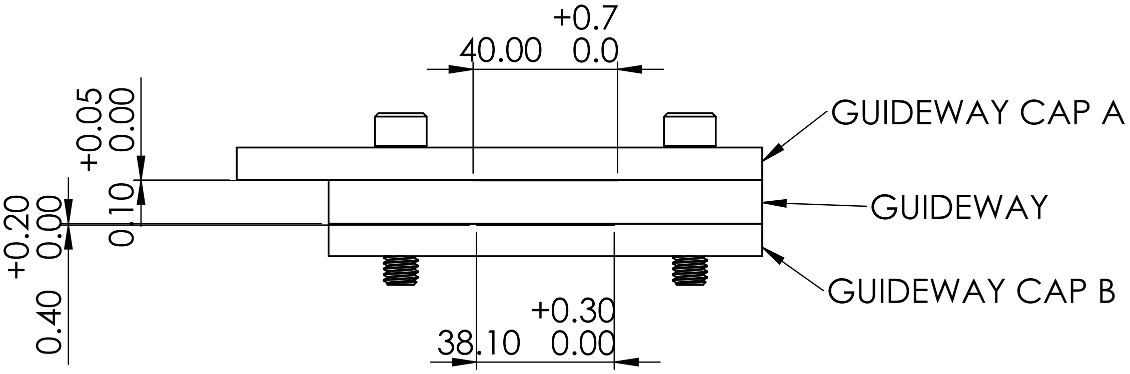

FIGURE 6.5: Drawing of guideway assembly

the inner-most turn, therefore a soldered joint was selected for the winding. The winding process can be summarized in the following steps:

- Cut a 2.0 m length of foil, solder the 90° lap joint to a 15 cm length
- Apply polyimide tape to both sides of the soldered joint and the entirety of the 15cm tab. (Figure 6.6a)
- Wrap the stator pole in double-sided polyimide tape, trim edges of tape flush to pole surface (Figure 6.6b)
- On the lathe, mount the pole to aluminum disk mounts in the lathe using glue (Figure 6.6c)
- Remove the release liner from the outside of the polyimide tape, exposing the adhesive. Press on thermocouple(s) and cover with additional double sided polyimide tape. Secure the remaining thermocouple(s) length to the lathe chuck
- Place the foil and insulation inside of the guideway, press foil onto adhesive tape on top of pole
- Align lathe Z-axis to allow for perpendicular winding onto the pole. (Figure 6.6d)
- Wind 16 turns by rotating lathe chuck and applying tension to foil-insulation combination
- Securing the winding with, remove and place into lower coil mold. Fold the outer tab to 90° joint centered on top of the coil.
- Wrap the coil in polyimide tape and secure mold together (Figure 6.6e)
- Remove the pole from glued mount by applying heat to the back of the mount (Figure 6.6f)
- Compress winding by fastening top half of mold to lower half, bake at 180°C for 45 minutes

The ends of the windings are brushed with 4 coats of varnish (Sterling 77X-101, ElantasPDG Inc, St Louis, USA) and the paper is trimmed down with a knife. The assembled stator is shown in Figure 6.8.

Coil inductance and resistance can be a good indicator of defects. The windings were measured with a Hioki RM3548 milliohmmeter and a B&K Precision 889B LCR meter, the results are tabulated in Table 6.3.

Coil	Resistance ($m\Omega$)	Inductance @ 120 Hz, 10 mV(uH))
A1	5.18	22.0
B1	5.040	21.62
C1	5.011	22.6
D1	5.018	21.95
A2	5.010	21.81
B2	5.101	21.62
C2	5.174	22.0
D2	5.12	22.0

Table 6.3: Winding resistance and inductance

It is clear that the inductance and resistance measurements are close, but it is not immediately apparent how close the measurements would be if one turn was shorted. A shorted turn create two effective turns in parallel when they should be in series, which would result in a different measured resistance according to:

$$R_{\text{shorted}} = \frac{15.5}{16} R_{\text{ideal}} = 0.96875 R_{\text{ideal}} \tag{6.1}$$

However the inductance would see a significant change due to the N^2 term:

$$L = \frac{N^2}{\mathscr{R}}, L_{\text{shorted}} = \frac{15^2}{16^2} L_{\text{ideal}} = 0.8789 L_{\text{ideal}} \tag{6.2}$$

Which is 19.3 μH if the average inductance is taken as a baseline. Therefore, it is assumed no turns have been shorted together.

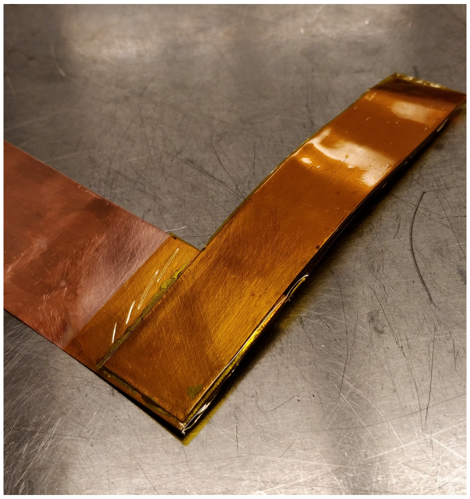

(A) Foil soldered to 90° joint

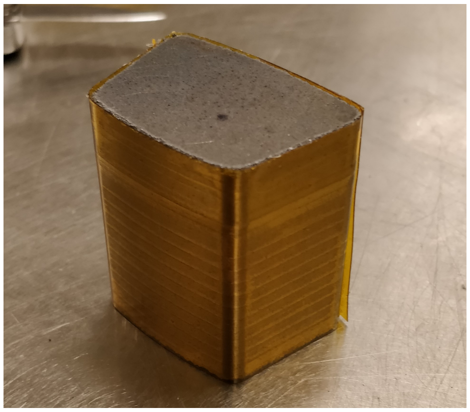

(B) Taped pole

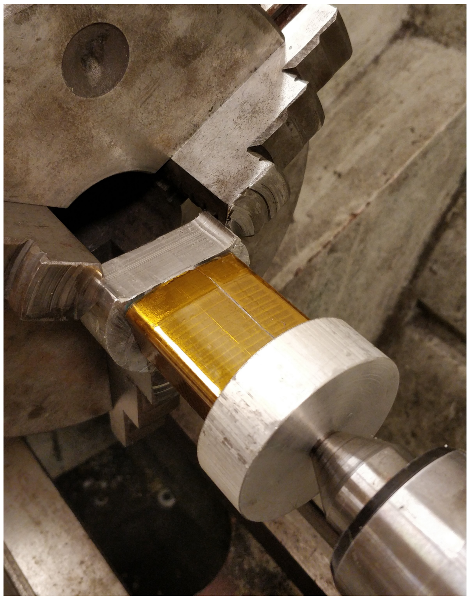

(C) Taped pole mounted on lathe jig

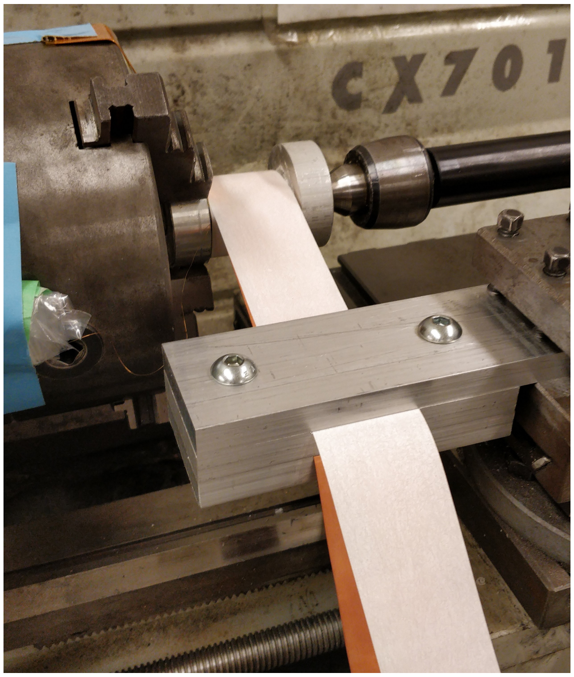

(D) Foil and insulation guideway mounted in tool post

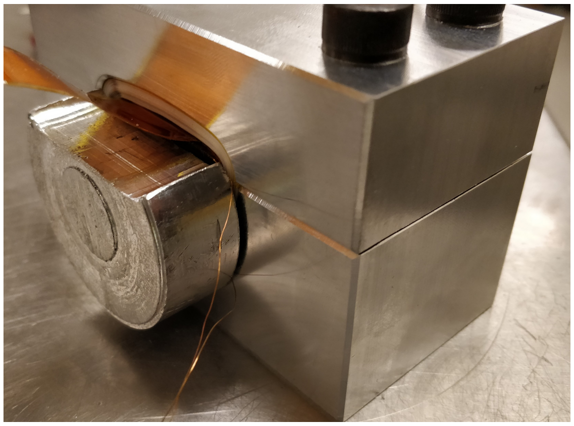

(E) Winding in mold with lathe mount still fixed

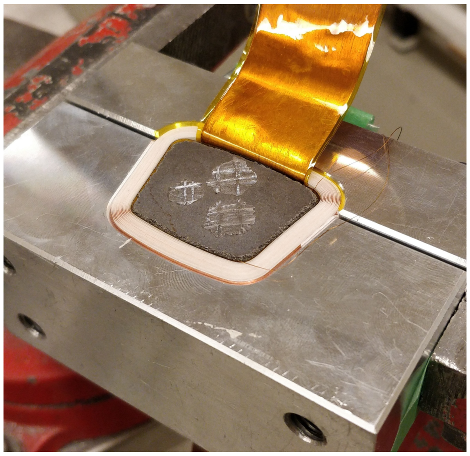

(F) Winding in mold with mount removed after heating

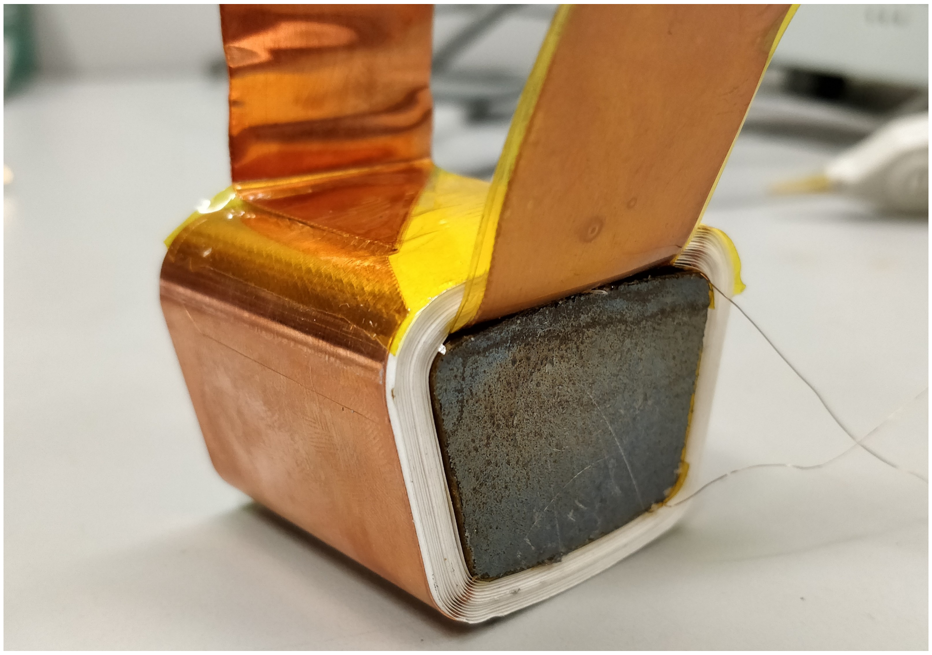

Figure 6.7: Completed winding on pole

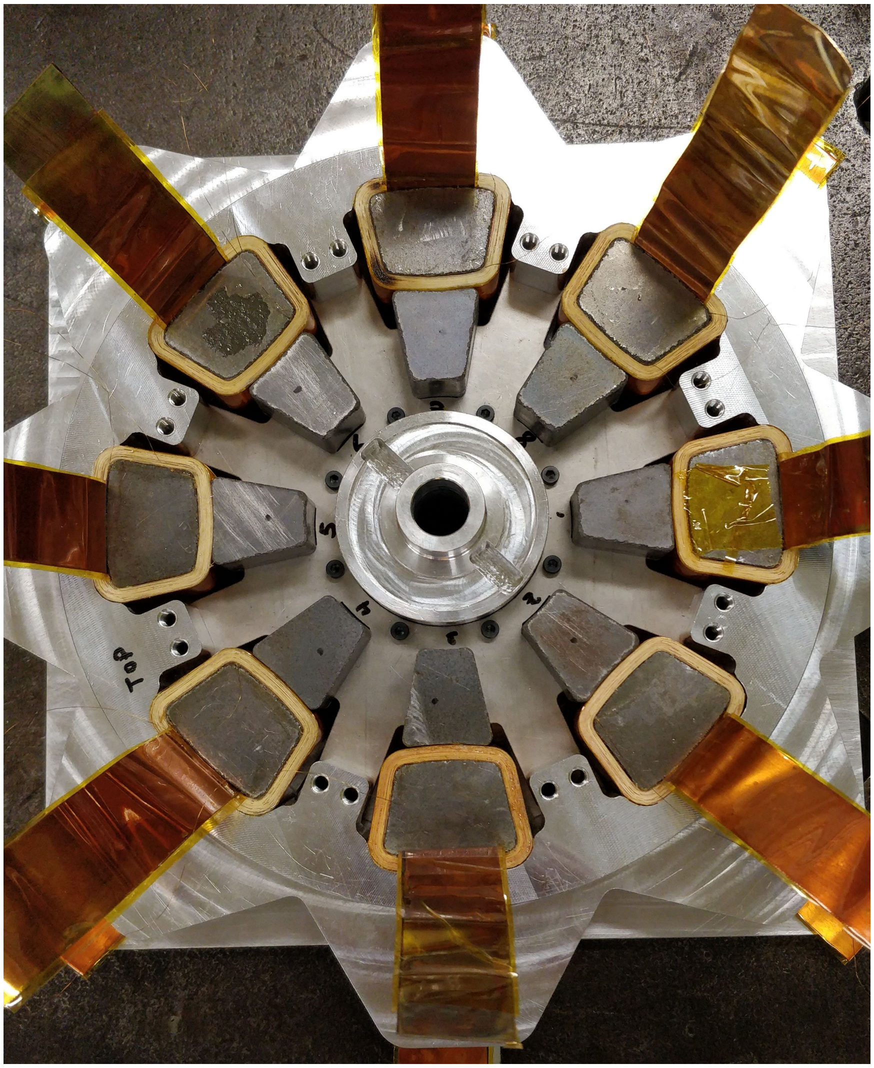

Figure 6.8: Assembled stator

6.3.1 Stator Coil Energizing

Before the coils can be accepted for encapsulation inside the stator, they should be energized under full load current. The RMS current must be considered due to the duty cycle of the phase currents. Assuming minimal overlap between the commutation of the 4 phases, the RMS current is given as:

$$I_{\text{RMS}} = I_{\text{targ}}\sqrt{0.25} = I_{\text{targ}} * 0.5 \tag{6.3}$$

This gives the continuous RMS current as $I_{\text{cont,RMS}} = 75A$ and the instantaneous RMS current as $I_{\text{inst,RMS}} = 150A$

Two examples of the thermal imaging inspection are shown in Figure 6.9.

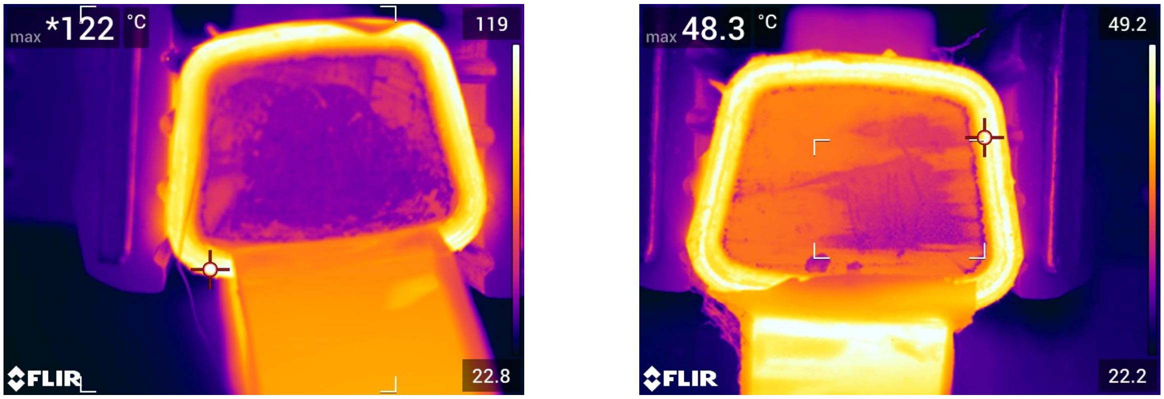

(A) Coil A1 (B) Coil C1

Figure 6.9: Thermal imaging of coils with high current

The surface defects on the pole surfaces (from glue removal and varnish application) create regions of varying emissivity, which is read by the thermal imaging as gradients in temperature. However, none of the areas on the sides of the winding that had low overlap of insulation between turns showed elevated temperatures, indicating that either the insulation system has not failed, or that the thermal imaging could not detect turn-turn shorts.

The mounting method of the coils in the winding energization test does not promote rejection of heat to the surroundings. In fact, a still chamber of air is a notably poor medium for removing heat. Therefore, the temperature rates and magnitudes are expected

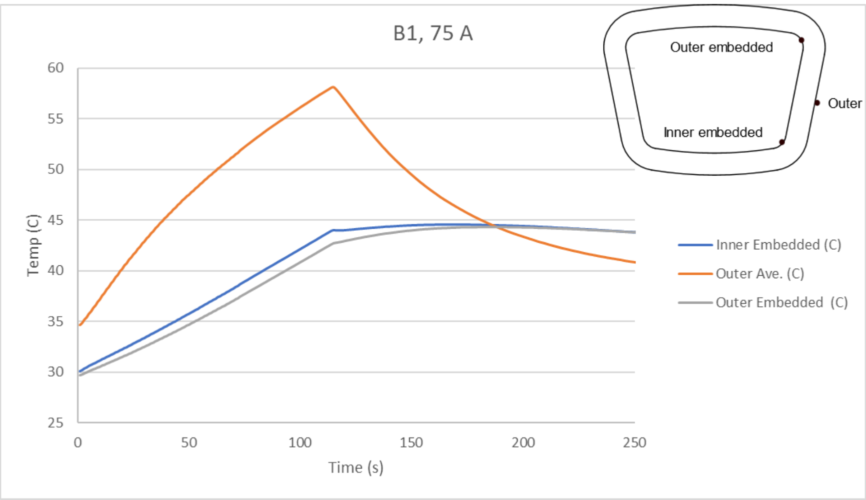

(A) 75 A

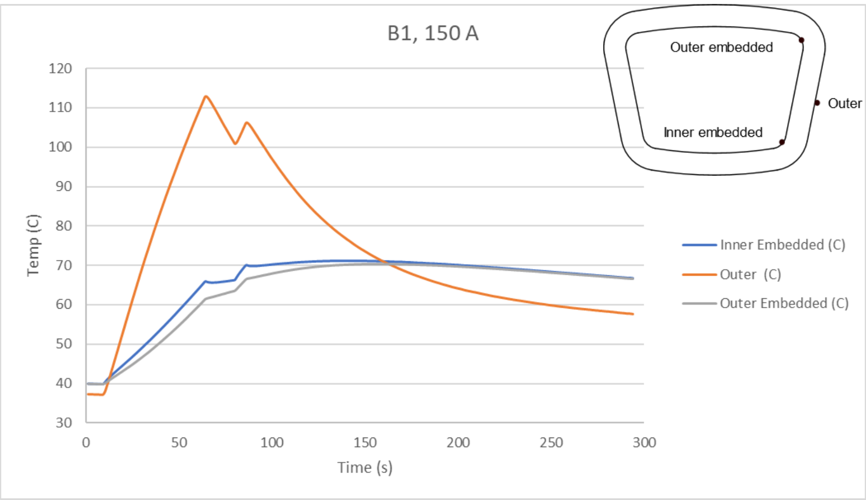

(B) 150 A

FIGURE 6.10: Temperature rise of B1 coil in rubber clamp

to be much less when the windings are installed in the stator. During the energization, the temperature of the inside turns of the coil lagged the outside because of the close contact with SMC, however the exterior of the coil is expected to have better heat rejection when it is installed due to the proximity to the aluminum casing.

6.4 Stator Encapsulation and Airgap Face Machining

The following desired qualities of an epoxy resin for the stator encapsulation can be identified:

- Temperature class 180° C or higher
- Good thermal conductivity
- Close coefficient of thermal expansion to aluminum
- Good adhesion to copper and aluminum
- Low viscosity

RanVar B2-206 from Elantas was identified as a good candidate for the encapsulation material. The epoxy has a thermal class of 180°C and cures at room temperature with the addition of a catalyst. However, its adhesion properties to aluminum and copper are not known and must be confirmed by tests with surfaces similar to the final application. Two adhesion tests were performed, the first with a 1.5" x 1.5" x 0.5" sample in a square aluminum extrusion acting as a mold. The sample was pulled from its mold using an engine hoist and force measured with a load cell. The bond was found to have an ultimate shear strength of 240 kPa. Regardless of the bond strength, additional strength is provided by the "wrap-around" geometry of the stator cavity that the encapsulation fills, limiting the reliance on the shear strength of the bond.

For the second adhesion test, two sample poles with wound coils were encapsulated in a 2" x 2" x 1.5" aluminum frame. A similar pull test was performed to evaluate the strength of the SMC pole to the winding, and the winding to the encapsulation, in series. This test indicates the weak point in the stackup of adhesions which retain the stator pole.

The results of the test show that the weakest point is the bond from coil to pole, which held 1255 N. This exceeds the forces expected on the stator pole by a factor of 7.94.

(A) Two stator poles encapsulated in test mold

(B) Stator pole pulled out after test

FIGURE 6.11: Pull-out test of encapsulated stator coil

To position the stator poles for encapsulation, each stator pole must be fully clamped to the controlled surface of the mold. Before encapsulation, high voltage insulation tests should be performed on the windings to ensure debris has not compromised the insulation. The recesses on the mold plate were taped over with polyimide to avoid false positive insulation failures through the mold plate, as the clamping force could cause some uncovered edge of the foil winding to make contact with the mold plate, and hence the frame. With additional layers of tape between the coil and stator frame, all insulation resistances were measured to be over $40G\Omega$ at 500 V. Before encapsulation, the heights of the pole pieces should be measured to detect the lowest point, used to set the machining height.

Four points on each segment (64 points in total) were measured on a Mitutoyo 544 coordinate measuring machine. Measured points were referenced to a plane defined from the bearing race surface (Figure 6.13b). The lowest pole was measured to be D2R (the inner pole piece of phase D, pole 2). With a range of 0.45mm, this was accepted as the maximum

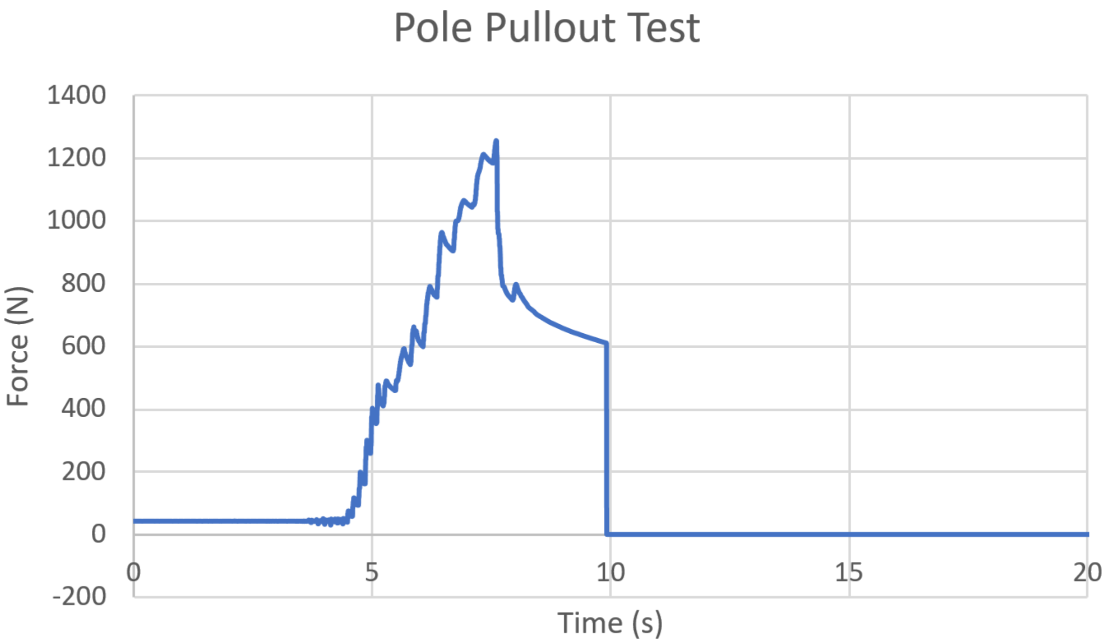

Figure 6.12: Force required to break stator pole free

height of material to be removed by machining. After encapsulation, the stator was mounted in a Birdgeport manual milling machine, and fixtured to level the bearing seat with the XY plane of the machine, within 0.00025". A 3/4" 4-flute end mill was used to machine the high points of the SMC airgap faces. The final surface is shown in Figure 6.14b.

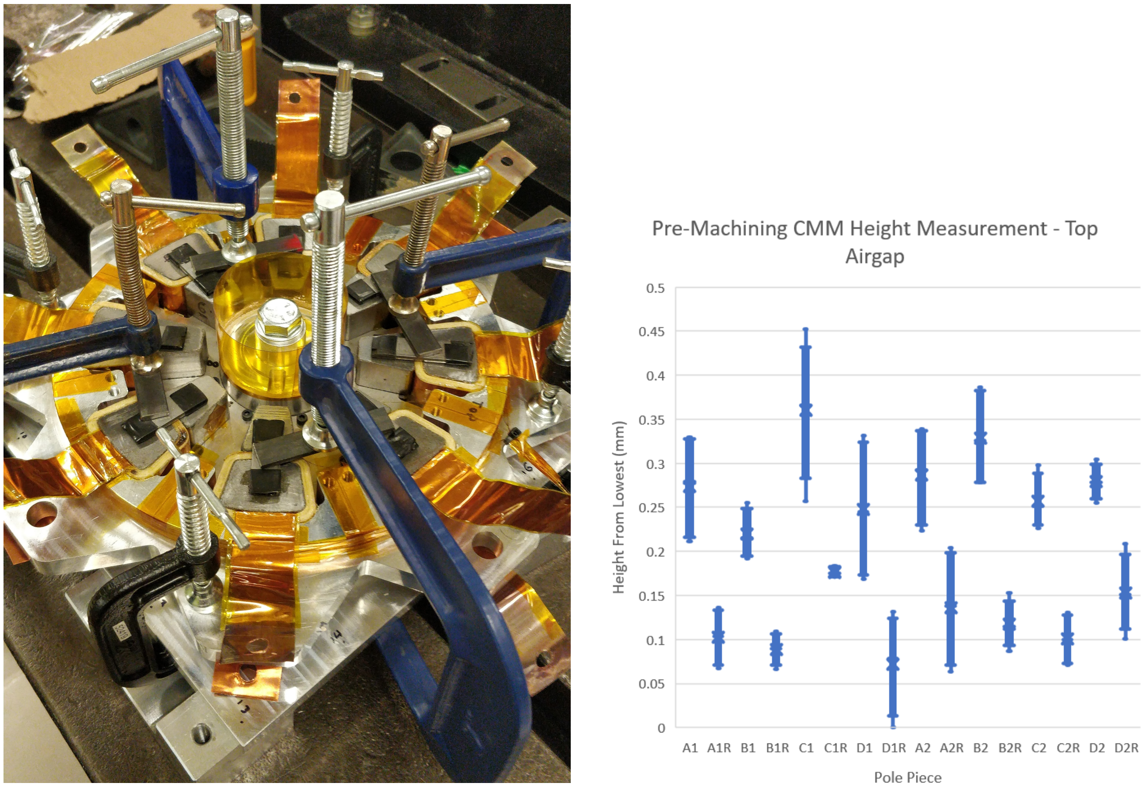

(A) Clamped stator assemble pre-encapsulation

(B) Box plot of stator segment heights from bearing race

Figure 6.13: Pre-encapsulation stator preparation

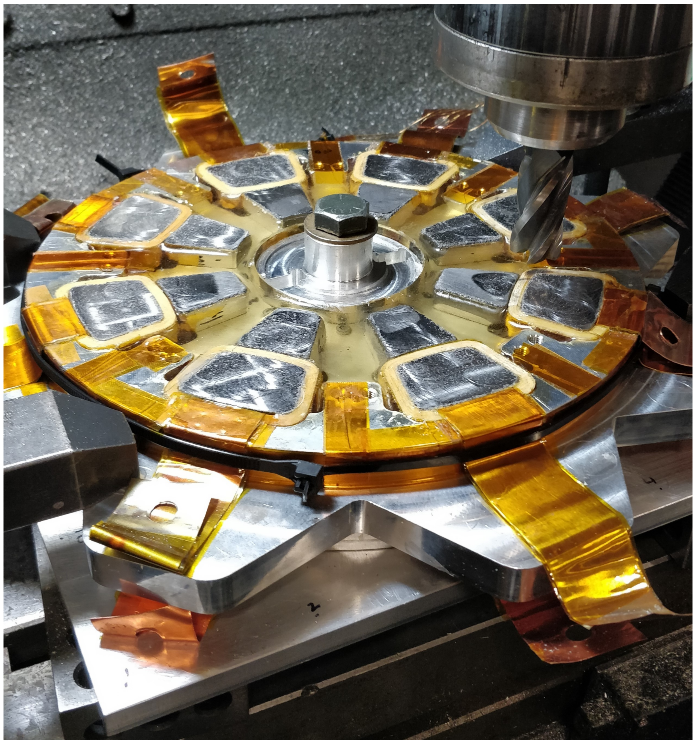

(A) Machining airgap face of encapsulated stator

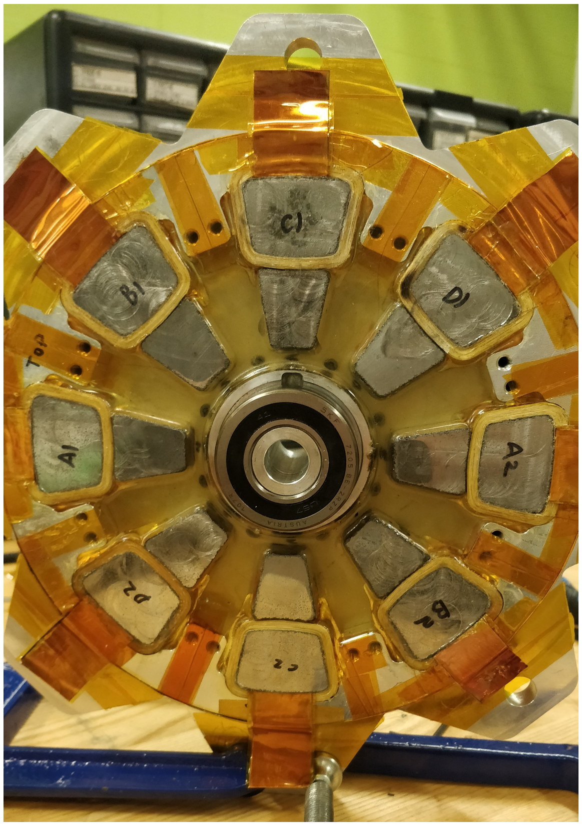

(B) View of machined airgap face

6.5 Rotor Manufacturing

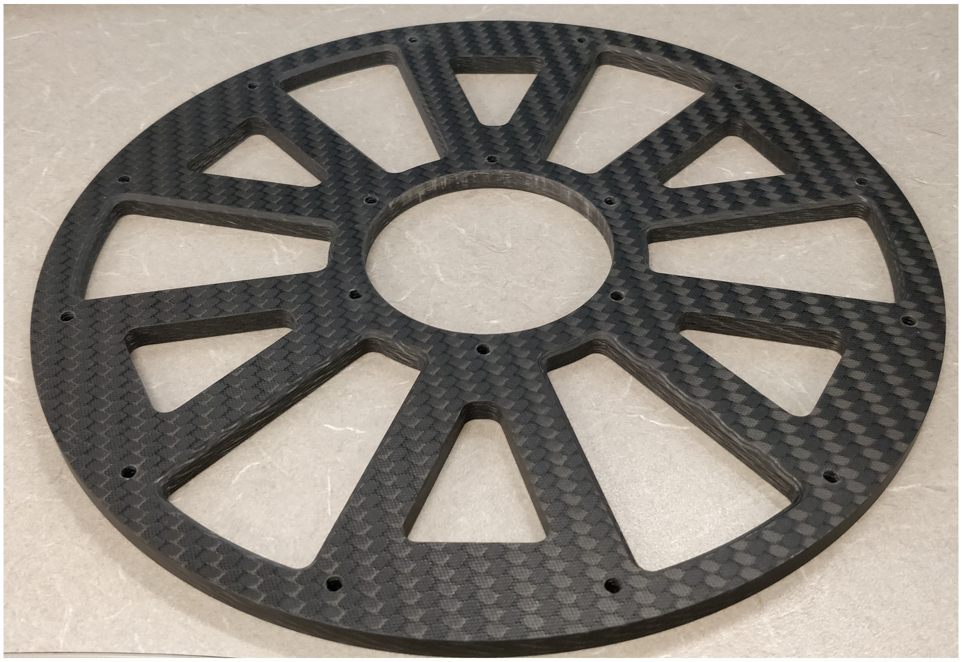

FIGURE 6.15: Machined CFRP retaining ring

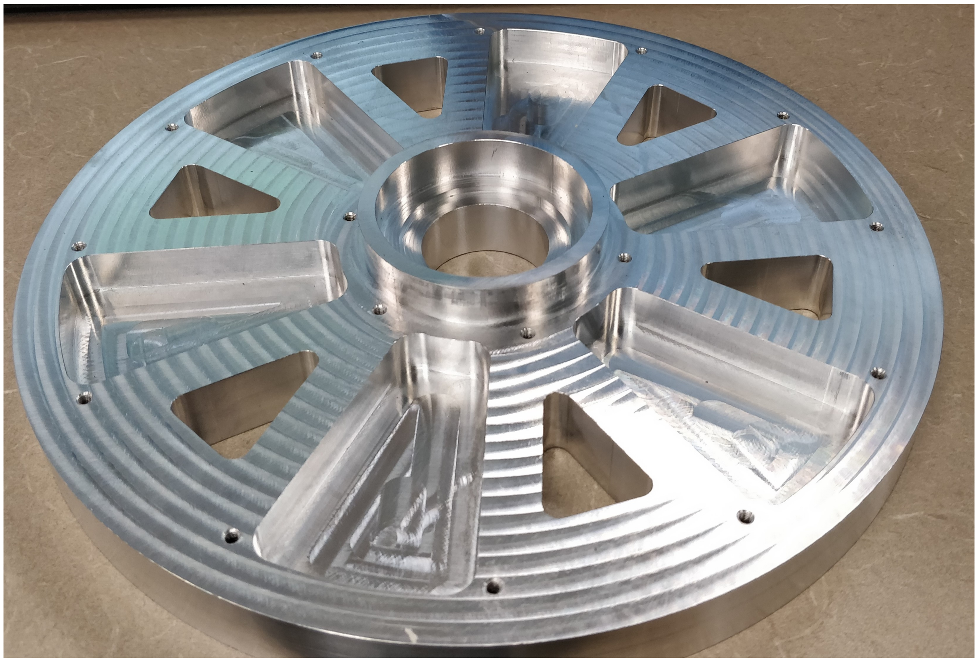

FIGURE 6.16: Machined aluminum rotor yoke

Figure 6.17: Machined SMC rotor pole

Figure 6.18: Full rotor prototype

6.6 Full Assembly

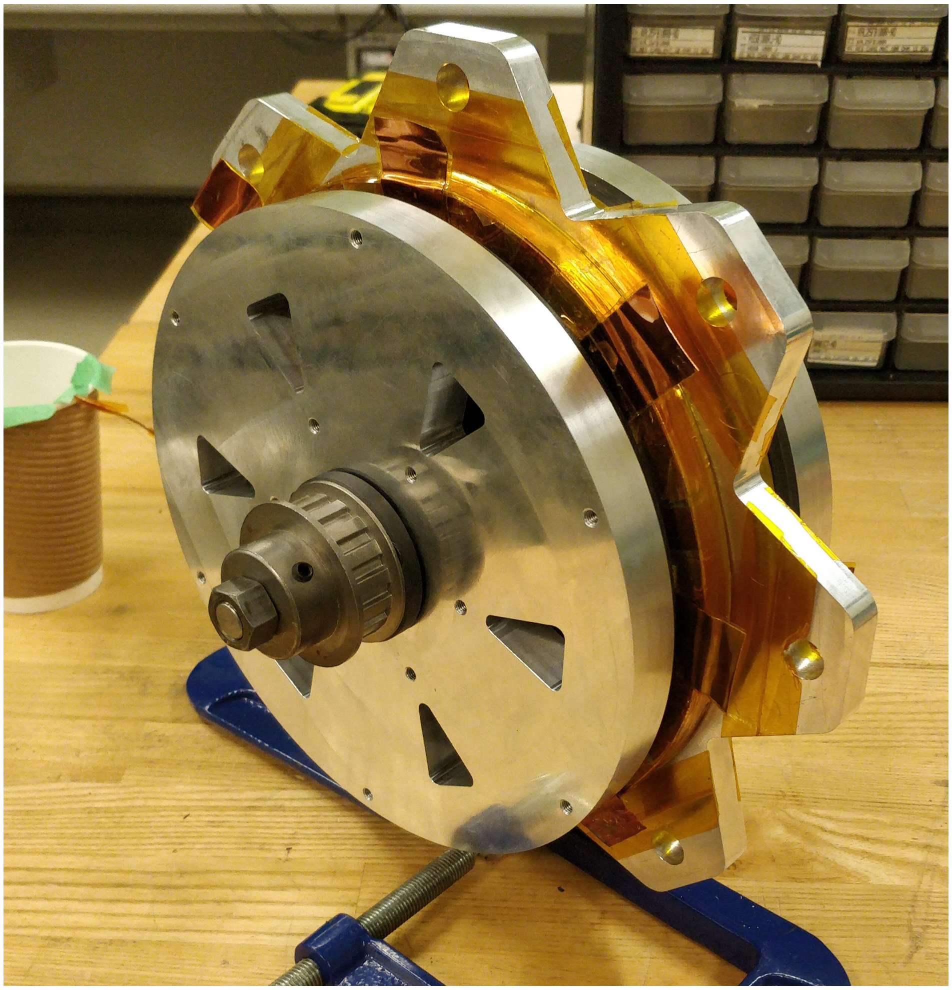

Figure 6.19: Full motor prototype

6.7 Prototyping Challenges

6.7.1 Dimensional Accuracy

Geometric tolerancing presents a significant challenge to prototyping a machine with competitive performance. Due to the plurality of airgaps and the short steel length of the flux path, the machine torque is highly sensitive to airgap length. Maintaining the small airgap requires a high degree of flatness on the stator and rotor faces, as well as a narrow tolerance of parallelity. In fact, the bearing alignment must position the rotor within 0.085° of the stator just to maintain ± 50% of the airgap. This requirement for flatness, as well as the proximity of stator windings to the airgap face, created difficult conditions for the fixturing and facing operations performed on the manual mill. Ultimately, the lowest measured point on the airgap face was not in fact the minimum, and the cutting tool did not remove material in some areas close to the inner radius, visible at the approximate position of the cutting tool in Figure 6.14a.

The large rotor diameter will also create a larger vibration amplitude for a given mass defect in the rotor, therefore a balancing process is critical before testing the assembled machine.

6.7.2 Coil Winding

A near full-width coil prohibits winding tooling from holding the stator pole in place, thus a sub-optimal process of fixturing with glue was necessary. Constant tension of the conductor being wound must be applied manually to avoid gaps between layers, however care must be taken not to break the glue bond to the winding fixture. The low clearance on either side created a small bounds for layup of foil and insulation, and a thickness constraint for the thermocouple that is placed underneath the first winding layer: in order to avoid collision with the rotor poles, the thermocouple wire must be routed within the 1mm clearance between the coil edge and airgap face. The small wire gauge used is susceptible to breakage during handling, or during the airgap face machining operation.

Chapter 7

Conclusion and Future Work

This chapter will provide an overview of the work described in this thesis, and steer future efforts for qualifying the AFSRM for use in a LEV powertrain.

7.1 Summary and Conclusions

A novel electrical machine for propulsion of a light electric vehicle was designed. The performance of the machine was found to be heavily dependent on magnetic properties of the active materials and the fabrication quality of the assembly, in order to achieve a small, uniform airgap. Extensive numerical simulations were performed to demonstrate the variation in performance with phase conduction angles. Simulations show that the machine can compete with similar traction machines in terms of efficiency, however power density can still be improved by investigating additional material removal on the rotor and stator poles.

The thermal properties of a foil winding were exploited to maximize current density without resorting to a liquid-cooled stator. Thermal simulations suggest operation at 200% - 300 % rated torque is possible for durations in the order of 10 minutes.

The rotor structure was found to be a limiting factor, as the SMC material approaches its structural limits as the motor reaches maximum speed.

The motor was prototyped for the purpose of dynamometer testing. Coils wound achieved a 68% fill factor with minimal tooling by using foil conductor. Difficulties in maintaining geometric and dimensional tolerances for the prototype indicate the need for a more variation-tolerant design and simplified assembly procedure.

A testing plan using a dynamometer is proposed to qualify many of the analyses outlined in the previous chapters. Static characteristics may be generated by injecting pulses of voltage to each phase and recording the rise of current. Conclusions about the material properties and manufacturing tolerances can be made from the discrepancy between measured static characteristics and FEA.

Optimization of the active pole geometry to reduce the under-utilized steel mass will further qualify the AFSRM for use in an electric vehicle. Higher-fidelity structural analysis is necessary to capture the transient response of the motor structure to electromagnetic loading. Improvements may be made to the torque quality by defining torque sharing functions that regulate the switch-on and switch-off current profiles.

7.2 Future Work

7.2.1 Proposed Testing Plan

The test bench is constructed on a t-slot table, driving a DC dynamometer through a timing belt with a 1.375:1 reduction. The AFSRM drives a 5 kW DC dynamometer, which can apply torque on the counter-shaft using a programmable DC load. The AFSRM rotor position feedback is provided with an optical encoder, mounted on separate hardware to the t-slot table and connected with a flexible coupling to allow for small shaft misalignments.

The CAD model of the test setup is shown in Figures 7.1, 7.2 below. Not shown are the four-phase converter or associated cabling.

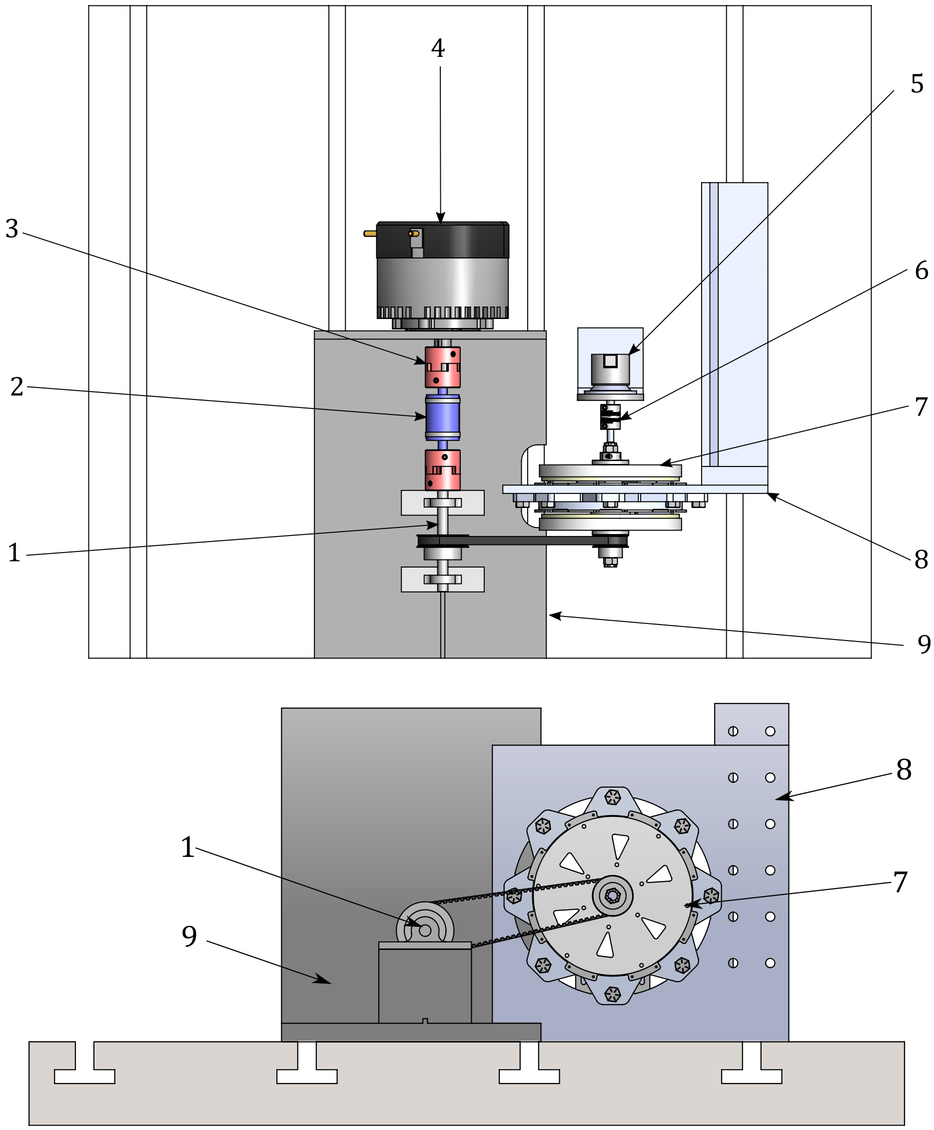

Figure 7.1: Top and front views of the test setup CAD: 1-Counter-shaft. 2-Torque Sensor. 3-Coupling. 4-DC Dynamometer. 5-Optical enocder. 6-Flexible coupling. 7-AFSRM. 8-AFSRM mounting plate. 9-Dynaomometer mounting plate.

A measurement of the static torque and flux linkage characteristics is necessary to baseline the entire testing campaign. Discrepancies in the static characteristics would point to materials or prototyping defects, such as misalignment of the rotor and stator planes or

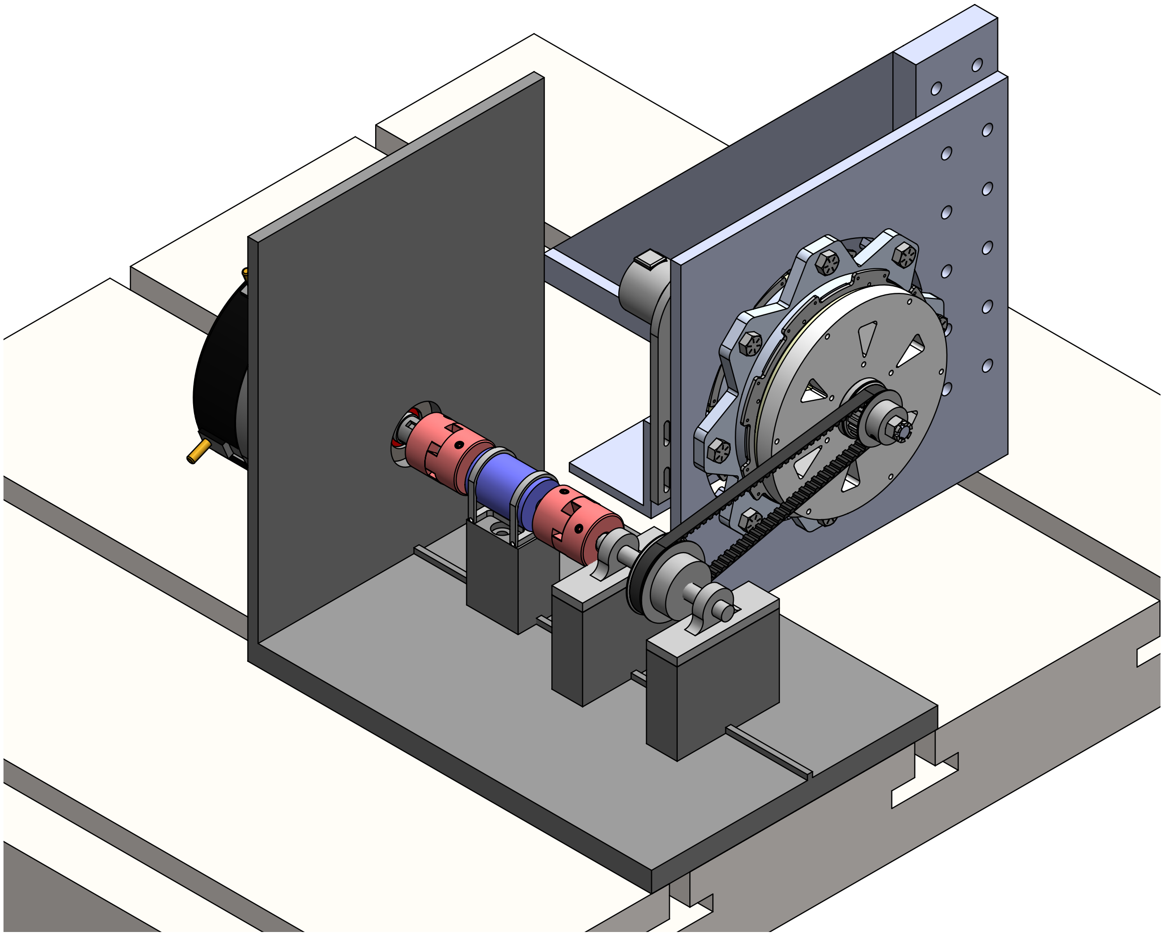

FIGURE 7.2: Isometric view of the test setup CAD

poor edge quality of the SMC. The static characteristics may be measured electrically, using the time rates of change of current. The flux linkage of a SRM phase can be expressed as:

$$\lambda(t) = \int_0^t V - IR\,dt \tag{7.1}$$

In discrete form, the flux can be computed from a measured current at the k$^{\text{th}}$ sample time:

$$\lambda_{\text{k}} = \lambda_{\text{k-1}} + (V - i_{\text{k}}R)(t_{\text{k}} - t_{\text{k-1}}) \tag{7.2}$$

With the AFSRM rotor locked with an rotary indexer, the flux linkage at a rotor position can be calculated by measuring the phase current when it is energized with a known voltage pulse. At this position, a one-dimensional flux linkage lookup table may be recorded, where flux linkage is a function of current. The measurement is repeated for a variety of rotor positions to create a two dimensional lookup table where flux linkage is a function of current and rotor position. Should a torque sensor be available, the torque map may be measured simultaneously. Otherwise, the torque lookup table may be computed by the gradient of inductance in equation 3.9, which can be calculated as:

$$L(i,\theta) = \frac{\partial \lambda(i,\theta)}{\partial i} \tag{7.3}$$

Dynamic tests may be performed by measuring torque and speed with the torque sensor. Efficiency may be measured by recording the electrical power with a four-phase power analyser. While copper losses can be indirectly measured using the current, iron losses are not measurable and must be extracted with the energy balance:

$$P_{\text{Iron}} = P_{\text{shaft}} - P_{\text{copper}} - P_{\text{mech}} \tag{7.4}$$

where $\mathrm{P}_{\text{shaft}}$ is the output power measured by the torque sensor, $\mathrm{P}_{\text{copper}}$ is the resistive copper loss and P_{mech} is the mechanical losses that includes windage and bearing friction. Since mechanical losses are dependent on speed, a spin-down test may be performed on the motor to map the windage and bearing losses. This is performed by spinning the rotor to its maximum speed, then removing the current excitation and recording the angular deceleration as a function of speed. The spin-down test requires an accurate estimation of rotor inertia, which can be provided by the CAD model.

The high speed operation of the motor requires consideration of burst containment, should a failure occur in the rotor structure. Due to the open-rotor construction, a rotor failure would not be contained, which creates a hazard for occupants of the test room. The hazard may be managed with a containment chamber that may be lowered over the test setup. The containment chamber should enclose all rotating components, while providing sufficient airflow. The sizing of a containment chamber wall thickness may be guided by an energy balance between the kinetic energy of the rotor and the shear and strain energy of the containment chamber wall at the impact zone [23]. A rotor failure of the AFSRM is likely to eject single rotor poles in unique trajectories, simplifying the containment chamber design to withstand impact of a single rotor pole, before factors of safety. The energy that must be suppressed by the containment chamber is assumed equal to the kinetic energy of the rotor pole, which can be expressed as:

$$E_{\text{pole}} = \frac{1}{2} J \omega^2 \tag{7.5}$$

which is 4.443 kJ for a single rotor pole at 8000 RPM. The tensile and compressive energy for the impact zone on the containment chamber wall are defined as [65]:

$$E_{\text{wall}} = A_{\text{impact}} t_{\text{wall}} \epsilon_{\max} \sigma_{\max} + C_{\text{shear}} \tau_{\max} P_{\text{impact}} {t_{\text{wall}}}^2 \tag{7.6}$$

where $\epsilon_{\max}, \sigma_{\max}$ and $\tau_{\max}$ are the strain, stress and shear stress limits for the material, A_{impact} and P_{impact} are the area and perimeter of the impact zone, C_{shear} is an experimental shear coefficient (conservatively assumed as 0.3) and t_{wall} is the thickness of the containment chamber wall. Assuming the outer face of the rotor pole collides with the containment chamber wall in the normal direction, and material properties for A36 steel, the required thickness is calculated to be 17.33 mm, or 11/16". It should be noted that this sizing exercise does not account for kinetic energy transfer from the projectile to the containment chamber, which will drive down the wall thickness requirement.

7.2.2 Further Design Improvements

Besides the proposed bench testing plan for the AFSRM, a number of further design improvement areas are suggested.

- **Mass Reduction:** While the AFSRM design meets the minimum criteria to validate the topology, further effort is necessary to reduce the mass of both the active and structural components. The torque curves in Figure 5.1 indicate that global saturation of the rotor poles is not achieved, and while FEA indicates high levels of saturation near the airgap surface, the utilization of the SMC away from the airgap could be improved. This could be achieved by increasing the number of turns, lowering the operating speed of the motor, which may in fact lend itself well to the structural limitations of the rotor at high speed. Alternatively, regions of SMC that suffer low utilization could be removed, increasing the saturation of the material and reducing the weight with the same stator MMF.

- **Current Shaping:** Further effort in the control optimization of the AFSRM is necessary to allow for acceptable torque quality across a wide speed range. Currently, the optimization of the switching angles allows for good torque quality at light loads, however the torque quality suffers when the machine is operating at max current. Shaping of the current, particularly at the point where the conduction of consecutive phases overlaps, will be key in producing better torque quality. Current shaping is only possible at low speeds, where the DC link voltage is significantly higher than the induced voltage. The profiles at the leading and trailing edge of the current waveform may be shaped by torque-sharing functions, which have been applied extensively to RFSRM control.

- **Transient Structural Analysis:** Although a baseline for vibrational response has been established, the effect of nonsinusoidal axial loading has not been studied. The transient magnetic forces on the rotor must be inserted into a transient structural model, which may compute the reaction of the rotor structure in the time domain. Higher fidelity models for material damping must be implemented, as the benefits of the CFRP as a damping element are not fully quantified. Finally, the vibrational behaviour of the stator must be studied, and the combined rotor and stator vibrations must be considered to confirm that the machine airgap is maintained even under transient conditions.

References

[1] J. Lin et al. “A novel axial flux switched reluctance motor with multi-level air gap geometry”. In: *2016 IEEE Electrical Power and Energy Conference (EPEC)*. 2016, pp. 1–8.

[2] C. Kennedy, I.D. Stewart, and M. Westphal. *Shifting Currents: Opportunities for Low-Carbon Electric Cities in the Global South*. Tech. rep. World Resources Institute, 2019.

[3] M. Humphries. *Rare Earth Elements: The Global Supply Chain*. Tech. rep. US Congressional Research Service, 2013.

[4] B. Bilgin. *Switched Reluctance Motor Drives*. CRC Press, 2018. ISBN: 113830459X.

[5] M. Rios. “Thermal Analysis of Foil Wound Conductors used in Axial Flux Permanent Magnet Alternators”. 2015.

[6] M. Rios. “Foil Windings in Electrical Machines”. 2018.

[7] M. Ehsani et al. *Modern Electric, Hybrid Electric and Fuel Cell Vehicles*. CRC Press, 2010. ISBN: 0-8493-3154-4.

[8] Blaz Segavac. *Agni Lynch motor fitted to an electric motorcycle*. 2011. URL: https://en.wikipedia.org/wiki/Lynch_motor#/media/File:Voltron-electric-motorcycle-agni-lynch-motor.jpg.

[9] A. Dieng, M. F. Benkhoris, and M. Ait-Ahmed. "Torque ripples reduction of five-phase PMSM using fractional order regulator". In: *2012 XXth International Conference on Electrical Machines*. Sept. 2012, pp. 1114–1120.

[10] B. Howey, B. Bilgin, and A. Emadi. "Design of a mutually coupled external-rotor direct drive E-bike switched reluctance motor". In: *IET Electrical Systems in Transportation* 10.1 (2020), pp. 89–95. ISSN: 2042-9746. DOI: 10.1049/iet-est.2018.5076.

[11] J. Lin, N. Schofield, and A. Emadi. "External-Rotor $6-10$ Switched Reluctance Motor for an Electric Bicycle". In: *IEEE Transactions on Transportation Electrification* 1.4 (Dec. 2015), pp. 348–356. ISSN: 2372-2088. DOI: 10.1109/TTE.2015.2502543.

[12] D. G. Dorrell et al. "Comparison of different motor design drives for hybrid electric vehicles". In: *2010 IEEE Energy Conversion Congress and Exposition*. Sept. 2010, pp. 3352–3359. DOI: 10.1109/ECCE.2010.5618318.

[13] Trading Economics. *HG1 Historical Price Data*. 2020. URL: https://tradingeconomics.com/commodity/copper.

[14] Trading Economics. *SREMNDM Historical Price Data*. 2020. URL: https://tradingeconomics.com/commodity/neodymium.

[15] Trading Economics. *SCO Historical Price Data*. 2020. URL: https://tradingeconomics.com/commodity/iron-ore.

[16] H. Li, B. Bilgin, and A. Emadi. "An Improved Torque Sharing Function for Torque Ripple Reduction in Switched Reluctance Machines". In: *IEEE Transactions on Power Electronics* 34.2 (Feb. 2019), pp. 1635–1644. ISSN: 1941-0107. DOI: 10.1109/TPEL.2018.2835773.

[17] Berker Bilgin and Ali Emadi. "Electric Motors in Electrified Transportation: A step toward achieving a sustainable and highly efficient transportation system". In: *IEEE Power Electronics Magazine* 1 (2014), pp. 10–17.

[18] T. Burress and S. Campbell. “Benchmarking EV and HEV power electronics and electric machines”. In: *2013 IEEE Transportation Electrification Conference and Expo (ITEC)*. 2013, pp. 1–6.

[19] T. Burress, S. Rogers, and B. Ozpineci. *Benchmarking Electric Vehicles and Hybrid Electric Vehicles*. Tech. rep. Oak Ridge National Laboratory, 2016.

[20] R. P. Wojda and M. K. Kazimierczuk. “Winding resistance of litz-wire and multi-strand inductors”. In: *IET Power Electronics* 5.2 (2012), pp. 257–268.

[21] M.K. Kazimierczuk. *High Frequency Magnetic Components*. John Wiley and Sons, 2014. ISBN: 9781118717714.

[22] Rafal Wojda. “Winding Resistance and Winding Power Loss of High-Frequency Power Inductors”. 2012.

[23] W. Tong. *Mechanical Design of Electric motors*. CRC Press, 2014. ISBN: 978-1-4200-9144-1.

[24] C. P. Steinmetz. “On the law of hysteresis”. In: *Proceedings of the IEEE* 72.2 (1984), pp. 197–221.

[25] A. Boglietti et al. “Predicting iron losses in soft magnetic materials with arbitrary voltage supply: an engineering approach”. In: *IEEE Transactions on Magnetics* 39.2 (2003), pp. 981–989.

[26] G. Bertotti. “Physical interpretation of eddy current losses in ferromagnetic materials. I. Theoretical considerations”. In: *Journal of Applied Physics* 57.6 (1985), pp. 2110–2117. DOI: `10.1063/1.334404`. eprint: `https://doi.org/10.1063/1.334404`. URL: `https://doi.org/10.1063/1.334404`.

[27] R. Siebert, J. Schneider, and E. Beyer. “Laser Cutting and Mechanical Cutting of Electrical Steels and its Effect on the Magnetic Properties”. In: *IEEE Transactions on Magnetics* 50.4 (2014), pp. 1–4.

[28] SKF Inc. *The SKF model for calculating the frictional moment*. URL: `https://www.skf.com/binary/21-299767/0901d1968065e9e7-The-SKF-model-for-calculating-the-frictional-movement_tcm_12-299767.pdf`.

[29] K. Kiyota et al. "Cylindrical Rotor Design for Acoustic Noise and Windage Loss Reduction in Switched Reluctance Motor for HEV Applications". In: *IEEE Transactions on Industry Applications* 52.1 (2016), pp. 154–162.

[30] J Saari. "Thermal Analysis of High-Speed Induction Machines". 1998.

[31] A. C. Malloy, R. F. Martinez-Botas, and M. Lampérth. "Measurement of Magnet Losses in a Surface Mounted Permanent Magnet Synchronous Machine". In: *IEEE Transactions on Energy Conversion* 30.1 (Mar. 2015), pp. 323–330. ISSN: 1558-0059. DOI: 10.1109/TEC.2014.2353133.

[32] P. Anpalahan and M. Lamperth. "Design of multi-stack axial flux permanent magnet generator for a hybrid electric vehicle". In: *2006 IEEE Vehicle Power and Propulsion Conference*. Sept. 2006, pp. 1–4. DOI: 10.1109/VPPC.2006.364273.

[33] A. C. Malloy et al. "Axial flux machines for hybrid module applications". In: *2014 IEEE International Electric Vehicle Conference (IEVC)*. Dec. 2014, pp. 1–8. DOI: 10.1109/IEVC.2014.7056159.

[34] Ben Katz. *Emrax Motor Teardown*. 2017. URL: https://www.evans-electric.com.au/.

[35] BorgWarner Inc. *Remy HVH250 Datasheet*. 2019. URL: https://cdn.borgwarner.com/docs/default-source/default-document-library/remy-pds---hvh250-115-sheet-euro-pr-3-16.pdf?sfvrsn=ad42cd3c_11.

[36] Avid Technology Inc. *EVO Motors Product Page*. 2019. URL: https://avidtp.com/product/evo-motors/.

[37] YASA Inc. *YASA 750R Product Page*. 2019. URL: https://avidtp.com/product/evo-motors/.

[38] Emrax Inc. *Emrax 268 Technical Data Summary*. 2019. URL: https://emrax.com/products/emrax-268/.

[39] Shang-Hsun Mao and Mi-Ching Tsai. “A novel switched reluctance motor with C-core stators”. In: *IEEE Transactions on Magnetics* 41.12 (Dec. 2005), pp. 4413–4420. ISSN: 1941-0069. DOI: 10.1109/TMAG.2005.858372.

[40] A. Labak and N. C. Kar. “A novel five-phase pancake shaped switched reluctance motor for hybrid electric vehicles”. In: *2009 IEEE Vehicle Power and Propulsion Conference*. Sept. 2009, pp. 494–499. DOI: 10.1109/VPPC.2009.5289806.

[41] J. H. J. Potgieter et al. “Performance evaluation of a high speed segmented rotor axial flux switched reluctance traction motor”. In: *2016 XXII International Conference on Electrical Machines (ICEM)*. Sept. 2016, pp. 531–537. DOI: 10.1109/ICELMACH.2016.7732577.

[42] P. Andrada et al. “New axial-flux switched reluctance motor for e-scooter”. In: *2016 International Conference on Electrical Systems for Aircraft, Railway, Ship Propulsion and Road Vehicles International Transportation Electrification Conference (ESARS-ITEC)*. Nov. 2016, pp. 1–6. DOI: 10.1109/ESARS-ITEC.2016.7841417.

[43] J. Ma, R. Qu, and J. Li. “Optimal design of axial flux switched reluctance motor for electric vehicle application”. In: *2014 17th International Conference on Electrical Machines and Systems (ICEMS)*. Oct. 2014, pp. 1860–1865. DOI: 10.1109/ICEMS.2014.7013786.

[44] J. Ma, R. Qu, and J. Li. “Optimal design of an axial flux switched reluctance motor with grain oriented electrical steel”. In: *2015 18th International Conference on Electrical Machines and Systems (ICEMS)*. Oct. 2015, pp. 2071–2077. DOI: 10.1109/ICEMS.2015.7385381.

[45] J. M. Kokernak and D. A. Torrey. “Magnetic circuit model for the mutually coupled switched-reluctance machine”. In: *IEEE Transactions on Magnetics* 36.2 (Mar. 2000), pp. 500–507. ISSN: 1941-0069. DOI: 10.1109/20.825824.

[46] A. Labak and N. C. Kar. "Designing and Prototyping a Novel Five-Phase Pancake-Shaped Axial-Flux SRM for Electric Vehicle Application Through Dynamic FEA Incorporating Flux-Tube Modeling". In: *IEEE Transactions on Industry Applications* 49.3 (May 2013), pp. 1276–1288. ISSN: 1939-9367. DOI: 10.1109/TIA.2013.2252871.

[47] T. Lambert, M. Biglarbegian, and S Mahmud. "A Novel Approach to the Design of Axial-Flux Switched Reluctance Motors". In: *Machines* (2015).

[48] S. Murakami, H. Goto, and O. Ichinokura. "A study about optimum stator pole design of Axial-gap switched reluctance motor". In: *2014 International Conference on Electrical Machines (ICEM)*. Sept. 2014, pp. 975–980. DOI: 10.1109/ICELMACH.2014.6960299.

[49] K. Deguchi, S. Sumita, and Y. Enomoto. "A 3.7-kW axial-gap switched-reluctance motor robustly designed by using a mathematical model". In: *2014 International Conference on Electrical Machines (ICEM)*. Sept. 2014, pp. 340–345. DOI: 10.1109/ICELMACH.2014.6960203.

[50] A. Labak and N. C. Kar. "Novel Approaches Towards Leakage Flux Reduction in Axial Flux Switched Reluctance Machines". In: *IEEE Transactions on Magnetics* 49.8 (Aug. 2013), pp. 4738–4741. ISSN: 1941-0069. DOI: 10.1109/TMAG.2013.2261287.

[51] M. J. Kermanipour and B. Ganji. "Modification in Geometric Structure of Double-Sided Axial Flux Switched Reluctance Motor for Mitigating Torque Ripple". In: *Canadian Journal of Electrical and Computer Engineering* 38.4 (2015), pp. 318–322.

[52] A. Schoppa and P. Delarbre. "Soft Magnetic Powder Composites and Potential Applications in Modern Electric Machines and Devices". In: *IEEE Transactions on Magnetics* 50.4 (Apr. 2014), pp. 1–4. ISSN: 1941-0069. DOI: 10.1109/TMAG.2013.2290135.

[53] H. Vansompel, P. Leijnen, and P. Sergeant. "Multiphysics Analysis of a Stator Construction Method in Yokeless and Segmented Armature Axial Flux PM Machines". In: *IEEE Transactions on Energy Conversion* 34.1 (Mar. 2019), pp. 139–146. ISSN: 1558-0059. DOI: 10.1109/TEC.2018.2862622.

[54] A. Binder, T. Schneider, and M. Klohr. “Fixation of buried and surface-mounted magnets in high-speed permanent-magnet synchronous machines”. In: *IEEE Transactions on Industry Applications* 42.4 (July 2006), pp. 1031–1037. ISSN: 1939-9367. DOI: 10.1109/TIA.2006.876072.

[55] R. Madhavan and B. G. Fernandes. “Performance Improvement in the Axial Flux-Segmented Rotor-Switched Reluctance Motor”. In: *IEEE Transactions on Energy Conversion* 29.3 (Sept. 2014), pp. 641–651. ISSN: 1558-0059. DOI: 10.1109/TEC.2014.2314657.

[56] H. Goto. “Double Stator Axial-Flux Switched Reluctance Motor for Electric City Commuters”. In: *2018 International Power Electronics Conference (IPEC-Niigata 2018 -ECCE Asia)*. May 2018, pp. 3192–3196. DOI: 10.23919/IPEC.2018.8507599.

[57] H. Torkaman, A. Ghaheri, and A. Keyhani. “Axial flux switched reluctance machines: a comprehensive review of design and topologies”. In: *IET Electric Power Applications* 13.3 (2019), pp. 310–321. ISSN: 1751-8679. DOI: 10.1049/iet-epa.2018.5190.

[58] Bo Zhang. “Soft Magnetic Composites in Novel Designs of Electrical Traction Machines”. 2016.

[59] M.Przybylski, D Kapelski, and B Slusarek. “Mechanical Properties of Soft Magnetic Composites at the Temperature of Liquid Nitrogen”. In: *12th Symposium of Magnetic Measurements and Modeling*. Vol. 131. 5. 2017, pp. 1199–1203.

[60] W. Palm. *Mechanical Vibration*. Wiley Press, 2006. ISBN: 978-0-471-34555-8.

[61] B. Wu, C. Jin, and Y Hu. “Theoretical Calculation of Thermal Contact Resistance of Ball Bearing Under Different Loads”. In: *6th International Conference on Informatics in Control, Automation and Robotics.*

[62] D. A. Howey, P. R. N. Childs, and A. S. Holmes. “Air-Gap Convection in Rotating Electrical Machines”. In: *IEEE Transactions on Industrial Electronics* 59.3 (2012), pp. 1367–1375.

[63] D. A. Howey, A. S. Holmes, and K. R. Pullen. "Measurement and CFD Prediction of Heat Transfer in Air-Cooled Disc-Type Electrical Machines". In: *IEEE Transactions on Industry Applications* 47.4 (2011), pp. 1716–1723.

[64] North American Hoganas. *Somaloy Prorotyping Material Brochure*. 2017. URL: `https://www.hoganas.com/globalassets/download-media/sharepoint/brochures-and-datasheets---all-documents/somaloy-prototyping-material_march_2016_1334hog.pdf`.

[65] A.C. Hagg and G.O. Sankey. "The Containment of Disk Burst Fragments by Cylindrical Shells". In: *ASME Journal of Engineering for Gas Turbines and Power* 96.2 (1974), pp. 114–123.